AFAPL-TR-78-2

LEVEL

2

NUMERICAL CALCULATIONS OF THE VISCOUS FLOW IN A SUPERSONIC COMPRESSOR CASCADE WITH SPLITTER VANES

L. WALITT
C. Y. LIU

NUMERICAL CONTINUUM MECHANICS, INC.
6269 VARIEL AVENUE, SUITE 200
WOODLAND HILLS, CALIFORNIA 91367

DDC

NOV 16 1978

F

FEBRUARY 1978

Approved for public release; distribution unlimited.

78 10 27 063

NOTICE

When Government drawings, specifications, or other data are used for any purpose other than in connection with a definitely related Government procurement operation, the United States Government thereby incurs no responsibility nor any obligation whatsoever; and the fact that the government may have formulated, furnished, or in any way supplied the said drawings, specifications, or other data, is not to be regarded by implication or otherwise as in any manner licensing the holder or any other person or corporation, or conveying any rights or permission to manufacture, use, or sell any patented invention that may in any way be related thereto.

This report has been reviewed by the Information Office (OI) and is releasable to the National Technical Information Service (NTIS). At NTIS, it will be available to the general public, including foreign nations.

This technical report has been reviewed and is approved for publication.
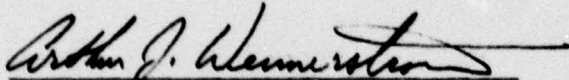
ARTHUR J. WENNERSTROM
Project Engineer

WALKER H. MITCHELL
Acting Chief, Technology Branch

FOR THE COMMANDER
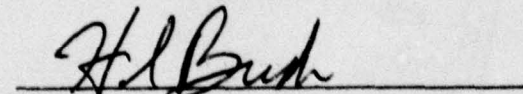
H. I. BUSH
Deputy Director
Turbine Engine Division

"If your address has changed, if you wish to be removed from our mailing list, or if the addressee is no longer employed by your organization please notify A. J. Wennerstrom (AFAPL/TBX), W-PAFB, OH 45433 to help us maintain a current mailing list."

Copies of this report should not be returned unless return is required by security considerations, contractual obligations, or notice on a specific document.

REPORT DOCUMENTATION PAGE	READ INSTRUCTIONS BEFORE COMPLETING FORM

1. REPORT NUMBER	2. GOVT ACCESSION NO.	3. RECIPIENT'S CATALOG NUMBER
AFAPL-TR-78-2		

4. TITLE (and Subtitle)	5. TYPE OF REPORT & PERIOD COVERED
Numerical Calculations of the Viscous Flow in a Supersonic Compressor Cascade with Splitter Vanes.	Final Report. Nov 1975 - Oct 1977
	6. PERFORMING ORG. REPORT NUMBER
	NCMR-77-101

7. AUTHOR(s)	8. CONTRACT OR GRANT NUMBER(s)
Leonard Walitt C.Y. Liu	F33615-76-C-2011

9. PERFORMING ORGANIZATION NAME AND ADDRESS	10. PROGRAM ELEMENT, PROJECT, TASK AREA & WORK UNIT NUMBERS
Numerical Continuum Mechanics, Inc. 6269 Variel Avenue, Suite 200 Woodland Hills, California 91367	Project 2307 Task S1 Work Unit 29

11. CONTROLLING OFFICE NAME AND ADDRESS	12. REPORT DATE
Air Force Aero Propulsion Laboratory Air Force Systems Command United States Air Force, Wright-Patterson AFB, Ohio 45433	February 1978
	13. NUMBER OF PAGES
	143 p.

14. MONITORING AGENCY NAME & ADDRESS(if different from Controlling Office)	15. SECURITY CLASS. (of this report)
Commander DCASD Van Nuys 6230 Van Nuys Blvd. Van Nuys, California 91408	Unclassified
	15a. DECLASSIFICATION/DOWNGRADING SCHEDULE

16. DISTRIBUTION STATEMENT (of this Report)

Approved for Public Release; Distribution Unlimited

61102F

17. DISTRIBUTION STATEMENT (of the abstract entered in Block 20, if different from Report)

18. SUPPLEMENTARY NOTES

19. KEY WORDS (Continue on reverse side if necessary and identify by block number)

Viscous flow, Compressor aerodynamics, Navier-Stokes solution, Numerical fluid mechanics, Compressor cascade, Three-dimensional flow

20. ABSTRACT (Continue on reverse side if necessary and identify by block number)

A numerical method has been developed to solve the steady, three-dimensional Reynolds-averaged Navier-Stokes equations by iteration. The computer code which embodies the method was employed to calculate the viscous flow field about an axial compressor cascade at a freestream Mach number of 1.46 and a freestream Reynolds number based on chord of 1.36 million. The cascade geometry contained splitter vanes and contoured sidewalls to simulate the flow in the streamtube of an axial compressor rotor. A strong shock wave

DD FORM 1473 EDITION OF 1 NOV 65 IS OBSOLETE

boundary layer interaction, with strong separation, was computed on the suction surface of the main cascade blade. This interaction region distorted the cascade flow field and resulted in high system losses. Measurements of static pressure on the main cascade blade and splitter vane compared favorably with corresponding computed static pressures. In addition measurements of the mass averaged static pressure and Mach number in the wake of the cascade agreed with corresponding computed mass averaged quantities.

PREFACE

ACCESSION for

NTIS   White Section
DDC   Buff Section
UNANNOUNCED
JUSTIFICATION

BY
DISTRIBUTION/AVAILABILITY CODES

A

iii

TABLE OF CONTENTS

LIST OF ILLUSTRATIONS

LIST OF SYMBOLS

This section presents a partial list of the notation employed. Symbols missing from this list are defined in the text.

$\underline{A}$	Vector surface area
A	Area in (x,y) plane
dA	Area element in (x,y) plane
c	Local sound speed
c_p	Specific heat at constant pressure
c_v	Specific heat at constant volume
C	Closed curve in (x,y) plane
dC	Arc length element along curve C
e	Turbulent kinetic energy
E	Specific internal energy, ft-lbs/slug
f	Function which related curvilinear coordinate x to generalized coordinates, $x=f(\xi, \eta, \tau)$
g	Function which relates curvilinear coordinate y to generalized coordinates, $x=g(\xi, \eta, \tau)$
h	Enthalpy
H_t	Stagnation enthalpy
h_x	Metric in the x-direction
h_y	Metric in the y-direction
h_z	Metric in the z-direction
$\underline{i}$	Unit vector in x-direction
$\underline{j}$	Unit vector in y-direction
J	J-line, streamline-like-line or Jacobian of transformation
$\underline{k}$	Unit vector in z-direction
K	K-line, potential-like-line
ℓ	$\int h_x dx$

x

m	Mass or $\int h_y \, dy$
M	Mach number
$\underline{M}$	Momentum vector
n	$\int h_z \, dz$
$\underline{n}$	Unit vector normal to curve C in (x,y) plane
N	Cycle count
p	Pressure, lbs/ft.^{2}
P_+	Stagnation pressure, lbs/ft.^{2}
$\underline{q}$	Transformed particle velocity vector in (x,y) plane
$\underline{q_s}$	Transformed mesh point velocity vector in (x,y) plane
r_o	Radius at discharge, ft
r	Radius, ft.
R	Gas constant, ft/$^\circ$R
Re	Reynolds number
Re_x	Reynolds number based on distance along body
Re_θ	Reynolds number based on momentum thickness
S_x	Mesh point coordinate velocity in the x-direction, fps
S_y	Mesh point coordinate velocity in the y-direction, fps
t	Time, secs or time-like-coordinate, secs/ft
Δt_c	Timestep controlled by sound speed
Δt_d	Timestep controlled by diffusive effects
T	Temperature, $^\circ$R
u	Component of velocity in the x-direction, fps
u_e	Velocity at boundary layer outer edge, fps
U_z	Velocity of blade-to-blade and/or cross-sectional sur-fact, fps
v	Component of velocity in the y-direction, fps

w	Component of velocity in the z-direction, fps
w^1	Perturbation velocity in the z-direction, fps
$\underline{W}$	Average velocity vector in (x,y) plane, fps
W	Velocity ($\sqrt{u^2 + v^2 + w^2}$), fps
x	Curvilinear coordinate associated with the angular direction
x	Distance along a surface
x_1, x_2, x_3	Cartesian coordinates
y	Curvilinear coordinate which labels potential-like-lines in the meridional plane
y	Distance normal to surface
z	Curvilinear coordinate which labels streamlike-lines in the meridional plane
γ	Ratio of specific heats,
ϵ	Eddy viscosity
μ	Molecular viscosity, slugs/ft-sec
ρ	Density, slugs/ft^3
τ	Characteristic time for calculation or time in generalized coordinates
τ_{ij}	Turbulent shear stress tensor
η	Generalized distance coordinate
ξ	Generalized distance coordinate
Ω	Turbulent vorticity
σ_{ij}	Total stress tensor
θ	Angular coordinate, or momentum thickness
δ	Boundary layer thickness
δ^*	Displacement thickness
δ_i^*	Incompressible displacement thickness
ω	Angular velocity, radians/sec

Superscripts

$( )^n$ Property associated with time t^n

$( )^{n-\frac{1}{2}}$ Property associated with time $t^{n-\frac{1}{2}}$

Subscripts

$\tilde{( )}$ Property evaluated from a previous iterate

$( )_r$ Reference condition

$( )_t$ Stagnation condition

$( )_o$ Laboratory stagnation condition

$( )_i$ Ideal or inviscid condition

SECTION I

INTRODUCTION

The principal objective of this study was to numerically calculate the three dimensional, viscous flow field in a cascade of airfoils including splitter vanes. Supersonic flow enters the cascade and subsonic flow leaves the system; thus, flow through a section of blading in a converging compressor annulus is simulated. The accuracy of the numerical calculations was tested against appropriate experimental data, the flow field results were studied to learn more about such cascade flow fields, and these numerical data were used to help determine the validity of simulating flow in a converging axial compressor annulus with a cascade having convergent sidewalls.

To properly address such a complex viscous, three-dimensional flow problem requires solution of the steady, three-dimensional Reynolds-averaged Navier-Stokes equations. Inviscid quasi-three-dimensional methods, such as those of Hearsey[1], Wennerstrom[2], and Katsanis and McNalley[3], do not properly account for viscous effects nor three-dimensionality. Three-dimensional, inviscid relaxation techniques with viscous terms treated as source terms, such as the method of Dodge[4,5], are useful for weak interactions. However, a strong interaction, with a strong three-dimensional vortical flow in the separated region, is beyond the scope of these techniques. Time-dependent solutions of the three-dimensional, Reynolds-averaged Navier-Stokes equations are now possible, as evidenced by the work of Steger and Pulliam[6]; however, such methods are limited by the speed and storage capacity of present day computers

1

such as the CDC 7600. Therefore, an iterative solution of the steady, Reynolds-averaged, three-dimensional, Navier-Stokes equations appears to be the most viable alternative.

A computer code, called VANS*, was the starting point for this numerical investigation. The VANS code solves the time-independent, three-dimensional Navier-Stokes equations on blade-to-blade computational surfaces. This code, developed from first principles at NASA Ames Research Center, is briefly described in Reference 7. Two of the main features of the VANS code are that (1) it performs computations along the streamline-like lines of the finite difference mesh in each blade-to-blade surface, and (2) it employs vector coding. The IFFC** computer code, which was developed at NASA Lewis Research Center[8], performs blade-to-blade computations along the potential-like lines of the finite difference mesh and is written in FORTRAN. The streamline-like-mode of computation reduces the number of branch points in the computer code and the vector coding makes the arithmetic more efficient. The present version of the VANS computer code is 88% faster than the IFFC computer code on the CDC 7600 computer.

Under NASA Lewis sponsorship the IFFC computer code was employed to generate a blade-to-blade iterate for a backswept, centrifugal impeller operating at 75000 rpm, with a tip diameter of 6.28 in, and a compressor design pressure ratio of $3:1$[8]. The calculated blade-to-blade flow field contained a leading edge suction surface separation, significant boundary layer flows along

---

*The letters VANS stand for Vectorized Asymmetric Navier-Stokes Code.
**The letters IFFC stand for Impeller Flow Field Calculator Code.

the pressure and suction blade surfaces, and a mixed supersonic-subsonic region at the inducer. In general, the blade-to-blade flow field contained significant differences from the inviscid, quasi-three-dimensional flow field[3] which served as the zeroth iterate.

In a subsequent follow-on program[9], the VANS blade-to-blade computer code was revised to solve the equations of motion on cross-sectional surfaces. Based on the blade-to-blade field as the previous iterate, the VANS computer code was employed to generate a cross-sectional iterate for the backswept centrifugal impeller. The calculated cross-sectional flow field duplicated the leading edge suction surface separation computed earlier, and in addition contained three other fluid-mechanical phenomena. First, it was found, in cross-sectional planes tipped normal to the blading, that the cross-sectional relative velocity field exhibited a large vortex. This vortex was quite pronounced in the inducer region. Second, a standing pressure wave was recorded along the hub and shroud of the system. The wave-length of this disturbance was correlated to the time of travel of a sound signal from shroud to hub. Furthermore, measurements of time-averaged shroud pressures indicated the presence of such a wave. Third, the flow separated along the shroud of the system near the discharge. The leading edge suction surface separation and shroud separation produced relative total pressure losses at the discharge. The standing pressure wave distorted the discharge flow field which resulted in losses in the diffuser of the centrifugal compressor.

3

In this research effort splitter vane logic was developed and incorporated into the blade-to-blade and cross-sectional versions of the VANS computer codes, and the supersonic compressor cascade problem was solved.

The VANS computer codes and the numerical method they embody are described in Section 2.0, turbulence and transition models are discussed in Section 3.0, and the cascade geometry and input conditions are presented in Section 4. Section 5 presents the blade-to-blade solution, or first iterate, Section 6 presents the cross-sectional solution, or second iterate, and Section 7 outlines the principal conclusions and recommendations of this research effort.

SECTION II

THE VANS COMPUTER CODES

2.1 Formulation of Cascade Problem

A set of finite difference analogs of the full three-dimensional, compressible Reynolds-averaged, Navier-Stokes equations has been developed and programmed. In addition to three-dimensionality and compressibility, the following effects are included:

1) Splitter vane geometry

2) Transition and turbulence

3) Arbitrary cascade geometry

4) Shock waves

A solution to these finite difference equations is obtained in the following manner. Starting from a known inviscid, quasi three-dimensional solution, in this particular case the inviscid field generated by the method of Hearsey and Wennerstrom[1,2], we calculate the viscous effects through iteration. Certain terms of the finite difference equations (FDE) are evaluated from the inviscid solution and other terms are evaluated directly. Terms evaluated from the inviscid solution are designated "elliptic source terms", while those evaluated directly are designated "parabolic terms".

The distribution of the elliptic source terms and parabolic terms in the FDE depends on the mode of marching. At present two modes of marching are contemplated.

1) The FDE are solved on blade-to-blade surfaces which move from the case of the cascade to its symmetry plane.

2) The FDE are solved on cross-sectional surfaces, which move from upstream of the cascade blading to discharge.

5

Each method of marching results in its own set of elliptic source terms and parabolic terms.

For illustrative purposes we start with a schematic of one blading passage for a compressor cascade shown in Figure 1. The case of the system and its symmetry plane are indicated in the figure. The surface labelled "pressure surface" is like the windward side of an airfoil, while the surface, labelled "suction surface" is like the leeward side of an airfoil. In the blade-to-blade mode of marching, the computation takes place on a blade-to-blade surface which extends from the leading to the trailing edge of the cascade blade , and moves from the case to the symmetry plane during an iteration. The blade-to-blade method of marching is illustrated in the blade passage schematic shown in Figure 2. The x, y and z coordinates of Figure 2 represent a left-handed, orthogonal, curvilinear coordinate system. The z-direction is proportioral to the time-like-variable, t, with the calculation taking place in the (x,y) blade-to-blade surfaces. The (x,y) blade-to-blade surfaces move from the case to the symmetry plane of the cascade. This mode of marching accounts for two very important fluid mechanical effects that occur in three-dimensional cascades.

1) Upstream influence effects. The flow becomes subsonic within the blading passage; hence, downstream conditions influence upstream conditions. Since each blade-to-blade surface extends from the leading to trailing edges of the cascade blades, the downstream flow can influence the upstream flow as the blade-to-blade surface moves from the case to the symmetry plane.

2) Blade boundary layer separation. Separations, which occur on the blade surfaces, produce vortices whose axes are nearly

6

normal to the blade-to-blade surfaces. Thus, the vortices themselves are contained in the blade-to-blade surface and are easily calculable.

In the cross-sectional mode of marching, we move down the channel, from upstream of the leading edge of the cascade blade to downstream of the trailing edge of the cascade blade, in cross-sectional surfaces normal to the case surface. A schematic of the blade passage with the cross-sectional surface indicated is presented in Figure 3. The z-direction, i.e., the time-like-coordinate is now normal to the (x,y) cross-sectional surface of Figure 3. The (x,y) cross-sectional surfaces move from the leading to trailing edges of the cascade blades. This mode of marching accounts for two additional fluid mechanical effects that occur in cascades.

3) Channel corner vortices. At the junctions of the blades and the case, vortices usually form whose axes are generally normale to the cross-sectional surfaces; hence, the corner vortices would be contained in these surfaces and are easily calculable.

4) Symmetry plane effects. The symmetry plane imposes a frictionless flow boundary condition on the system, as well as a condition of zero flow normal to the symmetry plane. Effects of these boundary conditions are calculable in this mode of marching.

To properly solve for a cascade flow field, an iteration procedure with both modes of marching is required. The procedure is as follows. Starting from an inviscid solution as the "zeroth" iterate, we determine the first viscous iterate by marching in blade-to-blade surfaces which move from the case to the symmetry plane.

7

Based on the first iterate we determine a second viscous iterate by marching in cross-sectional surfaces which move from the leading to trailing edge of the cascade blade. In this way the four principal cascade fluid-mechanical effects, described above, can be accounted for. The second iterate is a good engineering solution to the three-dimensional, compressible, Reynolds-averaged, Navier-Stokes equations for flow in a supersonic compressor cascade. A third iterate, which is comprised of an additional blade-to-blade solution, is required to demonstrate convergence of this numerical method.

The differential equations of motion in orthogonal, curvilinear, Eulerian coordinates, x, y and z are presented in Appendix A. Integral equations solved on either blade-to-blade or cross-sectional surfaces are presented in Appendices B and C. In addition the continuity equation is derived in Appendix B.

2.2 Blade-to-Blade and Cross-Sectional VANS Computer Codes

The integral equations of Appendix B are equally applicable to either the blade-to-blade or cross-sectional modes of marching. Therefore, the principal differences between the blade-to-blade version of VANS, i.e., "VANS-BB", and the cross-sectional version of VANS, i.e., "VANS-CS" are in the boundary conditions and the implementation of the turbulence model. The blade-to-blade and cross-sectional turbulence models are discussed in Sections 3.2 and 3.3, respectively. Boundary conditions are described for the blade-to-blade version of VANS in Section 5.3, while cross-sectional boundary conditions are described in Section 6.3.

8

SECTION III

TURBULENCE AND TRANSITION

3.1 Turbulence and Transition Model for Computation of Flow in a
Compressor Cascade

An algebraic turbulence model, originally formulated by Rose[10],
was selected for the computation of turbulent flow in a compressor
cascade. The model is, in effect, the mixing length theory to
which relaxation along a streamline is incorporated. All versions
of available algebraic models are discussed. A criterion for
boundary layer transition is also presented.

3.1.1 Turbulence Modelling

Numerical modelling of turbulence has become quite practical
in the past decade with the advancement of high-speed computers.
Though a universal model with wide range of applicability is far
from reality, there is ample evidence that existing models have
served well even in complex situations such as shock-wave boundary-
layer interaction. All models of turbulence are supposed to be
general in scope, and until recently, cross-comparisons between
models (mainly studies done at NASA-Ames[10,11,12]) are few. For
flows in a compressor cascade, there is no investigation as to the
best turbulence model to employ. Thus a good rule in selection
seems to be "the simpler the better."

The usage of numerical models naturally bypasses the more
fundamental approach to turbulence studies via statistical theory,
which might be at times academically pleasing but unrealistic in
engineering applications. In general, turbulence modelling is
divided into two categories: the algebraic models such as mixing

length theory, and the transport models which are described by one or more differential equations governing some quantity like turbulence energy, turbulence vorticity or shearing stress. The original work of Prandtl and its subsequent extension by Cebeci and Smith, i.e., C-S model[13,14], Rose model[10], etc. are examples of the first class; the classical Kolmogorov model[15] and the Saffman model[16] fall into the latter category. In adopting a transport model, one must solve, in addition to the basic conservation laws, other differential equations from which turbulence stresses are determined. Success of transport models so far has been confined to simple problems such as attached turbulent boundary layers with small pressure gradients. A comparative study by Balwin and McCormack[12] has concluded that Saffman's transport model and the C-S mixing length theory suffer a similar degree of inaccuracy in the hypersonic boundary-layer shock-wave interaction problem.

Let us present herein the Saffman model[16] for illustration. The model contains two variables: the energy density e and a pseudo-vorticity, Ω, which are assumed to satisfy the following non-linear diffusion equations.

$$\frac{d}{dt}(\bar{\rho}e) + \frac{d}{dx_j}(\bar{\rho}\bar{u}_j e) = \left[\alpha^*(2 S_{ij} S_{ij})^{\frac{1}{2}} - \beta^* \bar{\rho}\Omega\right]\bar{\rho}e$$
$$+ \frac{d}{dx_j}\left[(\mu + \sigma^* e/\Omega)\frac{de}{dx_j}\right] - \xi \bar{\rho}e \frac{\partial \bar{u}_k}{\partial x_k} \tag{1}$$

$$\frac{d}{dt}(\bar{\rho}\Omega) + \frac{d}{dx_j}(\bar{\rho}\bar{u}_j \Omega^2) = \left[\alpha\left\{\left(\frac{\partial \bar{u}_i}{\partial x_j}\right)\left(\frac{\partial \bar{u}_i}{\partial x_j}\right)\right\}^{\frac{1}{2}} - \beta \bar{\rho}\Omega\right]\bar{\rho}\Omega^2$$
$$+ \frac{d}{dx_j}\left[(\mu + \sigma e/\Omega)\frac{d\Omega^2}{dx_j}\right] \tag{2}$$

where: t = time

   x_j = Cartesian coordinates (j = 1,2,3)

$\bar{\rho}$ = mean density

$\bar{u}_j$ = mean velocity components in the jth direction

μ = molecular viscosity coefficient

S_{ij} = mean rate of strain tensor

The numbers $\alpha, \alpha^*, \beta, \beta^*, \sigma, \sigma^*, \xi$ are assumed by the model to be universal constants.

$$\sigma = \sigma^* = \tfrac{1}{2}$$
$$\alpha^* = 0.3$$
$$\beta^* = \alpha^{*2}$$
$$\tfrac{5}{3} \leq \beta/\beta^* \leq 2$$
$$\alpha = \alpha^* \left(\beta/\beta^* - 4\sigma \frac{\bar{K}^2}{\alpha^*} \right)$$

ξ = 2.5, based on experimental data,

and K is the Karman constant.

This set of equations is integrated with an appropriate set of boundary conditions (which are by no means trivial) to yield e and Ω. The eddy viscosity ϵ is related to e and Ω by

$$\epsilon = e/\Omega \qquad (3)$$

Saffman's model is but one of the many available schemes governed by two equations; some of the others are Chou (1945)[17], Harlow-Nakayama (1968)[18], Jones-Launder (1972)[19], Ng-Spalding (1972)[20], etc. They all have a set of empirical constants, some even parametric functions. The complexity of the mathematical system and the uncertainty in those constants are inherent with all the models. Moreover, a set of non-linear diffusion equations generally introduces a new

11

time scale in the computation, which is often substantially smaller
than the convective or diffusive time scale for laminar type compu-
tation. The two-point boundary value problem also poses a tedious
numerical task. However, the advantage in this kind of turbulence
modelling is also clear; they all attempt to depict the physics of
turbulence transport, generation, dissipation and diffusion. In
addition, some models (such as Saffman's) show the correct analytical
behavior near the wall (as demanded by the law of wall). The pre-
dictive capabilities for incompressible boundary layer flows by
those models are convincingly established. Turbulent flows in more
than two spatial dimensions, including separation, compressibility,
rotational effects, and containing boundary layers interacting with
shock waves have not been subject to examination by those models*.
In short, the transport models, as promising as they are, have yet
to be thoroughly tested by problems more complex than plane boundary
layer flows.

In view of the three dimensionality of the cascade problem, the
desired economy in computation, and the added degree of complication
in the nonlinear equations, we must seek an alternative to the form-
ulation by turbulence model equations. The alternative should be
able to render a reasonably good description of the turbulent bound-
ary layer development without a disproportional amount of computation
time.

---

*Wilcox[21], applying Saffman's model, has shown good results in the study
of turbulent boundary separation and reattachment at moderate (2.96)
Mach number.

3.1.2 Algebraic Turbulence Models

The mixing length theory, originated by Prandtl[22], provides the foundation to all algebraic models. Modifications introduced by van Driest[23], Cebeci and Smith[13,14], and recently Balwin and Rose[10], Shang and Hankey[24], and Deiwert[11] all direct to improve the applicability of the model. Algebraic models bypass the necessity of solving additional differential equations. From a computational stand-point, the eddy viscosity based on an algebraic model is post-pro-cessed from mean-flow information. Our past application of the CS mixing length theory to internal flow problems in an impeller has shown good qualitative results. Quantitative comparison is not pos-sible due to the complete lack of experimental data. Hence, some version of an algebraic turbulence model is preferred to the more complex transport model. Despite the mixing-length common ingred-ient, there are variations in each individual formulation. The var-iations range from the unmodified theory to a relaxation model incor-porating special treatment for the separated regions. The relaxation model was found significantly better than the unmodified algebraic model. According to Shang and Hankey[24], it was significantly better than the Saffman's transport model for flow over a flat plate. Since separation in the cascade passage is a real possibility, incorporation of the relaxation effect becomes quite desirable. For a detailed comparison of various formulations, we list them in Table I.

The formulation we shall adopt in the cascade problem is basi-cally a hybrid relation primarily based on Rose's relaxation model and the modification suggested by Deiwert. Ingredients of the present algebraic model are blocked in heavy-lined rectangles in the preceding

13

$$\tau_{xy} = (\mu + \rho\epsilon)\left(\frac{\partial u}{\partial y} + \frac{\partial v}{\partial x}\right)$$
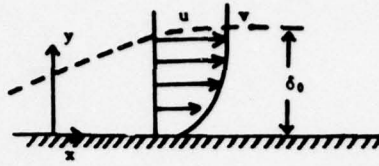
	C-S METHOD	ROSE-BALWIN BASELINE	ESCUDIER	ROSE-BALWIN RELAXAT
INNER REGION	$\epsilon_1 = \ell_1{}^2 \left\|\frac{\partial u}{\partial y}\right\|$ where $\ell_1{}^2 = k_1^2 y^2 D^2$ $k_1 = 0.4$ $D = 1-\exp\left(-\frac{Y}{A}\right)$ $A = 26\nu / \sqrt{\frac{\tau_w}{\rho} + \frac{d\rho}{dx}\frac{y}{\rho}}$	$\boxed{\epsilon_1 = \ell_1{}^2 \left\|\frac{\partial u}{\partial y} + \frac{\partial v}{\partial x}\right\|}$ where $\ell_1{}^2 = k_1^2 y^2 D^2$ $k_1 = 0.4$ $D = 1-\exp\left(-\frac{Y}{A}\right)$ $A = 26\nu_w / \sqrt{\frac{\tau_w}{\rho_w}}$ Subscript w = wall condition	Same as left hand side.	Same as Rose-Balwin B
OUTER REGION	$\epsilon_0 = k_2 u_{max} \delta_1{}^*/\gamma$ where $k_2 = 0.0168$ $\delta_1{}^* = \int_0^\delta \left(1-\frac{u}{u_{max}}\right) dy$ $\gamma = 1 + 5.5\left(\frac{y}{\delta}\right)^6$	$\epsilon_0 = k_2 u_{max} \delta_1{}^*/\gamma$ where $k_2 = 0.0168$ $\delta_1{}^* = \int_0^\delta \left(1-\frac{u}{u_{max}}\right) dy$ $\gamma = 1 + \left(\frac{y}{\delta}\right)^6$	$\epsilon_0 = \ell^2_{max} \left\|\frac{\partial u}{\partial y} + \frac{\partial v}{\partial x}\right\|$ where $\ell_{max} = 0.09\delta$	$\boxed{\epsilon_0 = \ell^2_{max} \left\|\frac{\partial u}{\partial y} + \frac{\partial v}{\partial x}\right\|}$ where $\ell_{max} = 0.09\delta_0$
SELECTION	$\epsilon = \text{Min}(\epsilon_1, \epsilon_0)$	$\boxed{\epsilon = \text{Min}(\epsilon_1, \epsilon_0)}$	$\epsilon = \text{Min}(\epsilon_1, \epsilon_0)$	$\epsilon = \text{Min}(\epsilon_1, \epsilon_0)$
RELAXATION	NO	NO	NO	$(\rho\epsilon) = (\rho\epsilon)_0 + [(\rho\epsilon)_{eq} -$ $[1-\exp(-$ $\alpha = \begin{cases} \infty & \text{if } (\rho\epsilon)_{eq} < (\rho\epsilon \\ 1/5 & \text{otherwise} \end{cases}$

1

ROSE-BALWIN RELAXATION	SHANG & HANKEY	DIEWERT MODEL 1	DIEWERT MODEL 2	DIEWERT MODEL
Same as Rose-Balwin Baseline	$\epsilon_i = \ell_i^2 \frac{\partial u}{\partial y}$ where ℓi is the same as Rose-Balwin Baseline	Same as Rose-Balwin Baseline.	$\boxed{\epsilon_i = \ell_i \sqrt{\left(\frac{\partial u}{\partial y}\right)^2 + \left(\frac{\partial v}{\partial x}\right)^2}}$ where ℓi is the same as Rose-Balwin Baseline	Same as Mode...
$\boxed{\epsilon_0 = \ell_{max}^2 \left\| \frac{\partial u}{\partial y} + \frac{\partial v}{\partial x} \right\|}$ where $\ell_{max} = 0.09\delta_0$	$\epsilon = 0.0168\, u_{max}\, \delta_i^*$ where $\delta_i = \int_0^\infty (1 - \frac{u}{u_{max}})dy$	Boundary Layer $\epsilon_0 = \ell^2 \left\| \frac{\partial u}{\partial y} + \frac{\partial v}{\partial x} \right\|$ where $\ell = 0.07\,(\delta - y_0)$ y_0 = value of y at zero velocity Wake $\epsilon_0 = 0.001176\,(\delta - y_0) \|u_\delta - u_\ell\|$	$\epsilon = \frac{0.0168\, u_\delta \delta_i^*}{1 + \left(\frac{y - y_0}{\delta}\right)^6}$ where $\delta_i^* = \int_{y_0}^\delta (1 - \frac{u}{u_\delta})\, dy$	ϵ, same as Model... $\delta_i^* = \int_{y_{ds}}^\delta (1 - \frac{u}{u}...)$ where y_{ds} = val... dividing stream...
$\epsilon = Min\,(\epsilon_i, \epsilon_0)$	$\epsilon = Min\,(\epsilon_i, \epsilon_0)$	Prescribed	Boundary Layer $\epsilon = Min\,(\epsilon_i, \epsilon_0)$ Separated Bubble $\epsilon = \ell_i^2 Min \{[(\frac{\partial u}{\partial y})^2 + (\frac{\partial v}{\partial x})^2]^{\frac{1}{2}}, \frac{u\delta}{\delta}\}$	Separated bubble – $\epsilon = 0.0168\, u_\delta\, \delta_i^*$ [... Separated bubble – $\epsilon = 0.0168\, u_\delta \delta_i^*$
$) = (\rho\epsilon)_0 + [(\rho\epsilon)_{eq} - (\rho\epsilon)_0]$ $[1 - exp(-\frac{\alpha(x - x_0)}{\delta_0})]$ if $(\rho\epsilon)_{eq} < (\rho\epsilon)_0$ 1/5 otherwise	$\epsilon = \epsilon_{eq} + (\epsilon_0 - \epsilon_{eq})\, exp(-\frac{\Delta x}{\lambda})$ $= \{ \begin{matrix} 10\delta, & \text{Boundary layer} \\ 2\delta, & \text{Mixing layer} \end{matrix}$	NO	NO	NO

14

γ

FORMULATIONS

DIEWERT MODEL 1	DIEWERT MODEL 2	DIEWERT MODEL 3 BASELINE	DIEWERT MODEL 4 RELAXATION
Same as Rose-Balwin Baseline.	$$\epsilon_i = \ell_i^2 \sqrt{\left(\frac{\partial u}{\partial y}\right)^2 + \left(\frac{\partial v}{\partial x}\right)^2}$$ where ℓ_i is the same as Rose-Balwin Baseline	Same as Model 2	Same as Model 3
__dary Layer__ $\epsilon = \ell^2 \left\|\frac{\partial u}{\partial y} + \frac{\partial v}{\partial x}\right\|$ __re__ $\ell = 0.07 (\delta - y_0)$ = value of y at zero velocity $= 0.001176 (\delta - y_0)$ $- u_\ell\|$	$\epsilon = \dfrac{0.0168\, u_\delta \delta_1^*}{1 + \left(\frac{y - y_0}{\delta}\right)^6}$ where $\delta_1^* = \int_{y_0}^{\delta} \left(1 - \frac{u}{u_\delta}\right) dy$	ϵ, same as Model 2 except $\delta_1^* = \int_{y_{ds}}^{\delta} \left(1 - \frac{u}{u_\delta}\right) dy$ where y_{ds} = value of y at dividing streamline	Same as Model 3
Prescribed	Boundary Layer $\epsilon = \text{Min} (\epsilon_i, \epsilon_0)$ Separated Bubble $\epsilon = \ell_i^2 \text{ Min} \left\{ \left[\left(\frac{\partial u}{\partial y}\right)^2 + \left(\frac{\partial v}{\partial x}\right)^2\right]^{\frac{1}{2}}, \frac{u\delta}{\delta} \right\}$	Separated bubble - wall region $\epsilon = 0.0168\, u_\delta\, \delta_1^* \left[\frac{y}{y_{ds}} (1 - \exp\left(\frac{y}{A}\right)\right]^2$ Separated bubble - wake region $\epsilon = 0.0168\, u_\delta \delta_1^*$	Same as Model 3
NO	NO	NO	$\epsilon(\xi) = \epsilon(\xi - \Delta\xi) + [\epsilon_{eq}(\xi) - \epsilon(\xi - \Delta\xi)] [1 - \exp(-\Delta\xi/\lambda)]$ $\lambda = 1\delta \sim 10\delta$

3

table. The model for the turbulence stress τ_{ij} can be summarized as follows

$$\tau_{ij} = \bar{\rho}\,\epsilon\left[\ \frac{\partial \bar{U}_i}{\partial X_j} + \frac{\partial \bar{U}_j}{\partial X_i} - \frac{2}{3}\,\frac{\partial \bar{U}_k}{\partial X_k}\,\delta_{ij}\right] - \frac{2}{3}\,\bar{\rho}\,\bar{e}_s\,\delta_{ij} \qquad (4)$$

with $\rho\,\bar{e}_s = -\frac{1}{2}\,\tau_{ii}$

The eddy viscosity ϵ is estimated by the mixing length theory which subdivides the shear layer into an inner and an outer region.

Inner region

$$\epsilon_I = \ell_I^2\sqrt{\left(\frac{\partial \bar{U}_i}{\partial X_j}\right)^2 + \left(\frac{\partial \bar{U}_j}{\partial X_i}\right)^2} \qquad (5)$$

where: $\ell_I = k_1 yD$

$k_1 = 0.4$

y = normal distance from the nearest wall

D = 1 - exp(y/A)

$A = 26\,\nu_w\,\Big/\sqrt{|\tau_w|/\bar{\rho}}$

ν_w = kinematic viscosity coefficient at the nearest wall

τ_w = shearing stress at the nearest wall

Outer Region

$$\epsilon_0 = \ell_{MAX}^2\sqrt{\left(\frac{\partial \bar{U}_i}{\partial X_j}\right)^2 + \left(\frac{\partial \bar{U}_j}{\partial X_i}\right)^2} \qquad (6)$$

where: $\ell_{max} = 0.96\,\delta_0$

δ_0 = boundary layer thickness

16

Selection

$$\epsilon_{eq.} = \text{Min}\,(\epsilon_I, \epsilon_0) \tag{7}$$

Relaxation along a streamline-like trajectory

$$\epsilon(\xi) = \epsilon(\xi - \Delta\xi) + \left[\epsilon_{eq.}(\xi) - \epsilon(\xi - \Delta\xi)\right]\left[1 - \exp\left(-\frac{\Delta\xi}{\lambda}\right)\right] \tag{8}$$

where

$$\lambda = \begin{cases} \infty, \text{ if } \quad \epsilon_{eq.} < \epsilon(\xi - \Delta\xi) \\ 5\delta_0, \text{otherwise} \end{cases}$$

and ξ is a parameter defined along a streamline.

Two major components, due to Deiwert, are introduced into Rose's formulation. One is the adoption of $\sqrt{\left(\frac{\partial \bar{u}_i}{\partial x_j}\right)^2 + \left(\frac{\partial \bar{u}_j}{\partial x_i}\right)^2}$ in place of $\left|\frac{\partial \bar{u}_i}{\partial x_j} + \frac{\partial \bar{u}_j}{\partial x_i}\right|$ to avoid the complete vanishing of ϵ in a recirculating zone. Another one is the modification of the relaxation process in which $\epsilon(\xi - \Delta\xi)$ is used in place of a fixed ϵ evaluated at some reference station. Moreover, Deiwert found that relaxation over a streamline-like contour was more appropriate particularly for flows over a curved boundary, such as airfoil or turbine blade. Both modifications, indeed minor in nature, are convenient to implement with our computer code in which the scanning is done along streamline-like trajectories. The necessity of incorporating the relaxation effect has been substantiated by Baldwin and Rose[10], Deiwert[11], Shang and Hankey[24]. Its usefulness for flows in a cascade passage will be born out in our forthcoming computation.

17

3.1.3 Transition to Turbulence

Laminar flow at large Reynolds numbers becomes unstable, then the growth of disturbance in the boundary layer builds up until transition to turbulence occurs. The point of transition is strongly affected by the streamwise pressure gradient and the turbulence level of the free stream. To account for these factors, several empirical methods are available (for example, van Driest and Blumer, Crabtree, Granville, Smith and Gamberoni, van Ingen, Michel). It is not possible to give a thorough comparison for those methods. In our blade-to-blade computation for flows in impeller passage, both Granville[25], and Michel's[26] formulations were examined. We found that Michel's simple algorithm provided a clear-cut prediction of transition point and it was extremely easy to implement. Since boundary layer transition is such a dubious subject in numerical computation, our guideline in the selection of a criterion is again "the simpler the better!" Unless future experiments contradict our selection, we shall adhere to Michel's criterion for the present application. The criterion gives a transition Reynolds number, $(Re_\theta)_{trans}$, based on the local Reynolds number Re_x.

$$(Re_\theta)_{trans} = 1.17 \left(1 + \frac{22400}{Re_x} \right) Re_x^{0.46} \tag{9}$$

The local Re_θ can be estimated from the incompressible momentum thickness θ_i.

$$\theta_i = \int_0^\delta \frac{\bar{u}}{\bar{u}_{max}} \left(1 - \frac{\bar{u}}{\bar{u}_{max}} \right) dy \tag{10}$$

18

If the local Re_θ is larger than $(Re_\theta)_{trans}$, transition to turbulent flow has taken place. Michel's criterion, which resulted from correlation of experimental data, is supposedly valid for the range of Re_x between 0.1×10^5 and 60×10^6. Criterion of this nature signifies that transition to turbulence occurs at a point, rather than in a region, and relaminarization is not possible. A.M.O. Smith had compared Michel's algorithm against Granville's, Smith found the simple criterion of Michel quite satisfactory in the description of transition to turbulence.

3.2 Blade-to-Blade Turbulence Model

The turbulence and transition models, as described in Section 3.1, were formulated, coded, merged into the VANS-BB code and de-bugged. The turbulence formulation considered only the components of velocity in a given blade-to-blade surface.

Our turbulence model is in effect the mixing-length formulation generalized for internal flows with a splitter vane and included re-laxation effects along streamlines. The transition criterion is the semi-empirical one proposed by Michael. To accomplish these computa-tions, consistent with the VANS scanning logic, four new subroutines were developed. The subroutines were structured as components in VANS; hence, any modification or even overall change of the basic theory would not require an overall change of the VANS code. The four components can best be described in tabulated form in the following.

Subroutine	Called from	Major functions
TURB	MVS* in VANS	1. Compute geometric and shear stress quantities at all walls. For a blade-to-blade geometry with a splitter vane, there are possibly four solid walls.
		2. Compute integral thickness at walls for all boundary layers.
		3. If transition has taken place, use mixing length theory to compute the eddy viscosity coefficient.
INTER	TURB	Find the distance between any two points in a curvilinear coordinate system. The distance is required by the mixing length theory.
TRANS	TURB	Examine if transition has taken place along any streamline, according to Michel algorithm. Relaminarization is not possible along a given streamline.
MIXL	TURB	Compute the eddy viscosity coefficient according to the mixing-length theory. MIXL is called only after transition has taken place.

3.3 Cross-Sectional Turbulence Model

Computation in the cross-sectional plane upstream of the splitter vane included the three boundary layers which influence the eddy viscosity at a given point in the flow field. The pressure surface boundary layer, the case boundary layer, and the suction surface boundary layer. All three layers were considered to determine the eddy viscosity at a given point. In a cross-sectional plane containing the trace of the splitter vane, two additional boundary layers must be considered; however, only the main blade and case boundary layers were employed to compute the eddy viscosity. The extension of the mixing length theory to this case is consistent with the practice discussed by Lauder and Spalding for flows in ducts[27], and for the mixing of two streams[28].

---

*The MVS subroutine of VANS computes the viscous stresses on each blade-to-blade surface.

A cross-sectional turbulence model was formulated, incorporated into the VANS cross-sectional computer code, and debugged. The main features of the cross sectional model are as follows:

(1) The mixing-length theory with streamwise relaxation, as formulated by Rose, is adapted. The model is capable of estimating the eddy viscosity coefficient for a specific turbulent boundary layer.

(2) Michel's empirical transition criterion is used for the location of transition from laminar to turbulent flow.

(3) The preceding models, originally formulated for steady flow with small boundary layer curvature, are used in the space-marching computation with curvilinear coordinates. Past comparison with experimental data seems to support this adaption.

(4) The eddy viscosity coefficient at any point in a passage is determined by the nearest turbulent boundary layer.

Implementation of this formulation for the cross-sectional surfaces was done through coding consisting of four subprograms:

TURB--The main program for turbulence computation in which all necessary information for the mixing-length theory are computed, updated and stored.

INTER--An auxiliary program in which the normal distance from any internal point in the passage to any point on a surface is computed.

TRANS--A short program in which Michel's transition criteria is examined for any boundary layer.

MIXL--A short program which calculated the eddy viscosity coefficient at any internal point in the passage according to the mixing length theory.

21

SECTION IV

CASCADE GEOMETRY AND INPUT CONDITIONS

The supersonic compressor cascade geometry numerically inves-
tigated was tested by Holtman, McClure, and Sinnet[29]. A schematic
of the compressor cascade is shown in Figure 4. The compressor
cascade is comprised of six blades and five splitter vanes. The
geometry of the cascade blades and splitter vanes is identical in
all planes parallel to the direction of free stream flow; hence,
the cascade is two dimensional in this respect. However, contoured
sidewalls are utilized in the cascade to obtain the required stream-
tube convergence; thus, the three dimensionality of the flow. The
effective axis of the system, designated as the X_3 direction, is
indicated in Figure 4. The contoured sidewalls and symmetry plane
are indicated in Figure 5, while a blading passage of the cascade
is shown in Figure 6. The main cascade blade has a chord of 3
inches and an axial length of 1.8396 inches.

Input flow properties for the cascade problem are as follows:

freestream Mach number = 1.46

mass flux per passage = .656772 lb/sec

medium is air with   = 1.4
  specific heat
  ratio γ

freestream Reynolds   = 1.3575×10^6
  number based on
  chord

Measurements of static pressure, total pressure, and Mach num-
ber were made in the wake of the cascade. The measurement axial
station was located at the symmetry plane approximately .49 inches
aft of the cascade exit. This corresponds to about 16 percent of

22

a chord aft of the cascade. Thus, mass averaged static pressures,
total pressures, and Mach numbers are <u>not</u> indicative of the true
cascade exit conditions. However, these mass averaged quantities
are tabulated below:

    mass averaged static pressure ratio = 1.883
      across cascade at symmetry plane

    mass averaged stagnation pressure   = .86
      ratio across cascade at symmetry
      plane

    mass averaged wake Mach number at   = .837
      symmetry plane

23

SECTION V

DEVELOPMENT OF BLADE-TO-BLADE SOLUTION: THE FIRST ITERATE

5.1 The Inviscid Solution: Zeroth Iterate

The inviscid solution to the cascade problem was generated by Capt. W.A. Buzzel of the Air Force Aero-Propulsion Laboratory. This solution constitutes the zeroth iterate in an iteration procedure to solve for the viscous flow field within the compressor cascade. In this section the cascade problem is briefly described, the method of obtaining its inviscid solution is briefly discussed and the inviscid streamlines are presented.

The compressor cascade is comprised of six blades and five splitter vanes. The geometry of the cascade blades and splitter vanes is identical in all planes parallel to the direction of free stream flow; hence, the cascade is two-dimensional in this respect. However, contoured sidewalls are utilized in the cascade to obtain required stream-tube convergence; thus, the three-dimensionality of the flow. Input flow properties for the cascade problem are presented in Section 4.

The inviscid solution was generated by Air Force Aero-Propulsion Laboratory Program UDO300. This computer code integrates the axisymmetric radial equilibrium equation of turbomachinery in a meridional plane associated with a mean stream surface through the blading passage[1]. Forces acting between the cascade blades and fluid are taken into account by body force terms in the radial equilibrium equation[2]. The splitter vane is accounted for in the continuity equation as blockage. Isentropic flow is assumed in obtaining the inviscid flow field.

24

Due to the axial symmetry built into Computer Code UDO300,
the essentially 2-D cascade problem is solved as an axial compres-
sor single-stage problem at large radius. The solution takes place
in the axial coordinate X_3 and a radius of 10000 inches is added
to the normal coordinates of the contoured sidewalls to produce
the radial coordinate. In addition to the introduction of a large
radius, the compressor is rotated at 16.5 r.p.m. Therefore, an
equivalent axial compressor single-stage problem is solved by pro-
gram UDO300 to generate the inviscid field about the compressor
cascade.

The meridional projection of the streamlines on the mean
stream surface is presented in Figure 7. The ordinate of the
figure corresponds to the radius, while the abcissa corresponds
to the axial coordinate. Due to the introduction of cylindrical
coordinates the lower contoured wall now becomes the hub and the
upper contoured wall becomes the shroud or case. The vertical
lines of Figure 7 represent the computing stations for Program
UDO300. There are seven streamlines and twenty-six computing sta-
tions. The hub and case of the system are indicated in Figure 7.
By assuming a linear pressure distribution between the cascade
suction and pressure blade surfaces, the blade velocities, and
hence, loadings are estimated.

5.2 Mapping of Blade-to-Blade Surface from Cartesian to Curvi-
    linear Space

The curvilinear coordinate system employed by the VANS computer
code is axisymmetric and orthogonal. The axisymmetric condition im-
plies that the geometry of the hub and case lines of the machine

25

are bodies of revolution. To expedite solution of the effectively
two-dimensional cascade problem, the inviscid method of solving an
equivalent axial compressor flow field at large radius is followed.
The VANS numerical solution considers the same axial and radial
coordinates employed to generate the inviscid flow field. However,
the equivalent axial compressor geometry computed by VANS will not
rotate.

This section is concerned with the specification of the geometry
for the cascade problem in cylindrical and curvilinear coordinates.
The cascade geometry is first specified in cylindrical coordinates
r, θ, and X_3. Meridional traces of the radial and axial coordi-
nates of the hub and case of the system have already been presented
in Figure 7. The radial hub and case coordinates are presented as
functions of axial distance, X_3. These hub and case lines extend
upstream of the leading edge of the blades and downstream of their
trailing edge so that the flow field in the inducer and discharge
regions can be calculated directly from the equations of motion.
Figure 8 presents angular coordinates of the traces of the blading
surfaces on the hub. The cascade pressure surface, suction and
splitter vane are indicated in Figure 8.

A generalized, axisymmetric, orthogonal, curvilinear coordi-
nate system is used to solve the cascade problem. Consider the
curvilinear coordinates x, y, and z. The surfaces x = constant
are selected as meridional planes. The surfaces y = constant and
z = constant are obtained by rotating two orthogonal curves on
the meridional plane about the axis of rotation of the machine.
Figure 9 presents two families of orthogonal curves in the

26

meridional plane. The streamline-like curves are identical to the inviscid streamlines of Figure 7. These curves form the surfaces of revolution y = constant and z = constant. The curvilinear coordinate x is identical to the angular coordinate θ. The curvilinear coordinates y and z are related to distances along the streamline-like and potential-line-like lines of Figure 9, respectively.

Streamline-like-meridional curves are labeled with the parameter z and are calculated according to the following integral:

$$z = \frac{2}{r_0^2} \int_0^n r(\cos\lambda - \sin\lambda)\, dn'$$ (11)

where r is the local radius, r_0 is the hub radius at discharge of the system, n is the arc length along the upstream potential-like-line of Figure 9, λ is the angle that the streamline-like-lines of the system make with upstream potential-like line, and n^1 is a dummy variable. It is noted that the parameter z is nondimensional.

Potential-like meridional curves are labeled by the parameter y, which is a measure of distance along the hub. The following integral is used to define the y curvilinear coordinate

$$y = \frac{1}{r_0} \int_0^{m_h} dm_h'$$ (12)

where m_h is the arc length along the hub and m_h^1 is a dummy variable. As in the case of Equation (11), y is nondimensional.

Based on the above definitions of x, y, and z the metrics of the transformation and their derivatives can be evaluated at each of the coordinate points of Figure 9. Vavra[30] developed formulae

27

for the metrics and their derivatives in terms of local curvatures
and slopes. Based on known metrics and their derivatives at the
coordinate points of Figure 9, the metrics and their derivatives
at a given point in the meridional plane, i.e., P(y,z), can be
determined by interpolation.

The cascade geometry in cylindrical coordinates, defined in
Figures 7 and 8, is transformed to x, y, z space according to
Equations (11) and (12). The transformed geometry is shown in
Figures 10 and 11. Figure 10 shows the hub and case curves in
the (y,z) plane; these curves have now become straight lines.
Figure 11 presents traces of the blading on the hub blade-to-blade
surface in the (x,y) plane. The calculation takes place in the
(x,y) planes which move from the hub to the symmetry plane as the
z parameter increases from zero at the hub to .2868-03 at the sym-
metry plane.

5.3 Meshes, Boundary Conditions, and Initial Conditions
5.3.1 Finite Difference Mesh for Cascade Problem

The VANS computation takes place on (x,y) blade to blade sur-
faces which move from the hub to the symmetry plane and distort
as the blade surfaces distort. The VANS computer code has a sub-
routine which automatically develops the finite difference mesh in
accordance with the blade geometry. The finite difference mesh cor-
responding to the hub blade-to-blade surface is shown in Figure 12.
The mesh is formed by the intersection of 42 streamline-like lines
and 80 potential-like lines, i.e., 3360 points. The streamline-like
lines are spaced closer in the vicinity of the blades and splitter

28

plate than in center of the passage between a blade and splitter plate surface.

The Reynolds number at the cascade exit, based on the average inviscid velocity along the hub, average hub density, average hub viscosity, and distance along the hub, is Re = 7.53 x 10^5. The flow will surely go turbulent along the blade ; however, for purposes of mesh sizing a laminar boundary layer was considered. Based on flat plate theory the exit boundary layer thickness is 1.028 x 10^{-3} ft. Using a radius of 10000 inches this would give an angular increment of Δx = 1.233 x 10^{-6} radians. The mesh was sized such that one zone would exist in the laminar flat plate boundary layer at the cascade exit. Five or six zones should exist in the turbulent boundary layer which actually occurs in this case.

5.3.2 Boundary conditions for Blade-to-Blade Iterate

Identical boundary conditions are prescribed for all blade-to-blade surfaces. Let us consider the hub blade-to-blade surface of Figure 12. The boundary conditions are as follows:

1. No slip flow is imposed on the main cascade blade and splitter vane.

2. Periodic conditions are imposed on the lateral boundaries upstream of and downstream of the main blade.

3. The inviscid, or zeroth iterate, flow field properties are specified at the upstream boundary.

4. The static pressure is uniformly varied along the downstream boundary to maintain the passage mass flux. As the blade-to-blade surface moves from the hub to the symmetry plane, the mass flux at the downstream boundary is integrated and the back

29

pressure is varied to produce a mass flux equal to half the pas-
sage mass flux of .656772 lb/sec.

5.3.3 Inviscid Blade-to-Blade Field at Cascade Hub

The inviscid field for the cascade problem was solved for
by Capt. W. A. Buzzel, using the UDO 300 computer code. Buzzell solved
for the inviscid velocity field, while the energy and density fields
were determined as functions of the velocity field by invoking con-
stant rothalpy, and the isentropic flow assumptions.

As in the case of the impeller problems solved previously[8],
the inviscid solution served a dual purpose.

1) It was the zeroth iterate, i.e., used to evaluate the el-
liptic source-like-terms in the equations of motion.

2) The hub solution served as the initial conditions for the
viscous calculation.

The inviscid or zeroth iterate velocity field on the hub blade-
to-blade surface is discussed in Section 5.5.

5.4 Characteristic Time for Calculation

To run the cascade problem, the speed at which the (x,y) blade-
to-blade planes move from the hub to the shroud must be specified.
The curvilinear coordinate z is related to a time-like parameter t
as follows:

$$z = U_z t \tag{13}$$

Where U_z is the speed at which the (x,y) plane moves, and is nothing
more than a coordinate transformation*. The curvilinear coordinate
z is measured in radians and U_z is in units of feet per second, so

*See Appendix B for a derivation of the coordinate transformation
from z to t .

30

the parameter t has the units seconds per foot. The speed U_z must be small enough to permit viscous diffusion effects at the blade surfaces to build-up boundary layers which could subsequently separate, depending on the magnitude of the adverse pressure gradient.

The definition of the characteristic time for diffusion is based on the distance, Δm , between the suction surface leading edge and trailing edge at the hub, and the average inviscid velocity, $\overline{U}_h$, along the mid-channel plane at the hub. The characterisic time τ is then defined as follows:

$$\tau = \Delta m / \overline{U}_h \qquad (14)$$

It was found that Δm = .1642 ft and $\overline{U}_h$ = 812 fps; therefore, a characteristic time τ of .2022 ms results.

In the process of solving the cascade problem the (x,y) plane was moved at U_z = 355 fps. This speed permitted two characteristic times to pass as the blade-to-blade surface moved from the hub to the symmetry plane of the system.

5.5 Numerical Results of Blade-to-Blade Solution

The cascade problem was run through 5300 cycles; where, each cycle of computation corresponds to updating all the variables of motion on one blade-to-blade surface. In 5300 cycles the blade-to-blade surface was moved from the system's hub, where the z-coordinate is zero, to the symmetry plane, where the z coordinate is .2868 x 10^{-3}. The cascade blade-to-blade iterate required 3.68 hours on the CDC 7600 computer at Lawrence Berkeley Laboratory. There exist computation-time-reduction methods that can be incorporated into the VANS computer codes to reduce the computational time considerably; this subject is discussed in Section 7.

31

The results obtained are presented in the following format.

1) Velocity vector plots of the entire cascade flow field.

2) Velocity vector plots in the neighborhood of the splitter
    vane.

3) The inviscid field and flow in the symmetry plane.

5.5.1 Velocity Vector Plots of Entire Cascade Flow Field

Figure 13 presents the inviscid velocity field on the blade-
to-blade surface corresponding to the hub of the system. This field
represents the initial conditions for the computation. The vectors
are proportional to the local particle velocities, and their tails
emanate from the finite difference mesh in the blade-to-blade sur-
face. The plot is shown in the coordinates ℓ and m defined as
follows:

$$\left. \begin{array}{l} \ell = \int h_x \, dx \\ m = \int h_y \, dy \end{array} \right\}$$ (15)

where (x,y) are the curvilinear coordinates and (hx,hy) are the me-
trics of the transformation. The coordinates ℓ and m correspond
to the actual cascade coordinates. The vectors of Figure 13 are
tangent to the pressure surface, suction surface, and splitter
vane.

On the blade-to-blade surface 11.9% of the distance between
the hub and symmetry plane of the system (Figure 14) boundary
layers are clearly indicated on both the pressure and suction blade
surfaces. Furthermore, a bow shock has formed about the splitter
vane. This shock is caused by the assumption of no splitter vane

32

loading in the initial inviscid field. It is as if the splitter

vane were instantaneously inserted in the flow field to produce a

piston-like bow shock. This phenomenon is a transient condition

which diffuses as the blade-to-blade surface moves towards the

symmetry plane.

In Figure 15 a velocity vector plot is shown on a blade-to-

blade surface 13.8% of the distance between the hub and symmetry

plane. This bow shock surrounding the splitter vane leading edge

is weaker, and a separation can be seen on the leading edge of the

suction blade surface.

Figure 16 shows a velocity vector plot of the cascade flow

field on a blade-to-blade surface 62% of the distance between the

hub and the symmetry plane. The initial bow shock has disappeared

on the splitter vane. A large vortex is clearly seen on the suction

surface of the cascade blade near its leading edge. This vortex,

which is a result of the interaction between the pressure surface

leading edge shock wave and the suction surface boundary layer, re-

duces the flow area to produce a rapid turning of the flow as it

streams about the vortex. Separated regions are also indicated at

the trailing edge of the cascade suction surface, along the pressure

side of the splitter vane, and at the trailing edge of the splitter

vane suction surface.

The cascade velocity field at the symmetry plane is shown in

Figure 17. The vortex near the leading edge of the cascade blade

suction surface, and the separated region near the trailing edge of

the suction surface of the splitter vane are still present. However,

a comparison of Figures 17 and 18 shows that the flow almost uni-

formly accelerates as the symmetry plane is approached.

5.5.2 Flow about the Splitter Vane

Development of the flow field about the splitter vane is presented in Figures 18 to 23. At 5.3% of the distance between the hub and symmetry plane (Figure 18) a bow shock is indicated about the splitter. The weakening and eventual diffusion of this bow shock is indicated in Figures 19 and 20. Figure 20 presents the field on the 28% blade-to-blade surface. A small separation region is indicated on the pressure side of the splitter, while the flow remains attached on the suction side of the splitter vane.

The main points emerging from Figures 18 to 20 are that a transient bow shock forms almost immediately about the splitter vane and then diffuses away.

Figure 21 shows a velocity vector plot of the splitter vane flow field on a blade-to-blade surface 50% of the distance between the hub and the symmetry plane. On the pressure side of the splitter vane the vortex present on the 28% blade-to-blade surface has grown, while a new separated region has developed at the trailing edge of the suction surface of this vane.

The vortex on the pressure surface of the splitter vane has further increased in size when the blade-to-blade surface has moved 80% of the distance between the hub and symmetry plane (Figure 22). Furthermore, this figure also depicts separation along a large portion of the splitter vane suction surface, a recirculation region at the trailing edge of the suction surface of the cascade blade, and a separation near the trailing edge of the pressure surface of the cascade blade.

34

The velocity field in the vicinity of the cascade exit is shown in Figure 23 at the symmetry plane. Comparison of the fields of Figures 22 and 23 indicates that an acceleration takes place as the blade-to-blade surface approaches the symmetry plane. The symmetry plane flow in the vicinity of the splitter vane suction surface, downstream of the 40% chord station, is separated with reattachment taking place near the trailing edge.

5.5.3 The Inviscid Field and Flow in the Symmetry Plane

The inviscid flow field for the blade-to-blade surface is generated from the pressure distribution on the mean stream surface[1,2]. It is based on the assumption that static pressure varies linearly from the mean stream surface to the pressure and suction surfaces of the cascade blade. Thus, the velocity distribution from blade-to-blade can be obtained from the isentropic relations. The inviscid field is then used in the zeroth iterate for the blade-to-blade computation in the VANS code. Hence, the inviscid solution, generated in the manner just described, plays an important role in the first iterate. Its influence on the accuracy of our solution will be diminished as the number of iterations increases, especially when the cross-flow computation becomes part of the iteration algorithm.

The inviscid flow field yields certain mass fluxes at specific stations along the cascade passage. As the surface of integration approaches the symmetry plane, the mass flux at each station should reach the maximum possible value. In fact, the mass flux at all stations along the cascade would reach the same value <u>right at</u>

35

the symmetry plane where all vertical velocities vanish. The pre-
sent inviscid solution, which is expected to be valid throughout a
good portion of the channel from hub to the symmetry plane, would
be relatively poor in describing the flow field near or at the
symmetry plane because the continuity equation is not exactly sa-
tisfied at either the hub or symmetry plane. For example, at the
axial station along the hub of zero, (see Figure 24), the mass
flux there is as high as 130% of the incoming mass flux, which
means that a strong vertical flow velocity is needed at that sta-
tion in order to satisfy the continuity equation. The corresponding
mass flux variation based on the viscous solution, and dependent
on the inviscid mass fluxes, is also shown in Figure 24.

Because of the preceding observation and the requirement on
maximum mass flow at the symmetry plane, the gas is then allowed
to expand isentropically from a place close to the symmetry plane
(78% blade-to-blade surface) to the symmetry plane (100% blade-
to-blade surface). This stipulates that all viscous losses at the
78% blade-to-blade surface are constant in the remainder of the
channel. This stipulation was verified by monitoring the losses
at every cycle of our computation between the 78% and 80% blade-
to-blade surfaces. Based on our monitoring we are satisfied that
all viscous losses have become nearly stationary above the 78% sur-
face. The isentropic expansion yields sonic conditions for a good
portion of the suction surface. The pressure distribution on the
suction surface is however not uniform at the symmetry plane, because
the viscous losses at each station are quite different from one ano-
ther. This simple algorithm for obtaining solutions at the

symmetry plane, based on the solution on the 78% surface, is applied
to all points at the symmetry plane.

According to the isentropic relation of Reference 31, we find

$$\frac{\dot{m}(\text{symmetry plane})}{\dot{m}(78\% - \text{surface})} = \frac{\left\{ \left[1 - \left(\frac{P}{P_+}\right)^{\frac{\gamma-1}{\gamma}} \right]^{\frac{1}{2}} \left(\frac{P}{P_+}\right)^{\frac{1}{\gamma}} \right\}_{\text{symmetry plane}}}{\left\{ \left[1 - \left(\frac{P}{P_+}\right)^{\frac{\gamma-1}{\gamma}} \right]^{\frac{1}{2}} \left(\frac{P}{P_+}\right)^{\frac{1}{\gamma}} \right\}_{78\% - \text{surface}}} \quad (16)$$

where $\dot{m}$ (symmetry plane) is the maximum possible mass flux up to
the sonic speed, $\dot{m}$ (78%-surface) is the mass flux evaluated at a
corresponding station on the 78% surface, and

$$P_{+\text{symmetry plane}} = P_{+78\% \text{surface}} \quad (17)$$

Equations (16) and (17) are employed to compute the local static to
stagnation pressure ratio. Based on the isentropic Mach number-pres-
sure ratio relation

$$M = \sqrt{\left(\frac{2}{\gamma-1}\right) \left[\left(\frac{P_+}{P}\right)^{\frac{\gamma-1}{\gamma}} - 1 \right]} \quad (18)$$

the Mach number is computed for $P/P_+ > .5283$. In cases where
$P/P_+ < .5283$, sonic flow is assumed. The usual isentropic relations
are employed to compute the local density, local specific internal
energy, and local velocity at the symmetry plane.

In summary, the principal results of the blade-to-blade iterate
were two-fold. First, a large separated region was computed on the
suction blade surface; caused by the interaction of the shock wave

37

emanating from the pressure surface leading edge and the boundary layer flowing along the suction blade surface. Second, the cascade suction surface separated region distorted the flow incident to the splitter vane producing a fairly significant separated region on its pressure surface. The blade-to-blade solution is an intermediate iterate in the iteration process. The cross-sectional iteration, which is discussed in Section 6, provides a good engineering answer to this problem.

SECTION VI

DEVELOPMENT OF CROSS-SECTIONAL SOLUTION:
THE SECOND ITERATE

6.1 Mapping of Cross-Sectional Surface from Cartesian to Curvilinear
Space

In Section 5.2 a blade-to-blade surface, specified in cylindri-
cal coordinates r, θ, X_3, was mapped to x, y, z space. This sec-
tion is concerned with the mapping of a cross-sectional surface from
cartesian to curvilinear coordinates.

A meridional view of traces of the blade-to-blade and cross-
sectional surfaces is presented in Figure 9. The streamline-like
lines of Figure 9 represent traces of blade-to-blade surfaces,
while the potential like lines represent traces of cross-sectional
surfaces. The surfaces x = constant are selected as meridional planes.
The surfaces y = constant are obtained by rotating the streamline-
like-lines about the axis of the system. Surfaces z = constant are
obtained by rotating the potential-like-lines about the axis of the
system.

Streamline-like-meridional curves are labelled with the para-
meter y and are calculated according to the following integral

$$y = \frac{2}{r_0^2} \int_0^m r \left(\cos \lambda - \sin \lambda \right) dm' \qquad (19)$$

where r is the local radius, r_0 is the hub radius at the cascade blade
trailing edge, and m is the arc length along the upstream potential-
like-line of Figure 9, λ is the angle that the streamline-like-
lines of the system make with the potential-like-lines, and m' is
a dummy variable.

39

Potential-like-meridional curves are labelled by the parameter z, which is a measure of distance along the hub. The following integral is used to define the z curvilinear coordinate

$$z = \frac{1}{r_0} \int^{n_h} dn_h' \tag{20}$$

where n_h is the arc length along the hub and n_h' is a dummy variable. As in the case of Equation (19), z is nondimensional.

Let us consider a cross-sectional surface between the leading edge of the cascade blade and the leading edge of the splitter vane, i.e., surface labelled z_3 in Figure 9. This surface is schematically illustrated in cartesian coordinates (X_1, X_2) in Figure 25a. As in the case of the blade-to-blade solution a radius of 10000 inches has been added to the ordinates of the cascade coordinates. The transformed geometry to (x,y) space is shown in Figure 25b. As seen from Figure 25b the cross-sectional surface has been transformed to a nearly rectangular region in (x,y) space; blade thickness produces some deviation from the rectangular geometry. The calculation takes place in (x,y) cross-sectional planes which move from the upstream boundary of the system to the cascade exit as the z parameter increases from zero at the upstream boundary to .61303-03 at the cascade exit.

6.2 Interpolation of Blade-to-Blade Solution onto Cross-Sectional Surfaces

A computer code has been written and debugged to interpolate the blade-to-blade data onto cross-sectional surfaces. The inter-

40

polated cross-sectional data will serve as the previous iterate in obtaining the cascade cross-sectional solution. The variables interpolated include axial coordinate, density, specific internal energy, eddy viscosity, and the three velocity components.

The blade-to-blade solution was obtained on a finite difference mesh comprised of 80 points in the axial direction and 42 points in the azimuthal direction. For purposes of interpolation, 19 blade-to-blade surfaces were employed, starting from the blade-to-blade surface coresponding to the hub and ending at the blade-to-blade surface corresponding to the symmetry plane. Each blade-to-blade surface is comprised of 80 streamwise points; hence, there are eighty cross-sectional surfaces. Furthermore, since there are 42 azimuthal points, each cross-sectional surface will be comprised of 19 points in the radial direction and 42 azimuthal points. Therefore, the finite difference mesh upon which the blade-to-blade solution is specified is comprised of 63840 points.

6.3 Meshes, Boundary Conditions, and Initial Conditions

6.3.1 Finite Difference Meshes

As seen from Figure 25b, the transformed cross-sectional surface is nearly rectangular, with the hub and symmetry plane lines parallel to each other. Due to the nearly rectangular transformed cross-sectional geometry, specification of the mesh points in (x,y) space becomes a trivial problem. The mesh is comprised of the intersection of 30 lines parallel to the hub and 42 lines conforming to the shape of the main cascade blade and splitter vane. The 42 azimuthal lines are spaced finely in the vicinity of the main

41

cascade blade and splitter vane, and coarsely in the center of the blade passage.

6.3.2 Boundary Conditions for Cross-Sectional Computation

The boundary conditions for the supersonic compressor cascade in cross-sectional computation planes are as follows:

1) No slip flow is enforced along the hub (contoured wall), pressure surface, suction surface, and splitter vane between the cascade blade entrance and discharge.

2) Periodic flow is enforced downstream of the discharge of the blades except on the hub and symmetry plane surfaces. On the hub the velocities will be set to zero, and frictionless flow calculated on the symmetry plane.

3) Periodic flow is enforced upstream of the cascade blade leading edge except on the hub where the velocities from the previous iterate are prescribed, and on the symmetry plane where frictionless flow with zero normal velocity is prescribed.

The above boundary conditions are illustrated in Figure 26. Figure 26a shows the cross-section in (x,y) curvilinear space upstream of the leading edge of the cascade blades. Periodic flow is enforced on the lateral boundaries, velocities from the previous iterate are enforced on the hub and frictionless flow, with zero normal velocity, is envoked at the symmetry plane. Figure 26b shows the (x,y) plane within the blading passage. No slip is imposed on the hub, splitter vane and cascade blades. Frictionless flow with a zero normal velocity is envoked at the symmetry plane. Downstream of the cascade discharge (Figure 26c), periodic flow is imposed on the lateral boundaries, no slip flow is enforced on the hub and

42

the normal velocity is set to zero at the symmetry plane, with the other components U_x and U_z determined from frictionless flow equations.

6.3.3 Initial Conditions for Cross-Sectional Computation

The blade-to-blade solution interpolated onto the farthest upstream cross-sectional surface of the system (see Figure 9), serves as the initial conditions for the cross-sectional calculation.

6.4 Characteristic Time for Calculation

The speed U_z at which the (x,y) cross-sectional plane moves from the farthest station upstream of the cascade to the cascade exit must be specified. For the cross-sectional calculation a speed parameter U_z of the 772 fps was employed.

As is discussed in Section 5.4, the characteristic time for diffusion is .2022 ms based on a distance of .1642 ft. between the suction surface leading edge and trailing edge at the hub. Therefore, at U_z = 772 fps, 1.05 characteristic times will pass after the cross-section moves from the entrance to the exit of the cascade.

6.5 Numerical Results of Cross-Sectional Solution

The cascade problem was run through 2216 cycles; where each cycle of computation corresponds to updating all the variables of motion on one cross-sectional surface. In 2216 cycles the cross-sectional surface was moved from the farthest upstream cross-section at X_3 = -3.00 ft (see Figure 9) to the exit of the cascade. The z-coordinate at X_3 = -3.00 ft is zero, while the z-coordinate at the discharge is .613149-03 radians. The cascade cross-sectional

43

iterate required 53 minutes on the Air Force Weapons Laboratory CDC 7600 Computer.

The results obtained are presented in the following format:

1. Data reduction analysis and procedures.

2. General flow field structure.

3. Comparison of numerical and experimental results.

4. Cascade Mach number.

5. Cascade total pressure losses.

6.5.1 Data Reduction Analysis and Procedures

This section is concerned with those cross-sectional surfaces for which numerical data have been reduced and the method of data reduction.

Cross-sectional surfaces for which numerical data have been reduced and interpreted are presented in Figure 27. This figure shows a meridional view of the cascade contoured wall and symmetry plane with cross-sectional surface traces indicated. These cross-sectional surfaces are labelled with the axial position that they intercept the symmetry plane of the system in the following manner. The ratio of axial distance from the cascade leading edge to the total axial length of the cascade blade*, ℓ_r, is employed to position a given cross-sectional surface. These ratios are indicated within parentheses in Figure 27. The cascade blade leading edge, splitter vane leading edge and cascade blade exit are also presented in Figure 27. It is noted that the farthest downstream cross-section is

*The total axial length of the cascade blade is 1.8396 inches.

44

labelled by the ratio (.945) and intercepts the hub of the system at the cascade exit*.

In order to properly interpret these numerical data, the cross-sectional surfaces of computation were tipped to the mean camber line of the cascade blade. Figure 28 presents a blade-to-blade view of the traces of the computational cross-section and the tipped cross-section. The computational cross-sectional trace is normal to the axial direction, X_3, while the tipped cross-section is normal to the blades. The tipping procedure, which was invoked for the cross-sections of Figure 27 between the leading and trailing edges of the cascade blade, is described in the following paragraph.

Let (x,y,z) and (U_x, U_y, U_z) define the curvilinear coordinates and velocity components, respectively, of the computational cross-sectional plane. The computational cross-sectional plane was mapped to the curvilinear coordinates x', y', z' which corresponded to the tipped plane. The original velocity components U_x and U_z were re-defined, respectively, as U_x' and U_z', to exist within and normal to the tipped plane. The nearly radial component of velocity U_y was unchanged in the transformation. This method of tipping the planes and associated revision of the velocity components is approximate, since no interpolation between computational cross-sectional planes was attempted. However, although approximate, it is believed that the tipped data present a more realistic physical picture of the fluid mechanics of the compressor cascade. Therefore, all the data presented in the forthcoming sections are on tipped cross-sectional planes.

*Due to a lack of time and funds it was not possible to carry the cross-sectional calculation into the wake of the system.

45

6.5.2 General Flow Field Structure

The general flow field structure is best depicted in contour plots of the ratio of the streamwise component of velocity U_z' to the local sound speed a on tipped cross-sectional planes. Contour plots of this type comprise the bulk of material presented in this section. For completeness, a few velocity vector plots of the tipped cross-sectional flow field, i.e., U_x', U_y, are also included.

A contour plot of U_z'/a is presented in Figure 29 on a tipped cross-sectional surface of ratio ℓ_r = .206 (see Figure 27). The plot is shown in the coordinates ℓ and m defined by Equations 15. The coordinates ℓ and m correspond to the actual cascade cross-sectional coordinates. The hub, symmetry plane, pressure surface and suction surface are indicated in the figure; the cross-section of Figure 28 becomes non-rectangular due to the tipping of the computational cross-sectional plane and the thickness of the blades. Upstream of the blading the velocity ratio U_z'/a = 1.46, while in the tipped cross-section at ℓ_r = .206 velocity ratios less than one appear. Therefore, the shock wave pattern at the cascade entrance is sufficient to produce subsonic conditions. Boundary layers are clearly indicated on the hub and pressure surface of the main cascade blade. Furthermore, a significant separation is indicated on the suction surface of the main cascade blade.

A contour level of U_z'/a = -.20 exists in the vicinity of the cascade suction blade surface. The negative velocity indicates the presence of a separated region. The separated region starts

46

at an ordinate m of about .04 and takes up about a third of the cross-section. The shock wave emanating from the leading edge of the pressure surface of the main cascade blade interacts with the turbulent boundary layer flowing along the suction blade surface to produce the separation. This separated region reduces the effective flow area of the cross-sectional surface; thus, markedly disturbing the flow pattern there.

A contour plot of U_z'/a is shown in Figure 30 on a tipped cross-sectional surface of axial distance ratio ℓ_r = .385 (see Figure 27). Boundary layers are still in evidence on the hub and pressure surface of the main cascade blade. Furthermore, the suction blade surface separated region is much smaller than that of Figure 29. The separated region starts at an ordinate m of .06 and takes up about a fifth of the cross-section. This region is again defined by the contour line $U_z'/a = -.20$. Due to the smaller separated region the cross-sectional area is larger at ℓ_r = .385 than at ℓ_r = .216; thus, the subsonic flow is diffused, as indicated by the velocity ratios of Figures 29 and 30.

The suction surface separated region shown in Figures 29 and 30 is in accord with the suction surface separated region of Figures 16 and 17, computed during the blade-to-blade iteration. Thus, two successive iterations produced nearly the same separated flow. The computation of the same physical phenomena in two successive iterations is an indication of the convergence of the numerical method. Furthermore, this points out one of the principal advantages of the ADE numerical technique. Through alternating the

47

direction of marching, a vortex was computed in cross-sectional planes which did not contain the vortex.

Contour plots of the streamwise velocity component are presented on cross-sections aft of the splitter vane leading edge in Figures 31, 32, and 33. Figure 31 shows contours of the velocity ratio U_z'/a on a cross-section of axial distance ratio $\ell_r = .605$. The splitter vane pressure surface and suction surface are indicated in the figure as well as the main cascade blade specifications. The main suction surface separated region is very small at $\ell_r = .605$, i.e., it starts at $m = .075$ and takes up about 10 percent of the channel width. The suction surface flow attached in Figures 32 and 33 at axial distance ratios $\ell_r = .672$ and $\ell_r = .945$, respectively.

The principal fluid mechanical features depicted in Figures 31, 32, and 33 are three-fold:

1. The splitter vane initially accelerates the incoming cascade flow.

2. The flow separates from the pressure side of the splitter vane.

3. The flow in the passage between the splitter vane pressure surface and main cascade blade suction surface is re-accelerated through a sonic condition and then shocked down to a subsonic condition. These three fluid mechanical phenomena are discussed further in the next several paragraphs.

Acceleration of the flow in the cascade passage, due to the splitter vane, is seen in a comparison of the streamwise velocity

ratios of Figures 30 and 31. In Figure 30, upstream of the splitter vane, streamwise velocity ratios U_z'/a of the order of .40 to .50 are present in the cross-section $\ell_r = .385$. Figure 31 ($\ell_r = .605$) shows U_z'/a going to .70 in the passage between the pressure surface of the main cascade blade and the suction surface of the splitter. Furthermore, U_z'/a approaches one in the passage between the pressure surface of the splitter vane and suction surface of the main cascade blade. The splitter vane reduces the cascade flow area; hence, an acceleration of the incoming subsonic flow is physically reasonable.

Flow separation is indicated on the pressure side of the splitter vane in Figures 31 and 32 at axial distance ratios $\ell_r = .605$ and $\ell_r = .692$, respectively. This separated region is more pronounced in the cross-section at $\ell_r = .692$ than in the cross-section at $\ell_r = .605$. Near the exit of the cascade, i.e., at the cross-section associated with axial distance ratio $\ell_r = .945$ (Figure 33), the splitter vane pressure surface flow is again re-attached. The pressure surface splitter vane separation is caused by the main cascade suction surface separation discussed earlier. The shock-wave turbulent boundary layer interaction, which triggers the main cascade blade suction surface separation, produces a variable incidence angle distribution of the flow upstream of the splitter vane. It is believed that this incidence angle distribution upstream of the splitter vane produces the splitter vane pressure surface separation.

Figure 34 shows a Schlieren picture of a two-dimensional shock-wave turbulent boundary layer interaction[32]. The freestream Mach

49

number for this case is 1.45 and the ramp angle is 4.5 degrees.

The separated region alters the direction of the shear layer flow

near the wall, increases the thickness of the shear layer and changes

the angle of the reflected shock wave. Hence, the variable direc-

tion of the flow downstream of the interaction region is markedly

different than what would occur if there were no shock-wave bound-

ary layer interaction . In fact the shear layer flow is directed

toward the surface of the system.

To illustrate the variations in splitter vane incidence

angle of the fluid, the mass flux division between the flow passage com-

prised of the main cascade pressure surface and splitter vane suction

surface (Passage I) and the flow passage comprised of the splitter

vane pressure surface and main cascade blade suction surface (Pas-

sage II) was determined. It was found that 53 percent of the in-

coming airflow passed through Passage I, while 47 percent passed

through Passage II. The nearly equal division of mass flux is

somewhat surprising at first. One would expect most of the mass

to go into Passage I, due to the large separated region on the

main cascade blade suction surface. However, the separation region,

which is caused by a shock-wave boundary layer interaction,

sufficiently changed the flow angles to induce a greater portion of

the mass flux into Passage II.

The splitter vane pressure surface separation computed in the

cross-sectional mode of iteration is in accord with the separated

region computed earlier in the blade-to-blade iteration. A comparison

50

of cross-sectional iterate Figures 31 and 32 with blade-to blade iterate Figures 21 and 22 indicates the presence of a splitter vane pressure surface separation at about the same region along the splitter. Thus, as in the case of the main cascade blade suction surface separation, two successive iterations produced nearly the same separated flow. Computation of the same physical phenomena in two successive iterations is an indication of the convergence of the method.

Due to the separation on the splitter vane pressure surface, the flow in Passage II undergoes an acceleration from subsonic to supersonic conditions and then subsequently goes through a normal shock back to subsonic cascade exit conditions. The acceleration to supersonic flow is indicated in Figures 31 and 32 at axial distance ratios of $\ell_r = .605$ and $\ell_r = .692$, respectively. In fact in the cross-section at $\ell_r = .692$ the velocity ratio U_z'/a approaches 1.3. Figure 33 ($\ell_r = .945$), which corresponds to a cross-section near the cascade exit, shows subsonic streamwise flow. In summary, the splitter vane pressure surface separation produces an effective area variation in Passage II which acts as a convergent-divergent nozzle to the flow.

For completeness cross-sectional velocity vector plots, i.e., of components U_y, U_x', are shown in Figures 35 to 37. Figure 35 shows the cross-sectional velocity field on an untipped cross-sectional plane located upstream of the cascade, i.e., $\ell_r = -1.146$ (see Figure 27). It is seen from Figure 35 that the cross-sectional field is effectively undisturbed upstream of the

51

cascade. The cross-sectional velocity field is shown on a tipped cross-sectional plane just upstream of the splitter vane in Figure 36. The cascade suction surface separation and the disturbances caused by the shocks in the system produce a complicated eddy pattern in the cross-section. However, it should be pointed out that the vectors of Figure 36 are small in magnitude relative to the streamwise component of velocity. The eddy field near the exit of the cascade is shown in Figure 37 at an axial distance ratio $\ell_r =$ .945. A comparison of cross-sectional velocity fields between Figures 36 and 37 indicates that the splitter vane tends to reduce the secondary flows in the system.

6.4.3 Comparison of Numerical and Experimental Results

Holtman, McClure, and Sinnet[29] measured static pressures along the main cascade blade at ten stations, along the suction surface of the splitter vane at three stations and along the pressure surface of the splitter vane at two stations. The above measurements were confined to the symmetry plane of the cascade. In addition, mass averaged values of pressure, total pressure, and Mach number were measured in the wake of the cascade at the symmetry plane. It is the purpose of this section to compare these measurements with corresponding calculations.

Figure 38 presents a comparison of calculated and experimental static pressures along the main cascade blade at the symmetry plane. The abscissa of the figure is the percent chord along the main blade and the ordinate is the ratio of the local static pressure to the freestream stagnation pressure. Comparisons of cascade blade suction and pressure surface static pressures are good.

52

Comparisons of numerical and experimental static pressures for the cascade splitter vane are shown in Figure 39. Coordinates of the figure are the same as that of Figure 38. These comparisons are at the symmetry plane of the system. As can be seen from Figure 39, the calculated pressures along the splitter suction surface are in excellent agreement with corresponding data. Calculated pressure ratios along the pressure surface of the splitter start at a ratio $p/p_{t\infty}$ of about .80, decrease to a ratio of approximately .45, and then increase to a ratio above .60. The initial drop in pressure ratio is due to separation on the splitter pressure surface. The subsequent increase in pressure ratio results after re-attachment has taken place. It appears from Figure 39 that the calculated initial pressure drop is overestimated; thus, the extent of the separated region may be overestimated. It is believed that the zeroth iterate, which assumed no splitter vane loading, is the cause of the larger calculated pressure drop. After re-attachment the numerical and experimental pressures are in accord on the splitter pressure surface.

Mass-averaged quantities were measured at the symmetry plane at an axial station of about 16 percent of a chord aft of the discharge of the cascade. Calculated mass-averaged quantities were determined at the symmetry plane on a cross-section at axial distance ratio $\ell_r = .945$, i.e., just upstream of the cascade exit. Thus, we have computed results effectively at the cascade exit and measured results in the wake of the cascade.

The symmetry plane of the cascade is quite unique, since no mass flow occurs normal to it. Thus, the mass flux within the

symmetry plane at the cascade exit is precisely the mass flux within the symmetry plane 16 percent of a chord aft of the cascade exit. Based on the area ratio between the cascade exit and station of measurement (A_w/A_e), the calculated mass averaged Mach number at the cascade exit ($\bar{M}_e$) and the pressure recovery between the cascade exit and station of measurement ($\bar{P}_{tw}/\bar{P}_{te}$), the mass averaged Mach number ($\bar{M}_w$) can be calculated at the station of measurement. The calculated mass averaged Mach number at the cascade exit $\bar{M}_e$ is .920, the area ratio A_w/A_e is 1.05757 and the calculated mass averaged exit pressure recovery $\bar{P}_{te}/P_{t\infty}$ is .896. The measured pressure recovery in the wake of the cascade is $\bar{P}_{tw}/P_{t\infty}$ = .860; hence, the pressure recovery between the cascade exit and measurement station $\bar{P}_{tw}/\bar{P}_{te}$ is .9598. On the basis of the above, the pressure ratio and Mach number at the station of measurement are computed. The calculations are compared to corresponding measured quantities in Table II.

Table 2

COMPARISON OF MASS AVERAGED STATIC PRESSURE AND

MACH NUMBER IN THE WAKE OF THE CASCADE AT THE SYM-

METRY PLANE

Parameter	Calculated	Measured
Pressure Ratio ($\bar{P}_w/P_\infty$)	1.893	1.883
Mach Number ($\bar{M}_w$)	.832	.837

The calculated wake Mach number and pressure ratio are within half a percent of the corresponding measured values.

54

On balance, numerical-experimental comparisons of the main cascade blade and splitter vane static pressures, and mass averaged quantities in the wake of the cascade are good. These comparisons strongly suggest that the numerical method has produced a good engineering prediction of the very complicated supersonic compressor cascade flow field.

In order to demonstrate convergence of the solution, a third blade-to-blade iterate must be developed, based on the cross-sectional field as the previous iterate. A calculation of this type can be used to evaluate the degree of convergence of the numerical method. Unfortunately, time and funds did not permit a third iteration.

6.5.4 Cascade Mach Number Field

In order to better understand the details of the cascade flow field, contour plots of the local Mach number were made within the blading passage. Figures 40-44 show Mach number contour plots on cross-sections having axial distance ratios ℓ_r of .206, .385, .605, .692, and .945, respectively. Meridional traces of these cross-sections are shown in Figure 27.

At an axial distance ratio ℓ_r of .206 (Figure 40), Mach numbers of about .80 prevail throughout most of the cross-section, with low subsonic Mach numbers along the main cascade blade suction surface and supersonic flow at the symmetry plane with a peak Mach number of 1.4. The Mach .80 flow in the center of the cross-section is consistent with the fluid mechanics at the leading edge of the main cascade blade pressure surface. The pressure surface leading edge wedge angle with respect to the Mach 1.46 freestream

55

flow is about 14 degress. This angle is too great to permit an attached oblique shock at the pressure surface leading edge. This being the case, a bow shock must occur just upstream of the cascade blade. On the basis of the blade-to-blade velocity vector plots of Figures 16 and 17, which show that the separated suction surface region lies on a normal from the pressure surface leading edge, the bow shock must be nearly normal to the pressure surface of the blade. The Mach number behind a normal shock is .72 for a 1.46 Mach number freestream flow; hence, an .80 local Mach number in the cross-section at an axial distance ratio l_r of .206 is consistent

The suction surface separation is also clearly indicated in Figure 40. Starting at an ordinate of m = .04 and going to the symmetry plane, Mach number contours are densely packed with a peak Mach number of .80 outside the shear layer and zero at the wall. The separated region takes up about a third of the width of the channel.

A contour plot of the local Mach number at a cross-section of axial distance ratio l_r = .385 is shown in Figure 41. The suction surface separated region has become smaller in this figure; thereby, increasing the cross-sectional area. The increased cross-sectional area has further diffused the flow in the center of the passage from about .80 Mach at l_r = .206 to .60 Mach at l_r = .385. Furthermore, flow at the symmetry plane is now predominantly subsonic.

Mach number contour plots within the splitter vane passage are presented in Figures 42 to 44 for cross-sections at axial distance ratios l_r = .605, .692, and .945. Boundary layers are clearly

56

seen building up on the hub, pressure surface of the main cascade blade and suction surface of the splitter vane in all three figures. In Passage I* the flow is subsonic in the center of the passage and along the pressure surface of the main cascade blade. However, along the suction surface of the splitter vane the flow is accelerated to supersonic conditions. The flow in Passage II accelerates to supersonic conditions in the center of the passage. Furthermore, at the symmetry plane a significant region of sonic flow prevails in both passages.

The flow in Passage I is subsonic near the main cascade blade pressure surface and in the center of the passage. Figure 42 shows a Mach number contour of level .40 near the cascade pressure surface, and contour levels of .60 to .80 in the center of the passage. In the neighborhood of the splitter vane suction surface, a contour level of 1.2 exists in Figure 42. Figures 43 and 44 indicate little change in Mach number near the cascade pressure surface and center of the passage from that of Figure 42. However, Figures 43 and 44 show a deceleration to sonic conditions near the splitter vane suction surface. An oblique shock wave may be present near the splitter vane suction surface to affect this deceleration. It is believed that this oblique shock wave is located at about the 75 percent chord position of the splitter vane. In Passage II the flow is accelerated to supersonic conditions in the center of the passage, and then decelerated to subsonic conditions. Figures 42 and 43, which depict the cross-sectional flow field upstream of the splitter vane 50 percent chord position, indicate an

---

*See Section 6.5.2 (p. 50) for definitions of Passage I and Passage II.

57

acceleration to Mach 1.4. Reasons for this acceleration in Passage II have been discussed earlier (see Section 6.5.2). Figure 44 shows that the flow in the center of Passage II is at approximately Mach .60 near the cascade exit. Thus, a normal shock occurs in Passage II near the 50 percent chord position.

In summary, the flow in Passage I accelerates to supersonic conditions along the splitter suction surface and then goes through an oblique shock located aft of the 50 percent splitter vane chord position. On the other hand, the flow in Passage II accelerates to supersonic conditions in the leading edge region of the splitter vane and goes through a normal shock near the 50 percent chord position.

6.5.5. Cascade Total Pressure Losses

To evaluate cascade losses, contour plots of the total pressure recovery, defined as the ratio of the local stagnation pressure to the freestream stagnation pressure ($P_t / P_{t\infty}$) were made on various tipped cross-sections within the blading passage. Figures 45 to 49 show total pressure recovery contour plots on cross-sections having axial distance ratios ℓ_r of .206, .385, .605, .692, and .945, respectively. Meridional traces of these cross - sections are shown in Figure 27. These contour plots depict the magnitude and location of losses in the flow field and these data are precisely what is required to improve the cascade performance. Detailed flow field data such as this is only possible through a numerical solution of the Navier-Stokes equations.

The principal cascade losses come from the following five sources.

58

1) A nearly normal shock emanating from the leading edge of the pressure surface of the main cascade blade.

2) A separation on the suction surface of the main cascade blade.

3) A separation on the pressure surface of the splitter vane.

4) A normal shock wave in the passage between the pressure surface of the splitter vane and the suction surface of the main cascade blade.

5) An oblique shock wave along the splitter vane suction surface.

High losses are present near the suction surface of the main cascade blade on the cross-section at an axial distance ratio l_r of .206 (Figure 45). Total pressure recoveries of the order of $P_t / P_{t\infty}$ = .10 are present in the suction surface separated region, while the total pressure recovery increases to nearly unity through the shear layer. Figure 45 indicates a thick shear layer near the suction surface.

Throughout the remainder of the flow field at l_r = .206, the losses are due to the nearly normal shock emanating from the leading edge of the pressure surface of the main cascade blade. Figure 45 shows a small contour level of .70 total pressure recovery; however, most of the cross-sectional flow is at .90 total pressure recovery. For reference purposes the total pressure recovery through a normal shock at 1.46 freestream Mach is $P_t / P_{t\infty}$ = .942.

A contour plot of the total pressure recovery at a cross-section of axial distance ratio l_r = .385 is shown in Figure 46.

59

High losses are still indicated along the cascade suction surface; however, the high loss region is confined closer to this surface than at l_r = .206. This is because the separated region is smaller at l_r = .385. Throughout a large portion of the remainder of the cross-section, the flow remains at a total pressure recovery near .90. This value is a result of the leading edge cascade main blade pressure surface shock wave.

Total pressure recovery contour plots within the splitter vane passage are presented in Figures 47 to 49 for cross-sections at axial distance ratios l_r = .605, .695, and .945. In general the results of Figures 47 to 49 show higher total pressure recoveries in Passage I than in Passage II. Furthermore, the total pressure recovery at the symmetry plane is higher than within the blading passage. As discussed earlier, the mass averaged total pressure recovery at the symmetry plane was .896 at an axial distance ratio l_r of .945.

Within splitter vane Passage I, the total pressure recovery ranges from .40 to .70 near the main cascade blade pressure surface and in the center of the passage. Near the splitter vane surface the pressure recovery ranges from .50 to .90 at distance ratios l_r of .605 and .692 (Figures 47 and 48). The pressure recovery then drops to approximately .50 along the splitter vane suction surface at l_r = .945 (Figure 49). This drop is caused by the oblique shock in Passage II.

Since the flow re-attached on the suction surface of the main blade, the high losses of the separated region, i.e., at l_r = .206, are no longer present. However, the suction blade separation did

60

produce losses, and more importantly, caused significant losses in other parts of the system.

The flow along the pressure surface of the splitter was induced to separate due to the main cascade suction blade separation. The splitter pressure surface separation caused high system losses throughout Passage II, i.e., total pressure recoveries as low as P_t/P_{t_∞} = .20 are present at ℓ_r = .605, .692 and .945 near the splitter pressure surface.

In addition the subsonic flow entering Passage II was accelerated to supersonic conditions and then shocked back to subsonic conditions. This was caused by the splitter vane pressure surface separation at its leading edge. Figures 47 and 48 show an inviscid core in Passage II of total pressure recovery in the 95 percent range*. At ℓ_r = .945 (Figure 49) pressure recoveries of 50 percent are now present in the region of Passage II where 95 percent prevailed previously. A normal shock wave in Passage II, believed located near the splitter vane 50 percent chord position, is the principal cause of this loss of pressure recovery.

---

*The contour interval is .10; hence, P_t/P_{t_∞} = .951 will show up as unity on the contour plot.

SECTION VII

CONCLUSIONS AND RECOMMENDATIONS

A numerical investigation has been conducted of the viscous, compressible, three-dimensional flow field in an axial supersonic compressor cascade. The main conclusion emerging from this research effort is that the ADE numerical method, embodied in the VANS computer codes, can produce a good engineering solution to this complex problem within two iterations. Numerical-experimental comparisons of cascade blade static pressures and mass-averaged quantities in the wake of the cascade, provide part of the evidence upon which the above conclusion is based.

A first-of-a-kind numerical solution has been developed of the flow field within the compressor cascade. It is recommended that these numerical data be further analyzed and interpreted in accord with the following two aims: (1) revising the geometry of the cascade to improve its performance, and (2) developing better physical models of the cascade flow to incorporate into the UD 0200 and UD 0300 codes[1,2] in order to provide a better zeroth iterate.

In addition to the above recommendation, it is further recommended that convergence of the ADE numerical method be demonstrated, the computational efficiency of the VANS codes be improved, and additional stator problems be solved. A third blade-to-blade iteration will permit an analysis of the convergence properties of the method. Through the use of spatial splitting of the explicit method presently employed[33], or through the use of implicit methods[34], it is believed that computational time can be reduced to within two

62

hours to complete two iterations. This would make the VANS computer codes practical for design of turbomachinery. Finally, the VANS computer code can be modified to calculate the periodic flow in the clearance region and stator blading of an axial compressor stage. Calculations of this type will reveal the fluid mechanics necessary to improve stator designs.

Figure 1. Schematic of the lower half of one blading passage
of a cascade of blades; the symmetry plane divides
the actual blading passage in half.
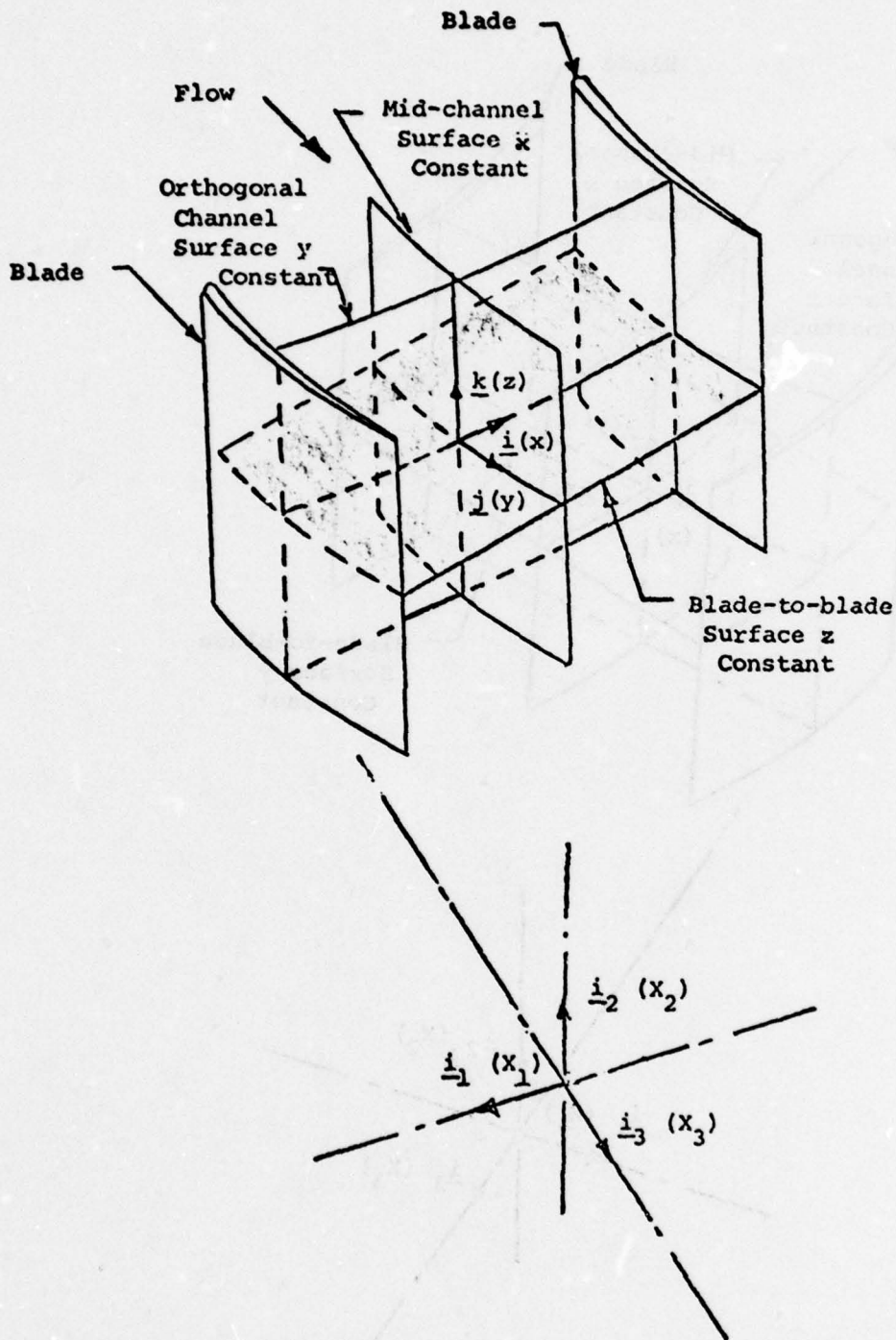
Figure 2. Schematic of cascade blading passage illustrating
the blade-to-blade mode of marching.

65
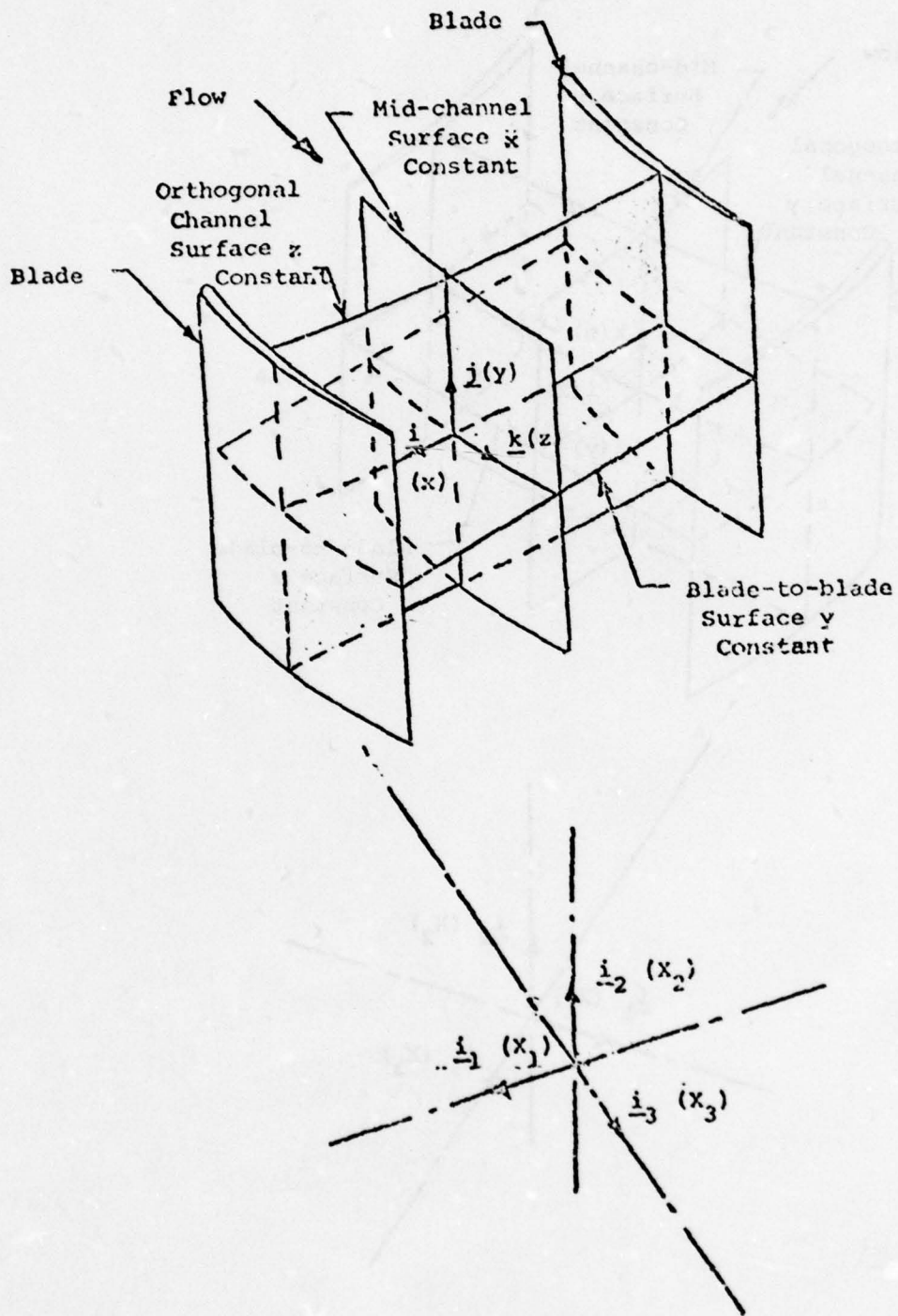
Figure 3. Schematic of cascade blading passage illustrating cross-sectional mode of marching.
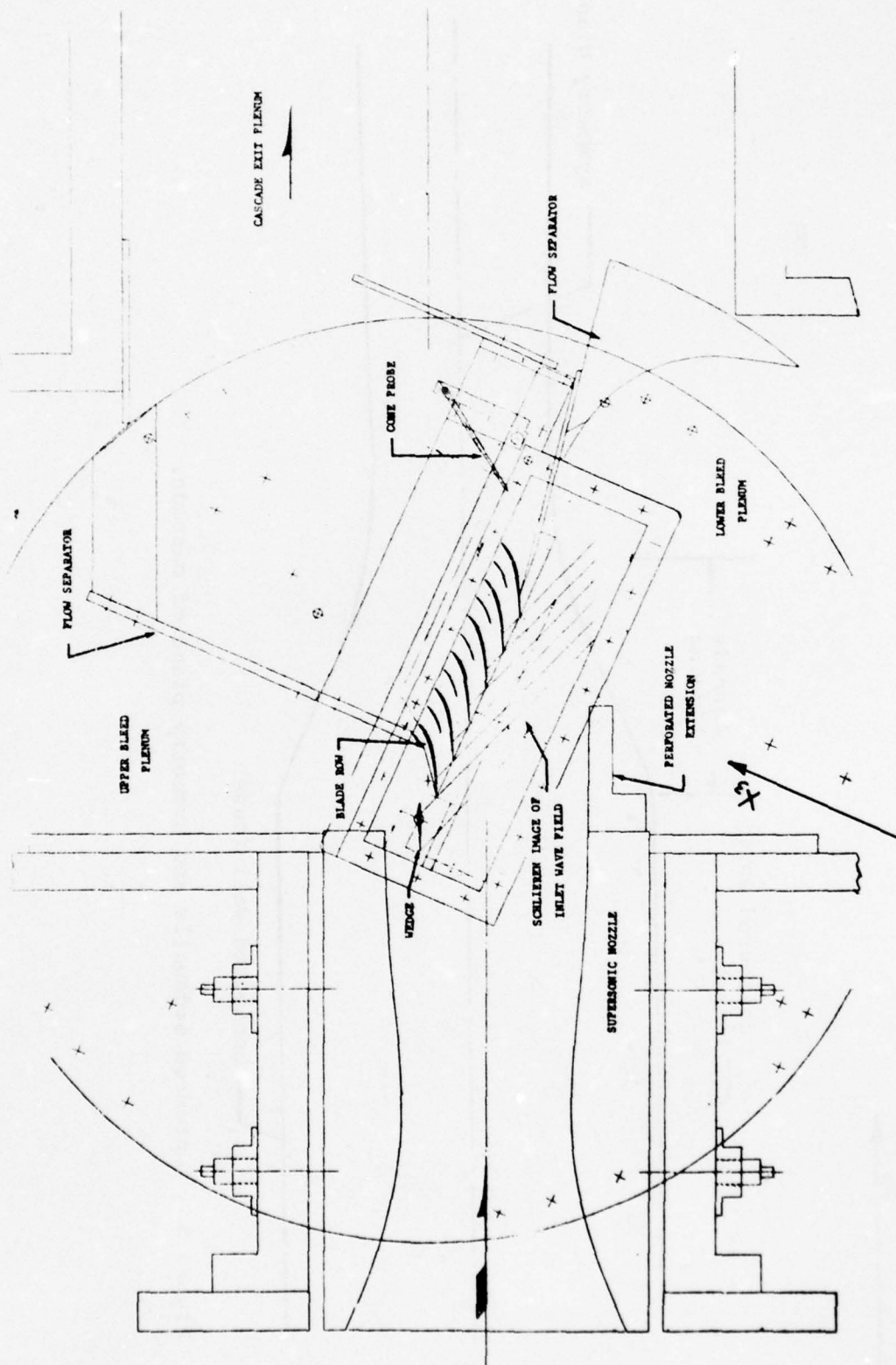
Figure 4. Compressor Cascade Schematic

67
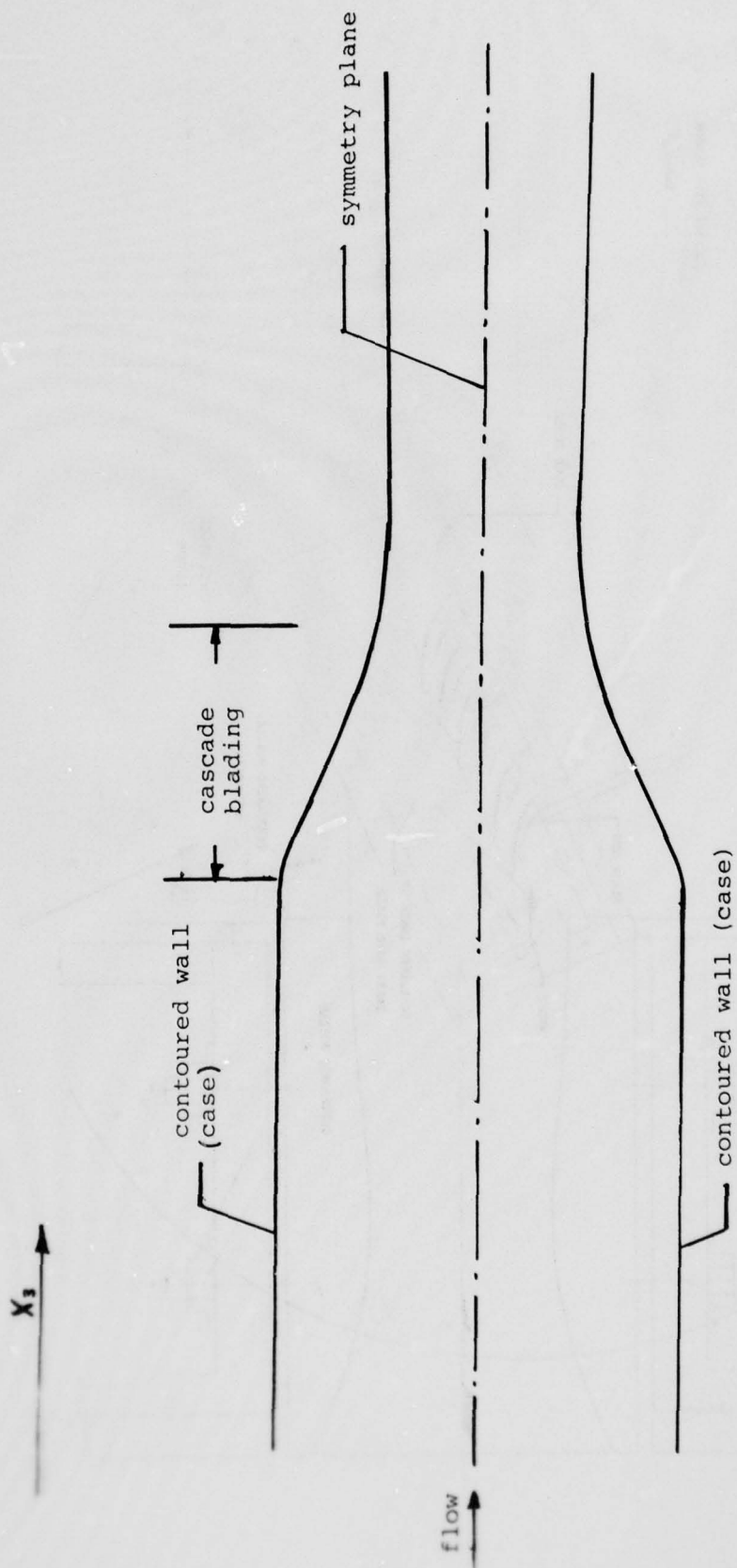
Figure 5. Contoured sidewalls and symmetry plane of cascade.
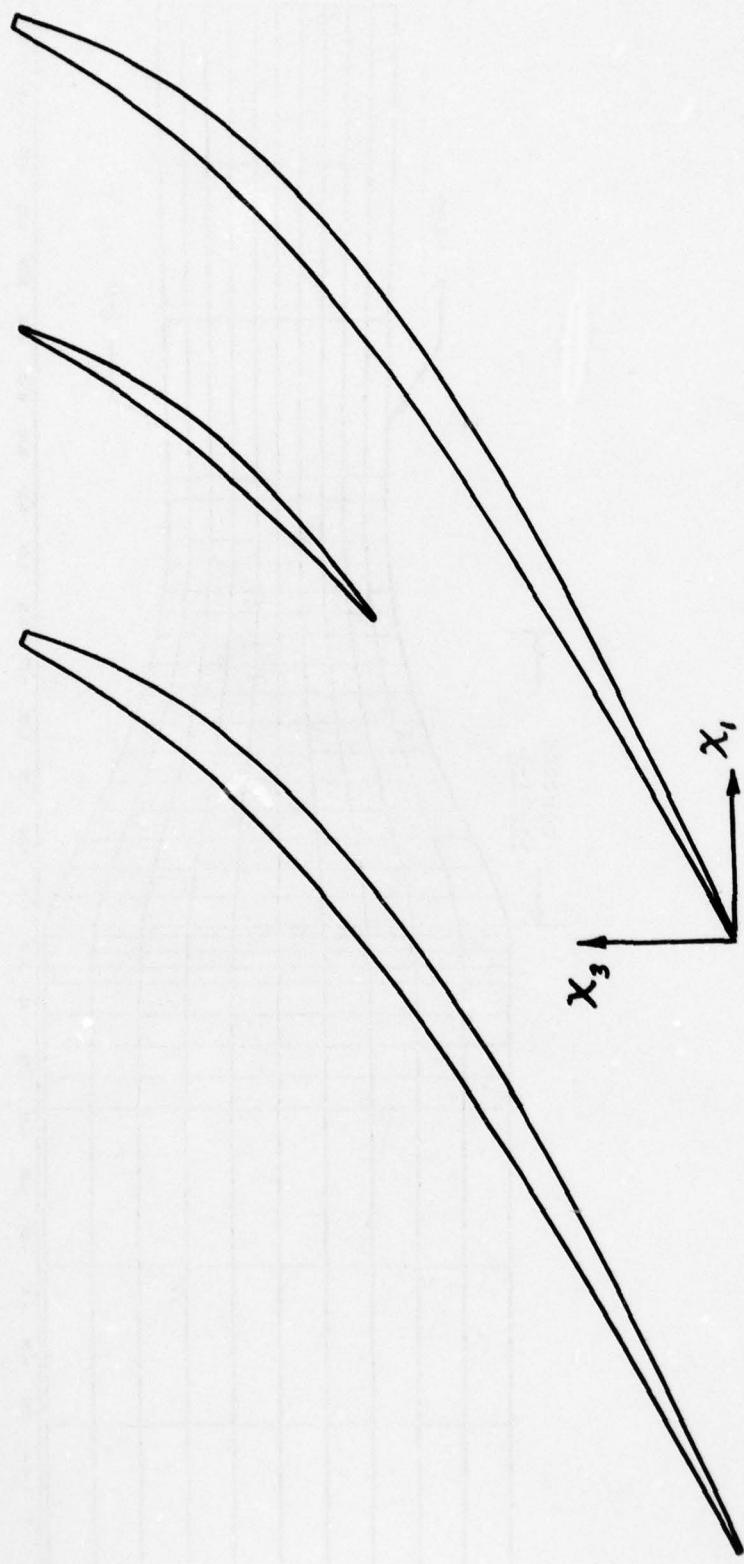
Figure 6. Blade-to-blade configuration.
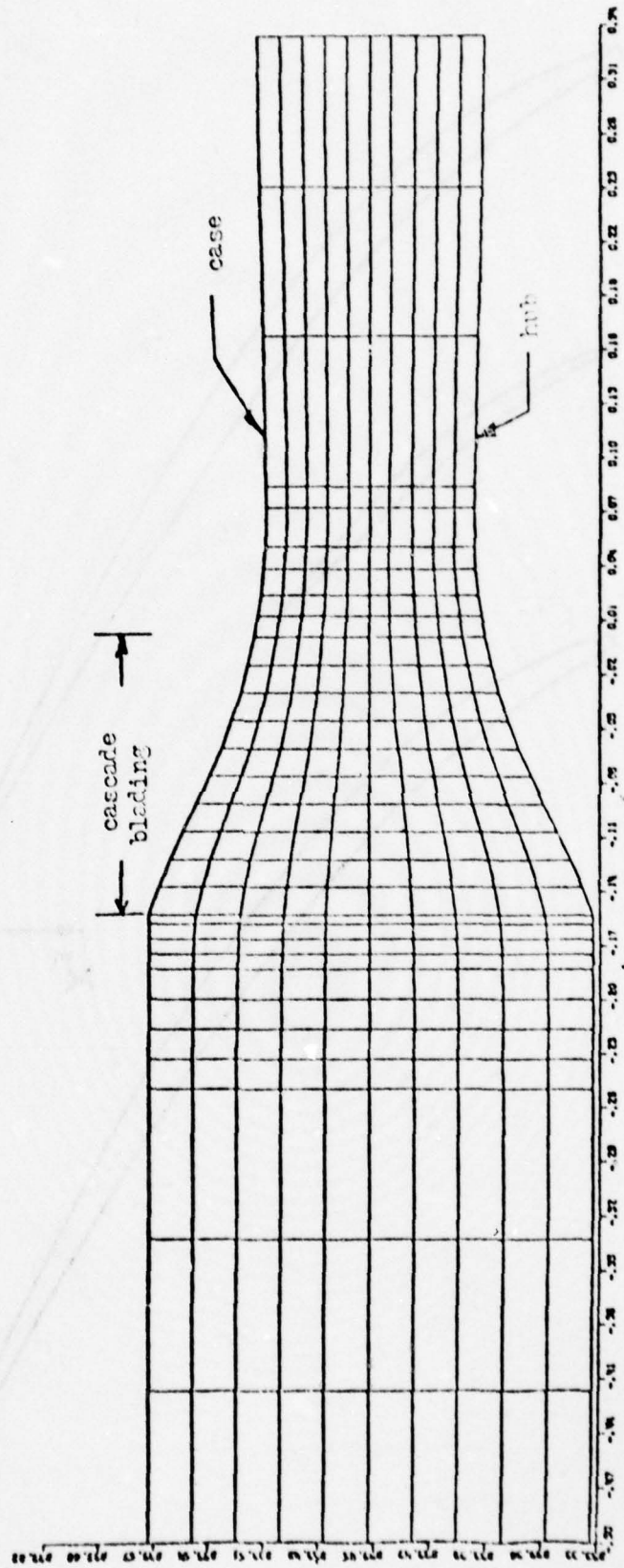
Figure 7. Meridional Projection of Enclosed Streamlines in Supersonic Compressor Cascade.

70
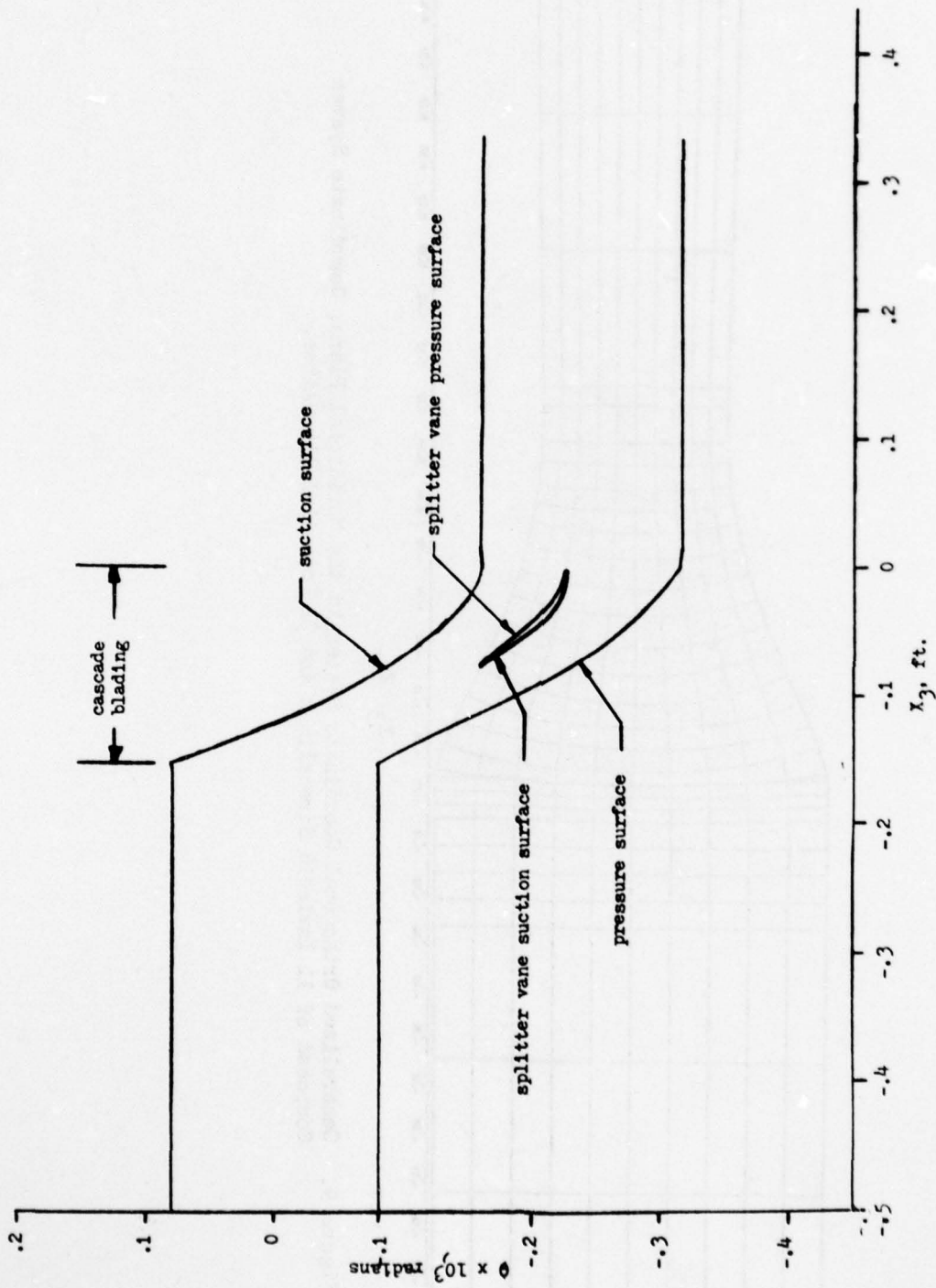
Figure 8. Angular and Axial Coordinates of the Traces of the Blading Surface on the Hub.

71

X_3, ft.
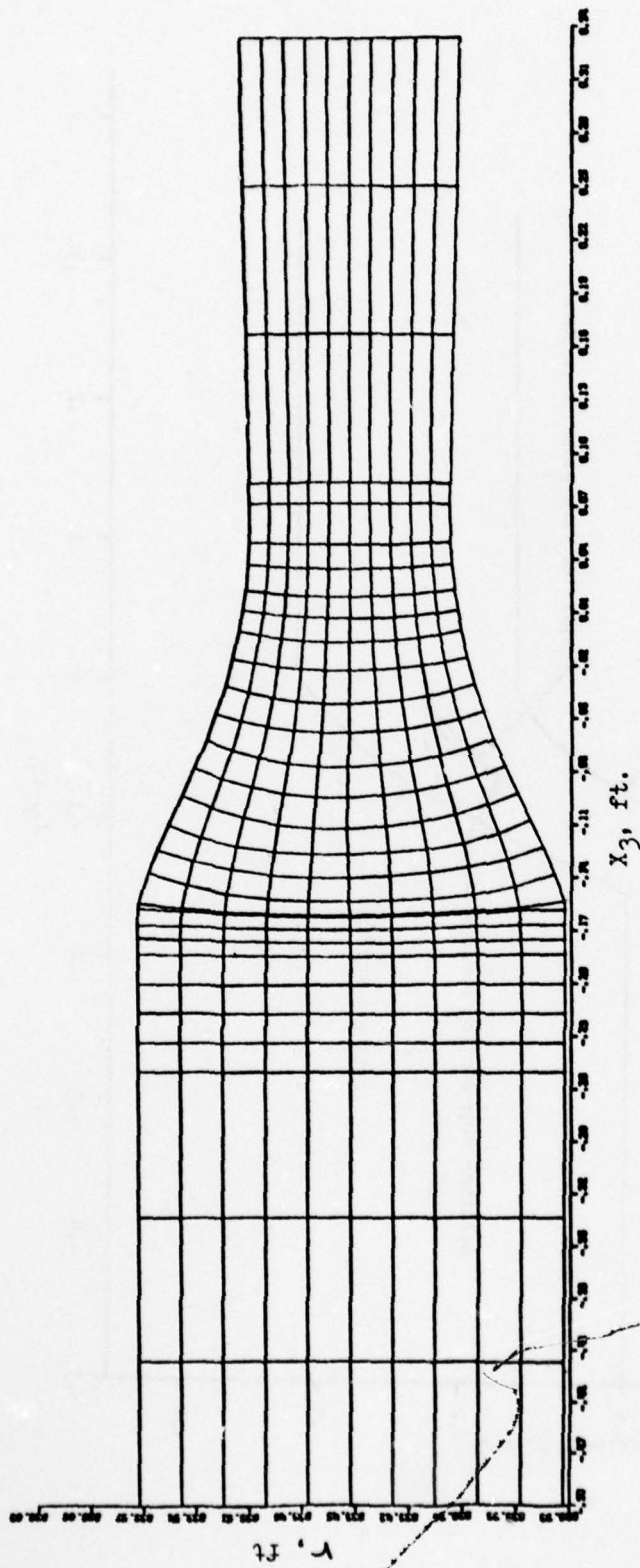
Figure 9. Generalized Orthogonal Coordinate System in the Meridional Plane; Coordinate System Composed of 11 Inviscid Streamlines and 31 Potential-like-lines.

72
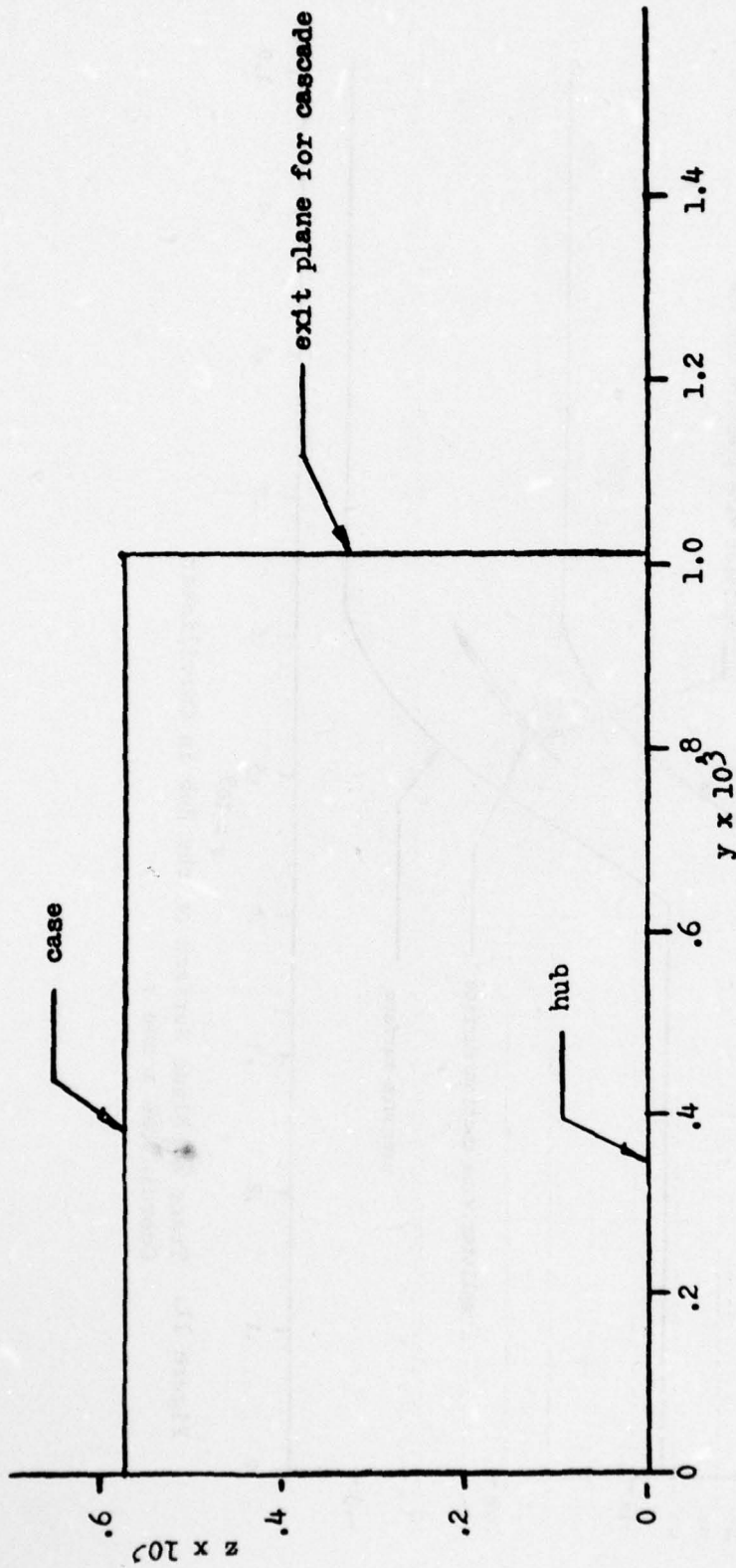
Figure 10. Mapping of Hub Line in Terms of Curvilinear Coordinates y and z.

73
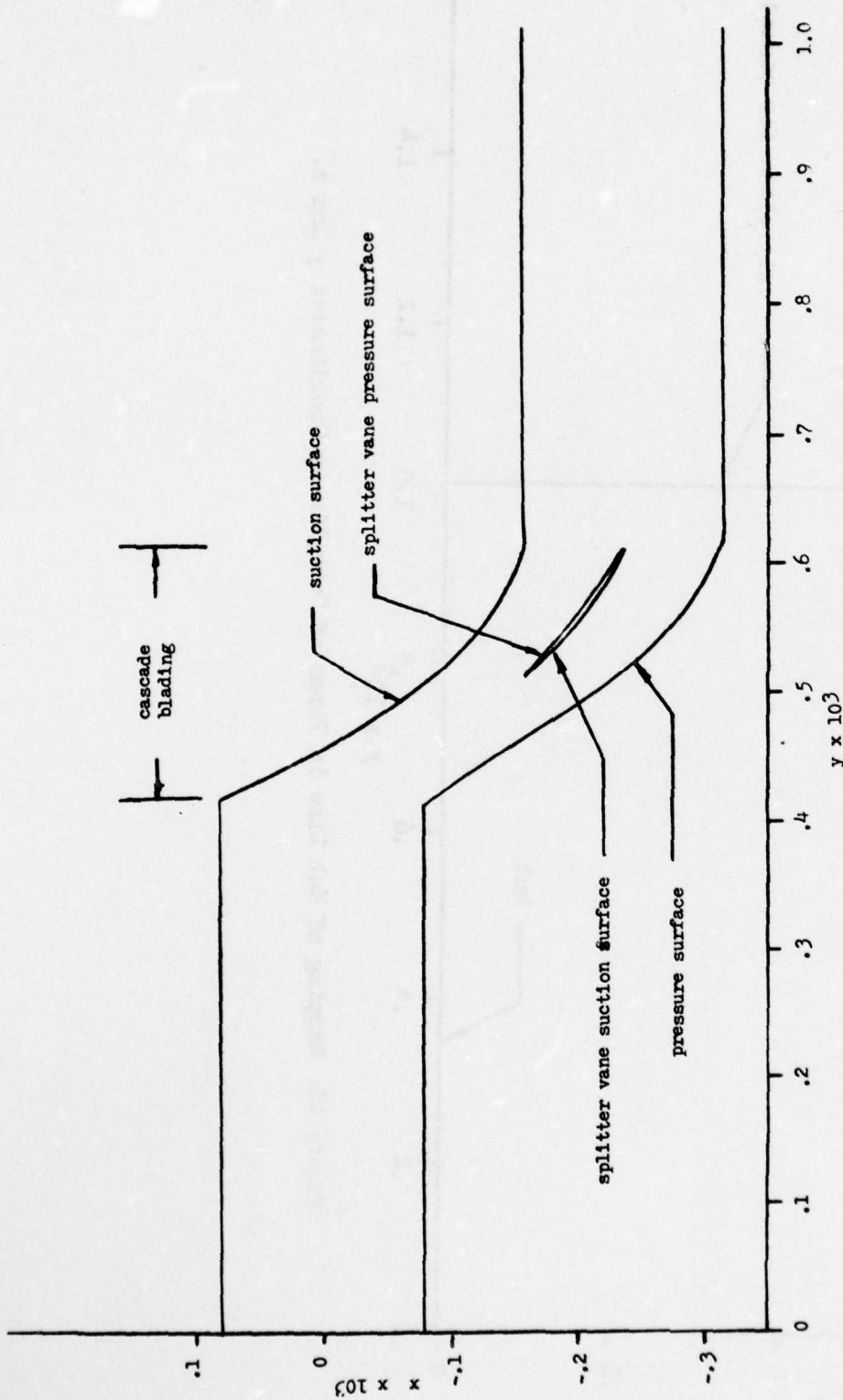
Figure 11. Trace of Blade Surface on the Hub in Curvilinear
Coordinates x and y.

74

y, radians
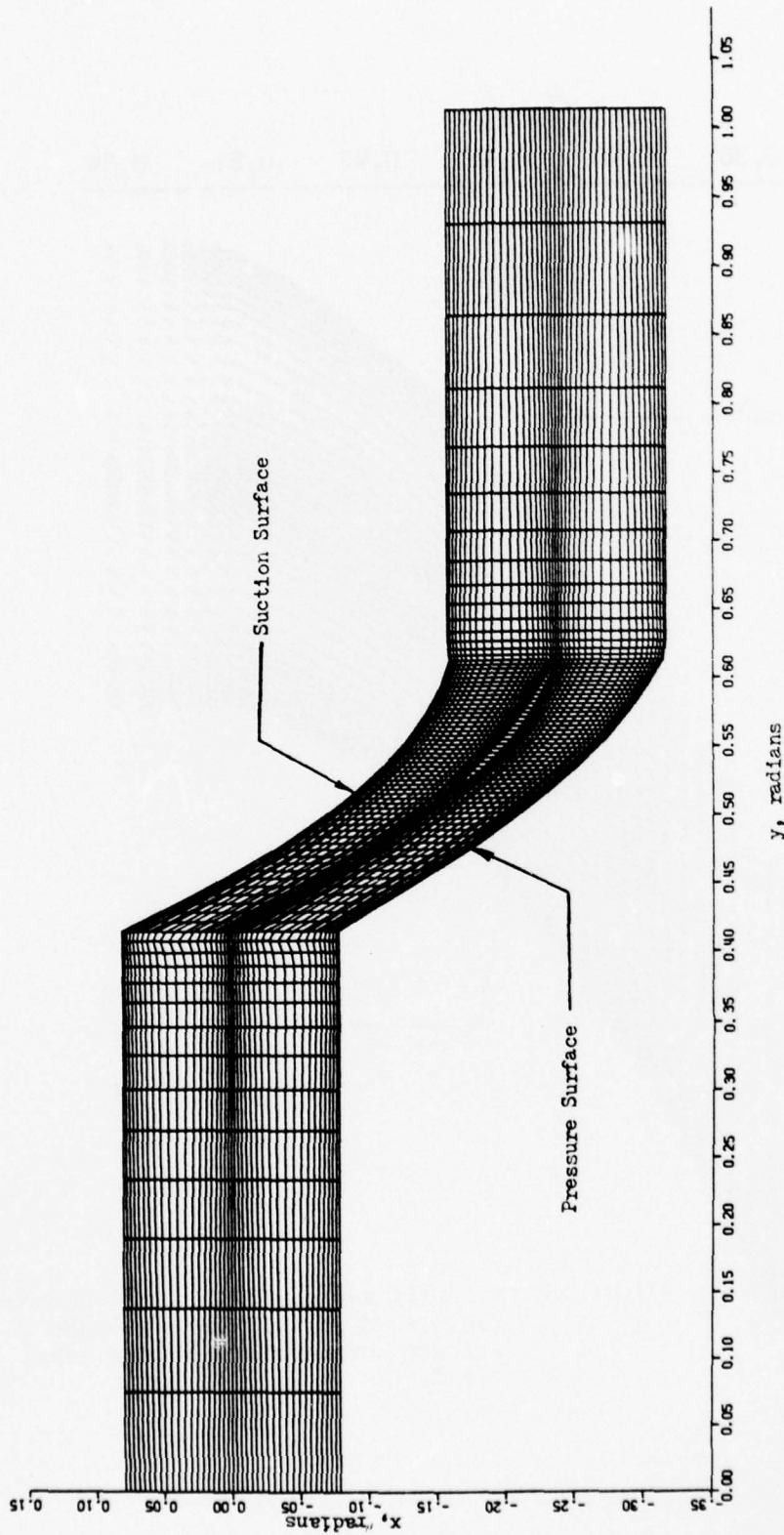
Figure 12 Finite difference mesh on the hub blade-to-blade surface, z=0; the parameters x and y correspond to curvilinear coordinates on this surface; the mesh is comprised of 42 streamline-like-lines and 80 potential-like-lines.

Figure 13. Velocity vector plot of the cascade flow field on the blade-to-blade surface corresponding to the hub; z = 0.
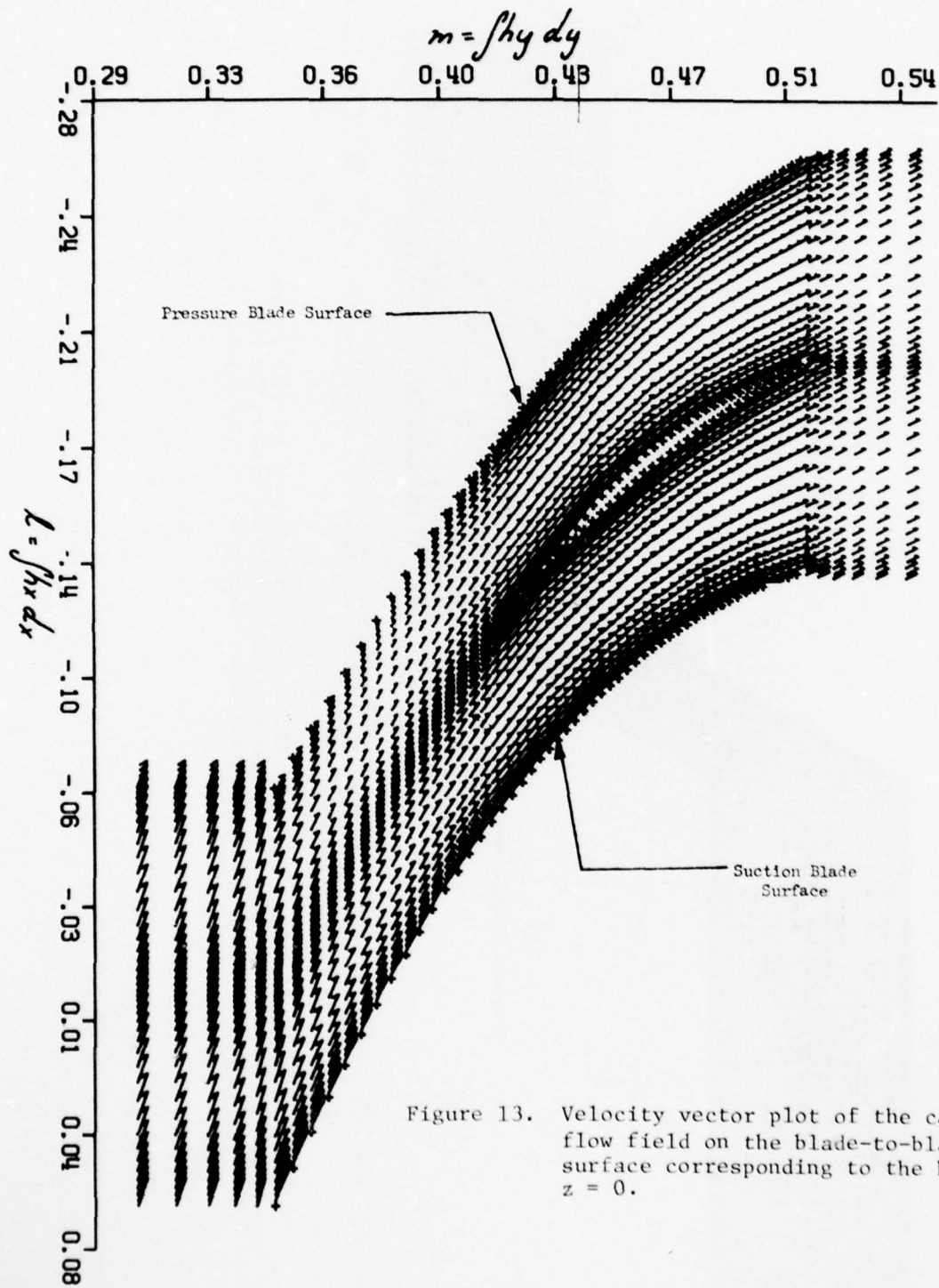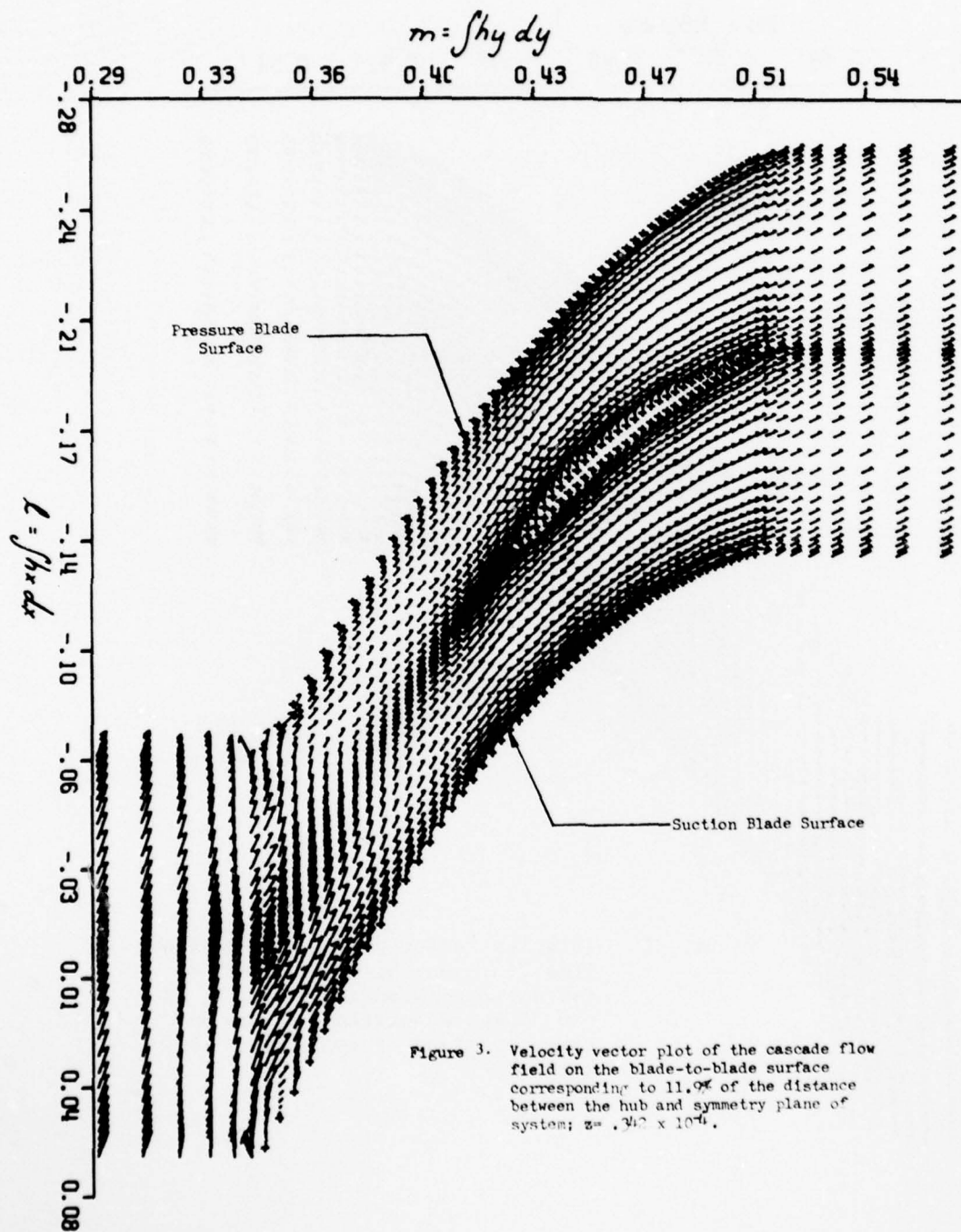
Figure 3. Velocity vector plot of the cascade flow field on the blade-to-blade surface corresponding to 11.9% of the distance between the hub and symmetry plane of system; z= .342 x 10⁻⁴.

$m = \int hy\, dy$

Pressure Blade
Surface

Suction Blade
Surface

$\ell = \int h_x\, dx$
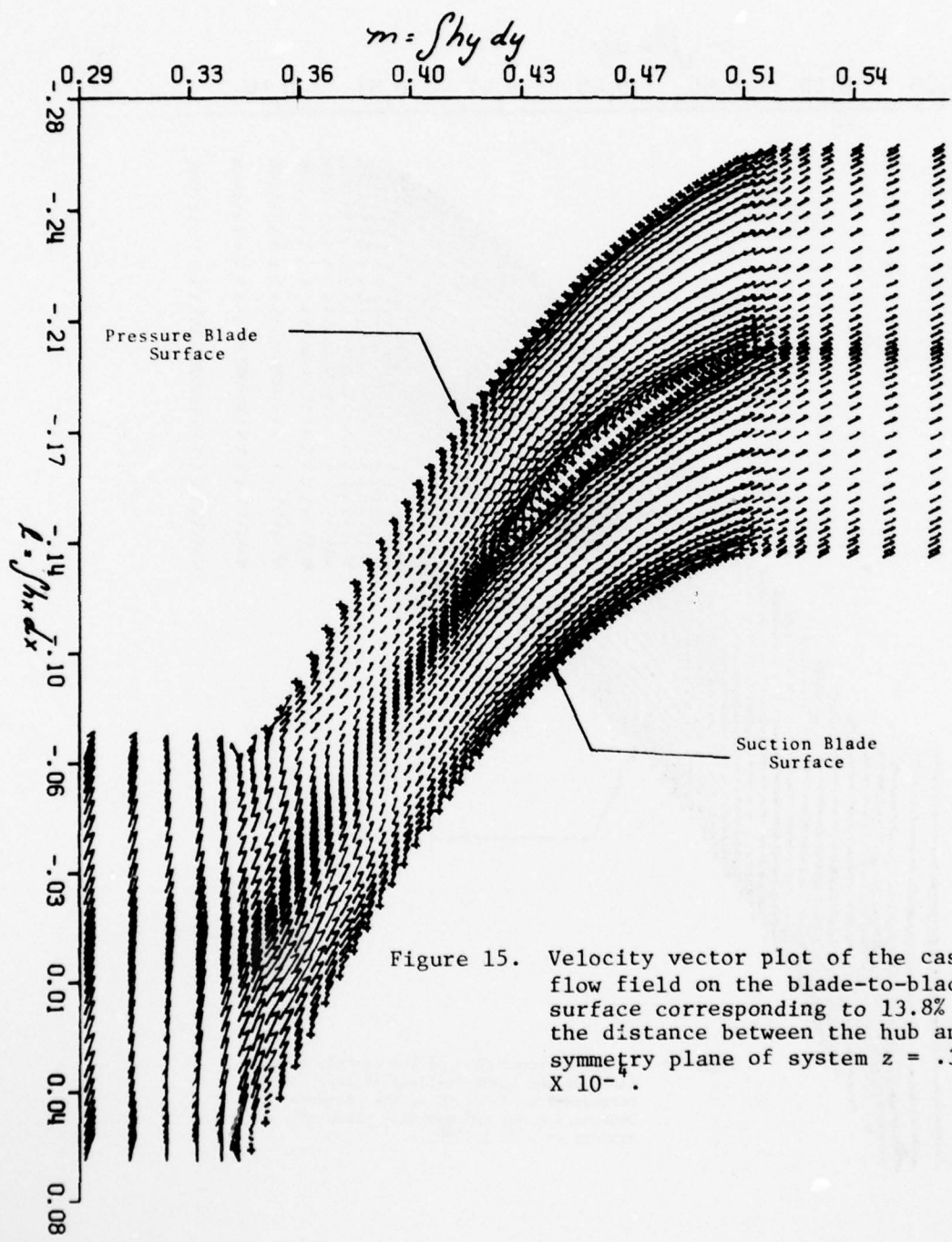
Figure 15. Velocity vector plot of the cascade
flow field on the blade-to-blade
surface corresponding to 13.8% of
the distance between the hub and
symmetry plane of system z = .397
X 10⁻⁴.

78

$$m = \int hy\,dy$$

Pressure Blade Surface

Suction Blade Surface

$$\ell = \int hx\,dx$$
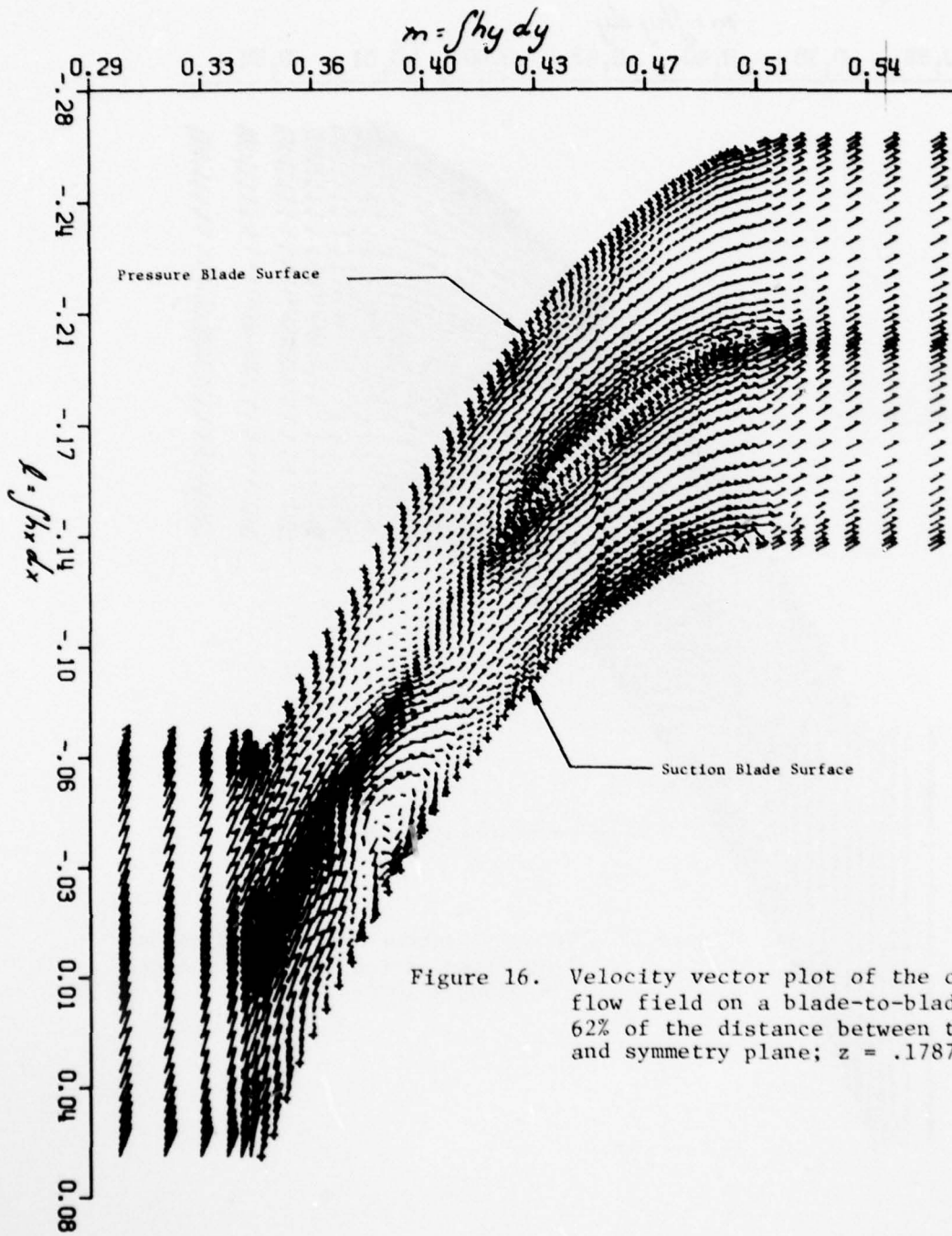
Figure 16. Velocity vector plot of the cascade
flow field on a blade-to-blade surface
62% of the distance between the hub
and symmetry plane; $z = .1787 \times 10^{-3}$.

79
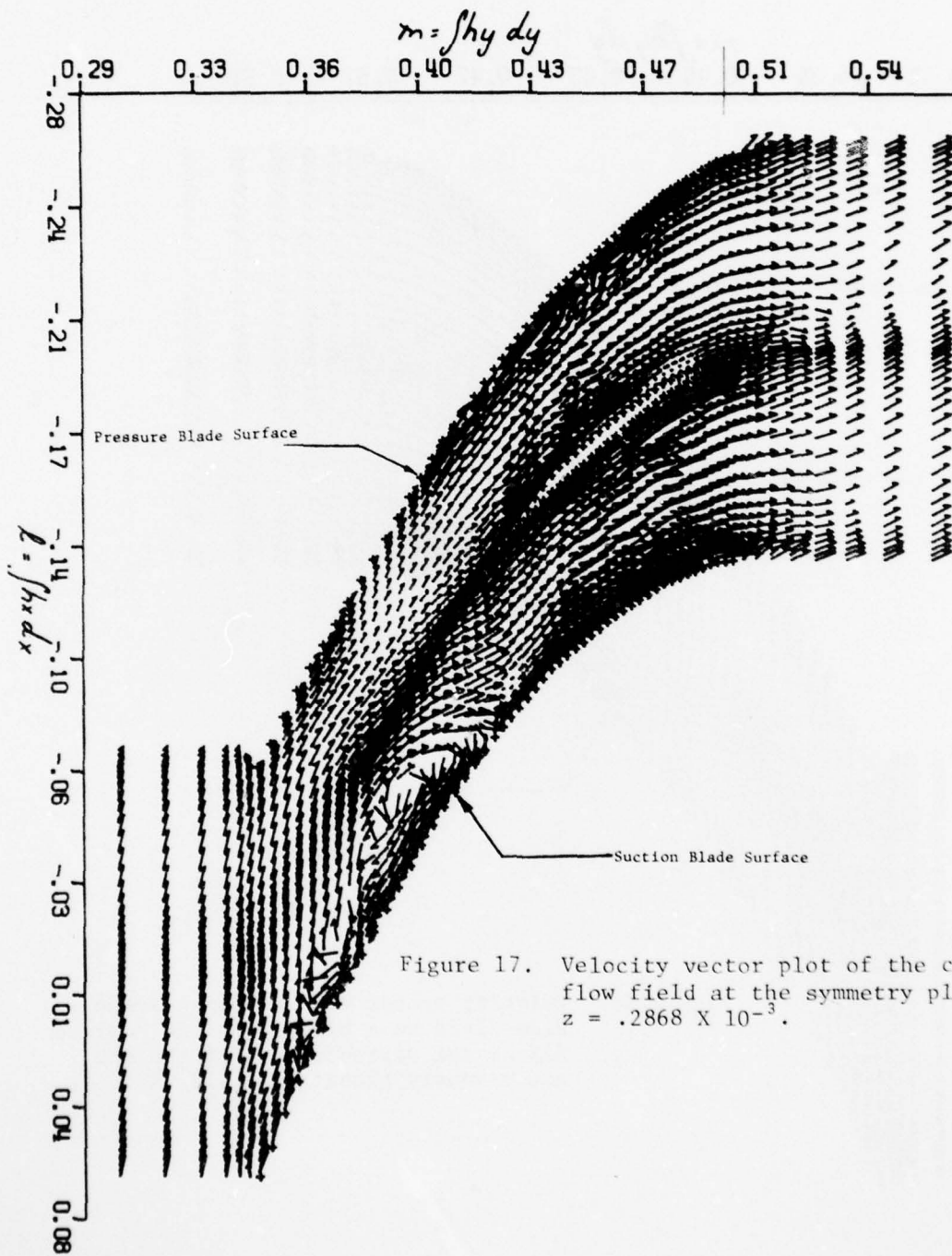
Figure 17. Velocity vector plot of the cascade flow field at the symmetry plane; $z = .2868 \times 10^{-3}$.
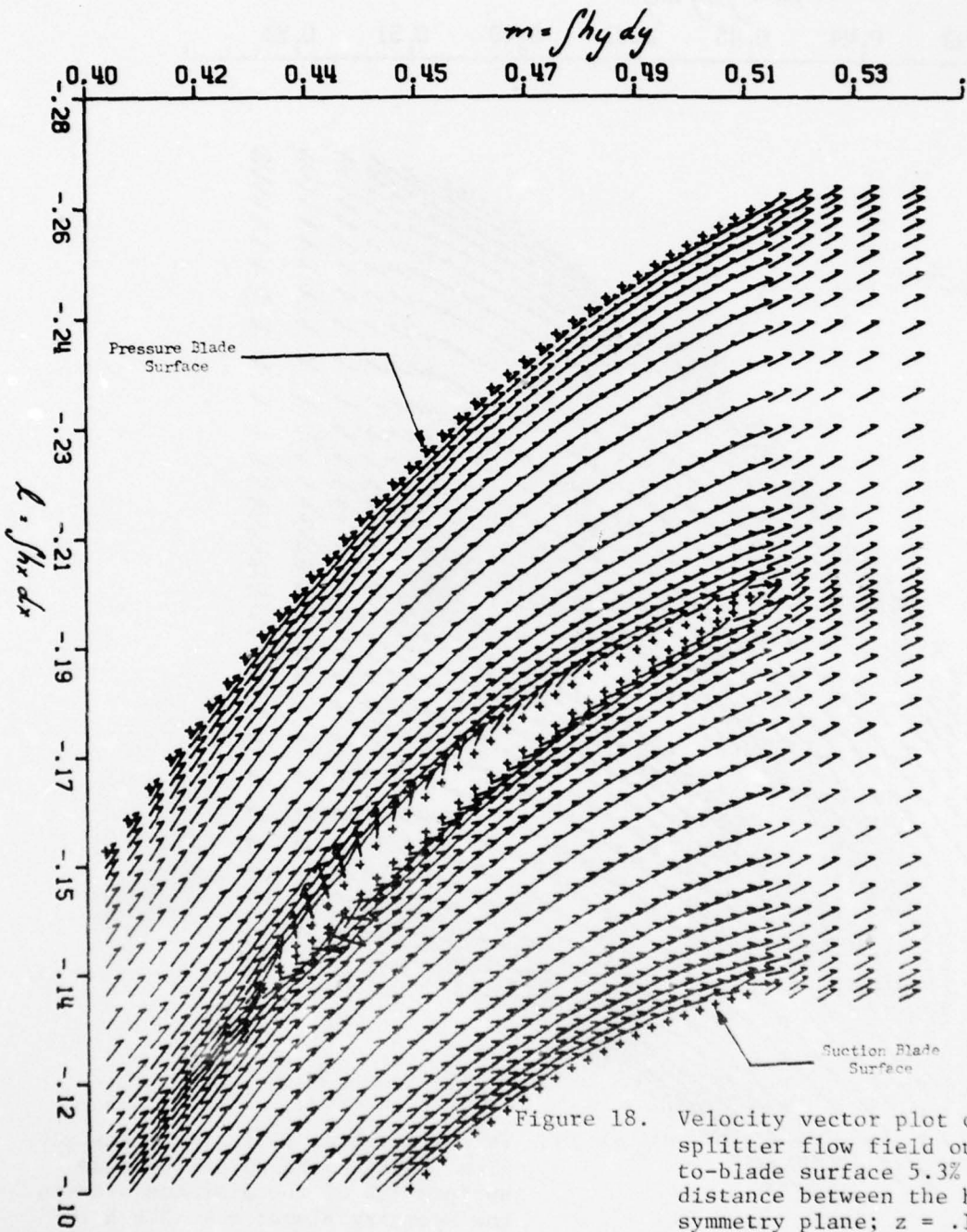
Figure 18. Velocity vector plot of the splitter flow field on a blade-to-blade surface 5.3% of the distance between the hub and symmetry plane; $z = .152 \times 10^{-4}$.

MICROCOPY RESOLUTION TEST CHART
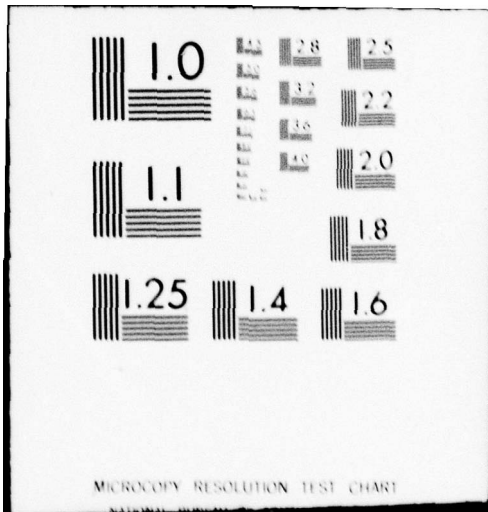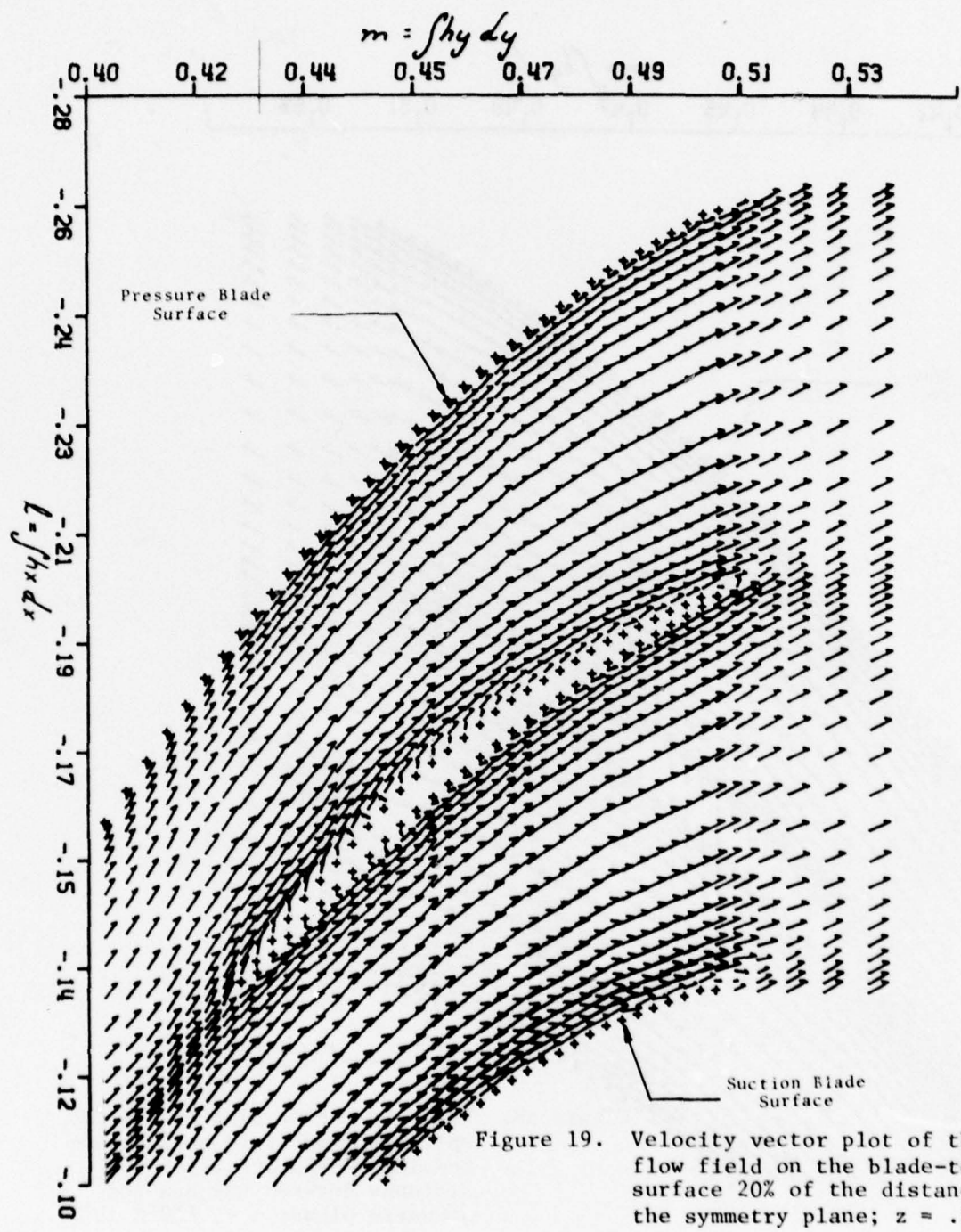
Figure 19. Velocity vector plot of the cascade flow field on the blade-to-blade surface 20% of the distance between the symmetry plane; z = .576 X 10^{-4}.

Figure 20. Velocity vector plot of the splitter flow field on a blade-to-blade surface 28% of the distance between the hub and symmetry plane; $z = .801 \times 10^{-4}$.
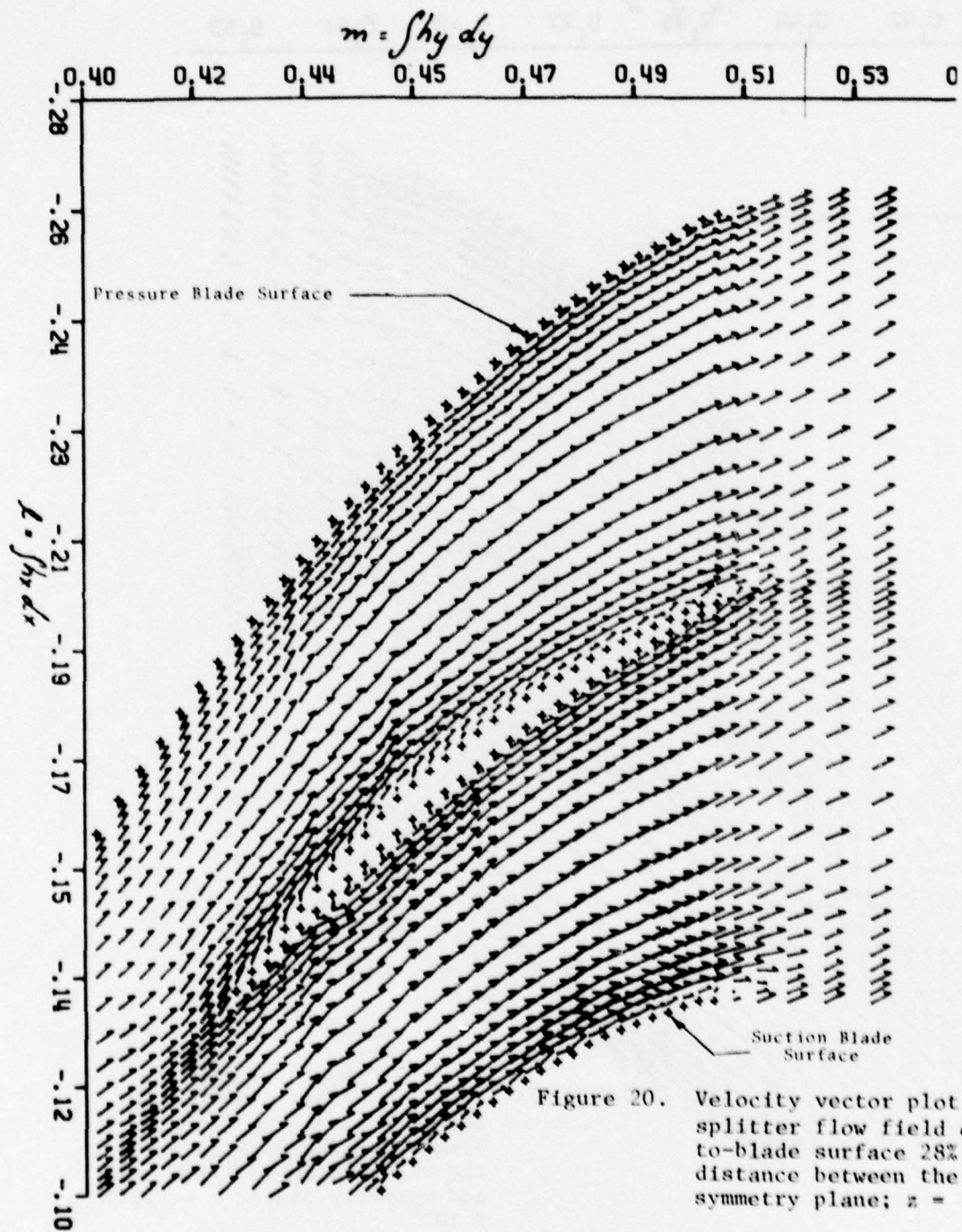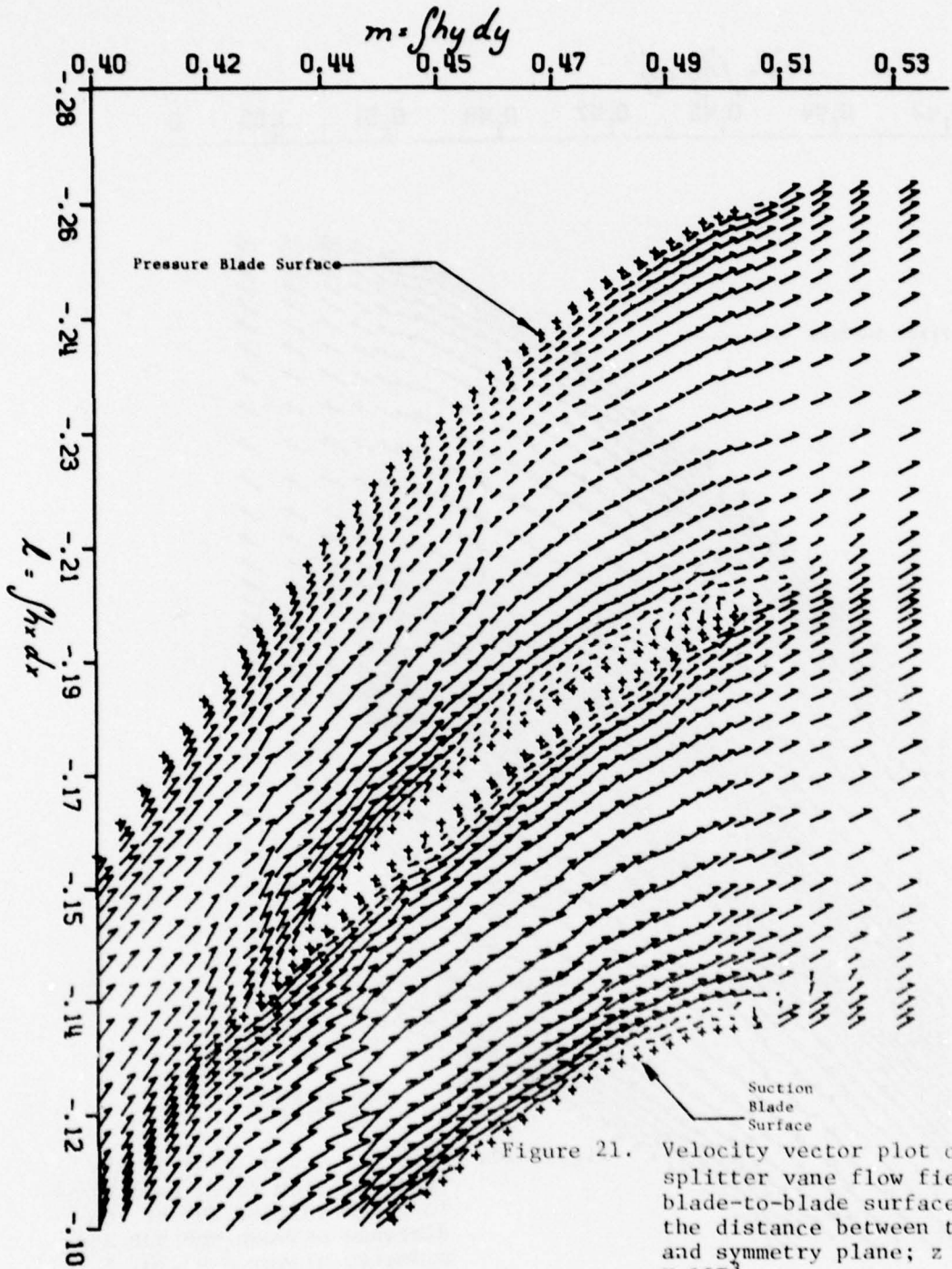
Figure 21. Velocity vector plot of the splitter vane flow field on a blade-to-blade surface 50% of the distance between the hub and symmetry plane; z = .1417 X 10⁻³

84
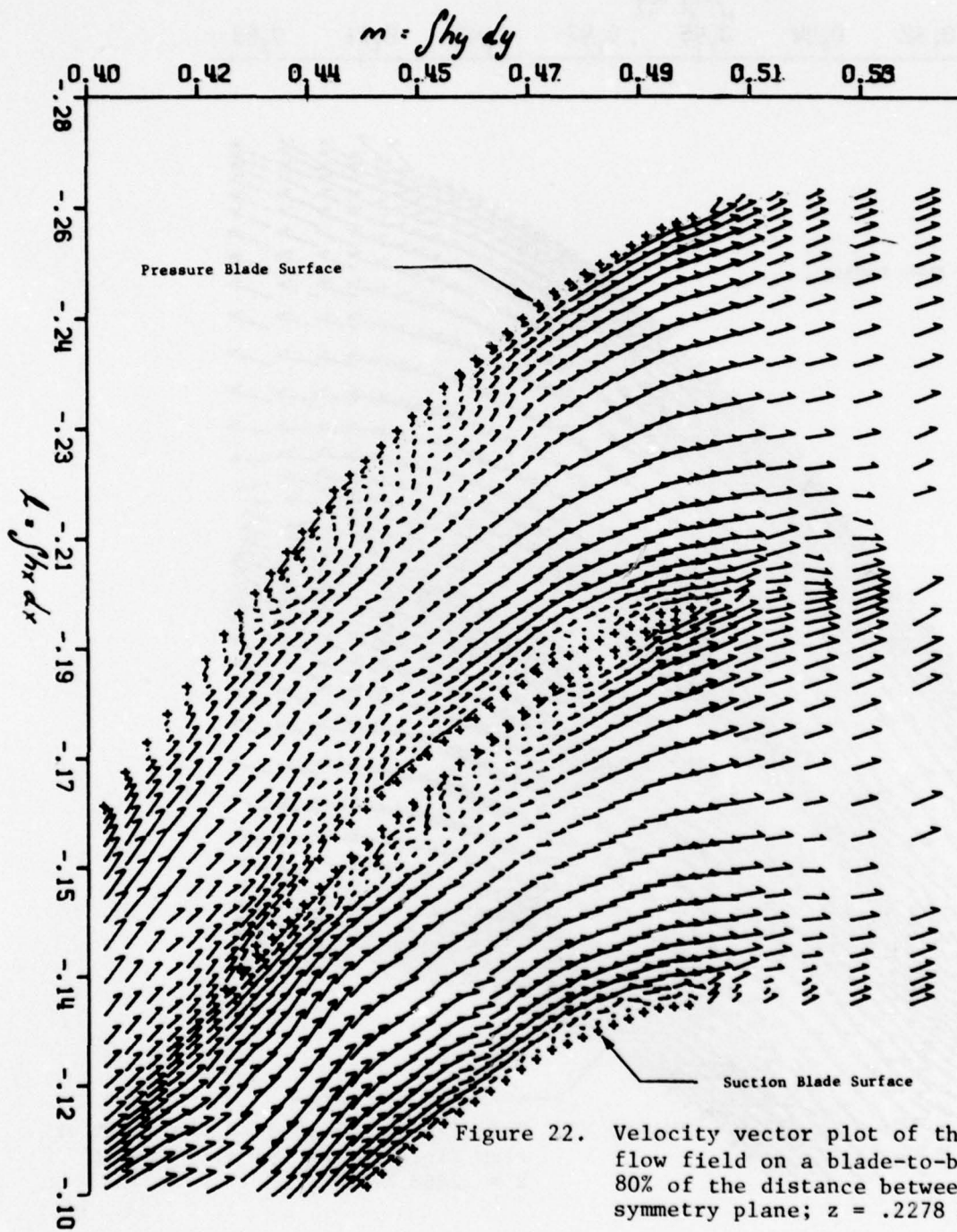
Figure 22. Velocity vector plot of the splitter flow field on a blade-to-blade surface 80% of the distance between the hub and symmetry plane; $z = .2278 \times 10^{-3}$.
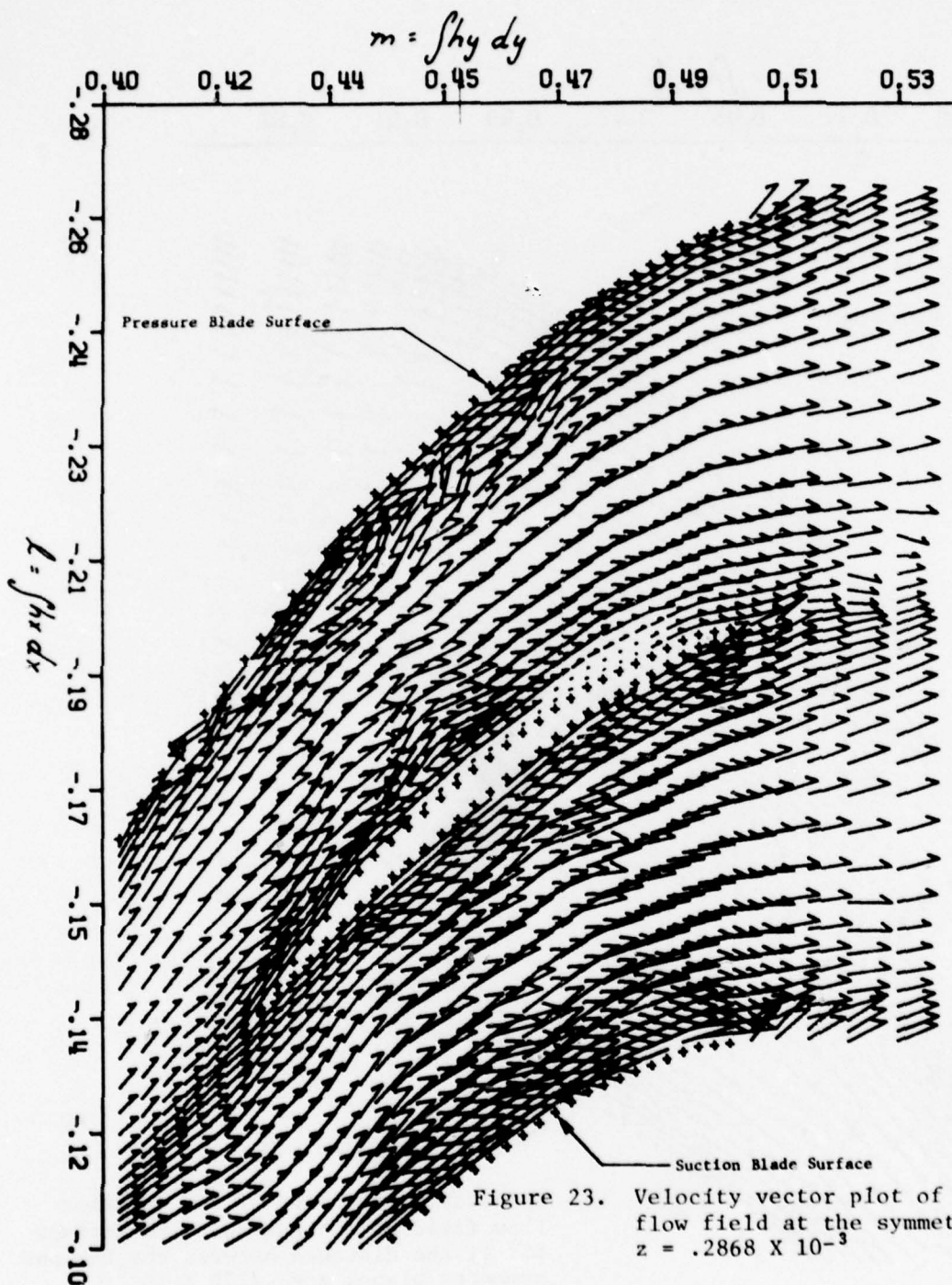
Figure 23. Velocity vector plot of the splitter flow field at the symmetry plane; $z = .2868 \times 10^{-3}$

86
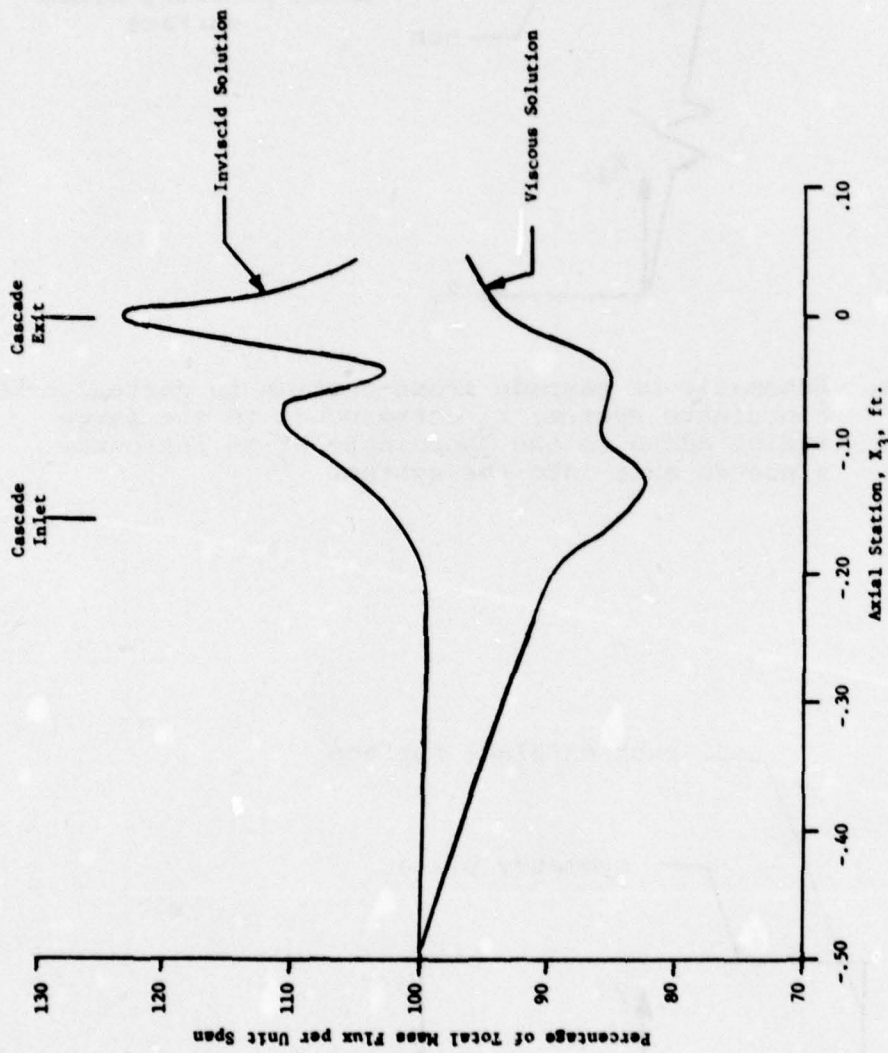
Figure 24. Percentage of total mass flux per unit span as a function of axial station on the blade-to-blade surface corresponding to the hub of the system; the total mass flux per unit span is defined as the mass flux per passage divided by the total increment in the curvilinear coordinate z; total mass per unit span = 1142 $\frac{lbs}{sec\text{-}radian}$

87
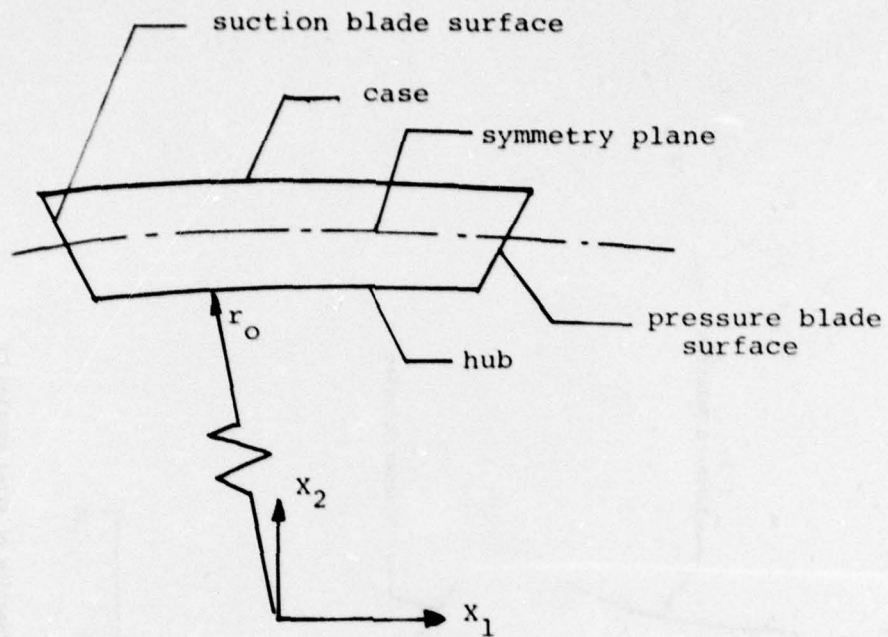
Figure 25a. Schematic of cascade cross-section in cartesian coordinate system; r_o corresponds to the large radius added to the coordinate X_2 to introduce a pseudo axis into the system.
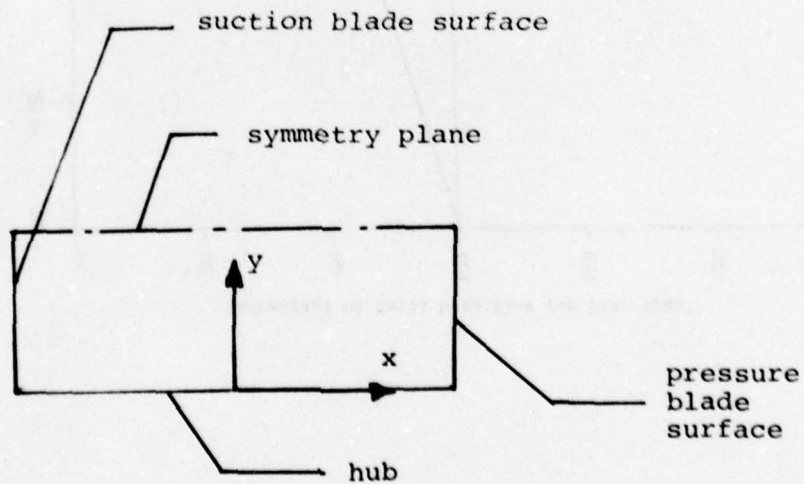
Figure 25b. Schematic of transformed cascade cross-section to the (x,y) curvilinear coordinates.

Symmetry Plane

Periodic ⟵

(No Slip)

Y

X   Hub

Periodic
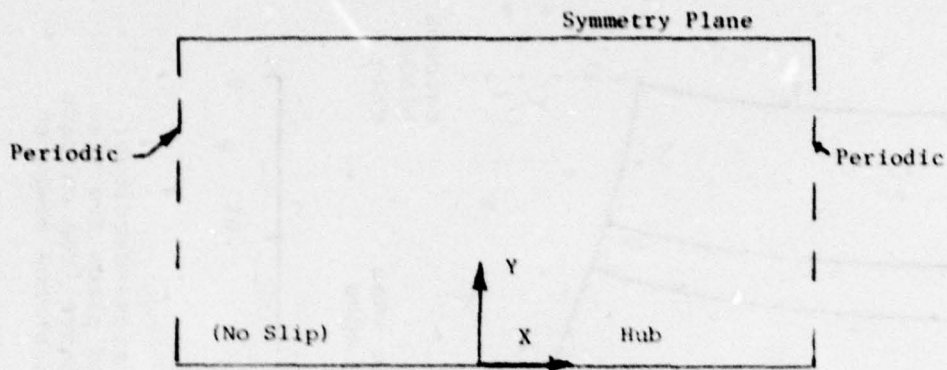
Figure 26c. Boundary Conditions on Cross-Sectional Planes
Downstream of Discharge

Suction Blade (No Slip)

Symmetry Plane

Splitter Vane
Pressure
Surface (No
Slip)

Splitter Vane
Suction Surface
(No Slip)

Pressure Blade
(No Slip)

Y

(No Slip)   X   Hub
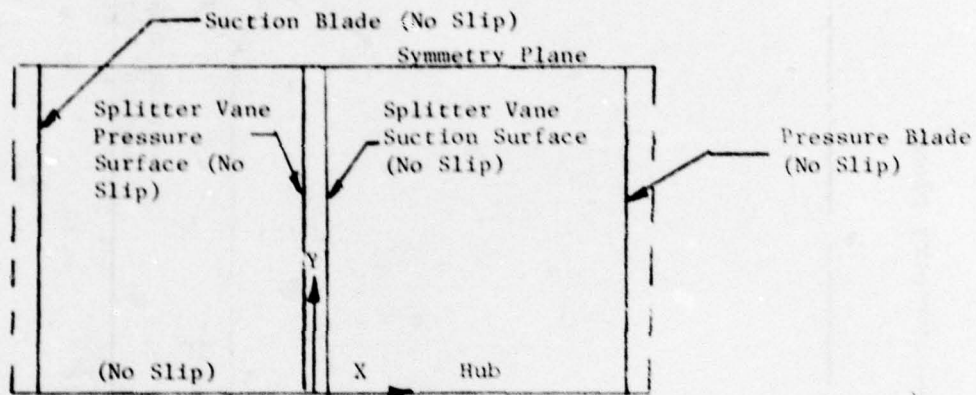
Figure 26b. Boundary Conditions on Cross-Sectional Planes
Within Blading Passage

Symmetry Plane

Periodic ⟵

Periodic

Y

X   Hub
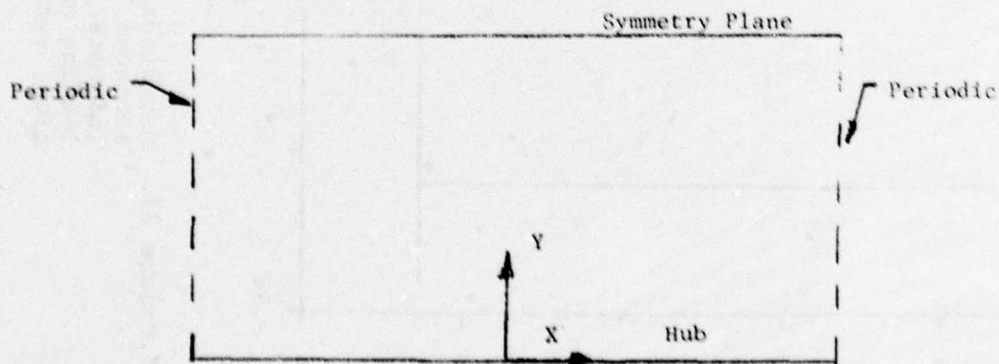
Figure 26a. Boundary Conditions on Cross-Sectional Planes
Upstream of the Cascade Blade Leading
Edge

89
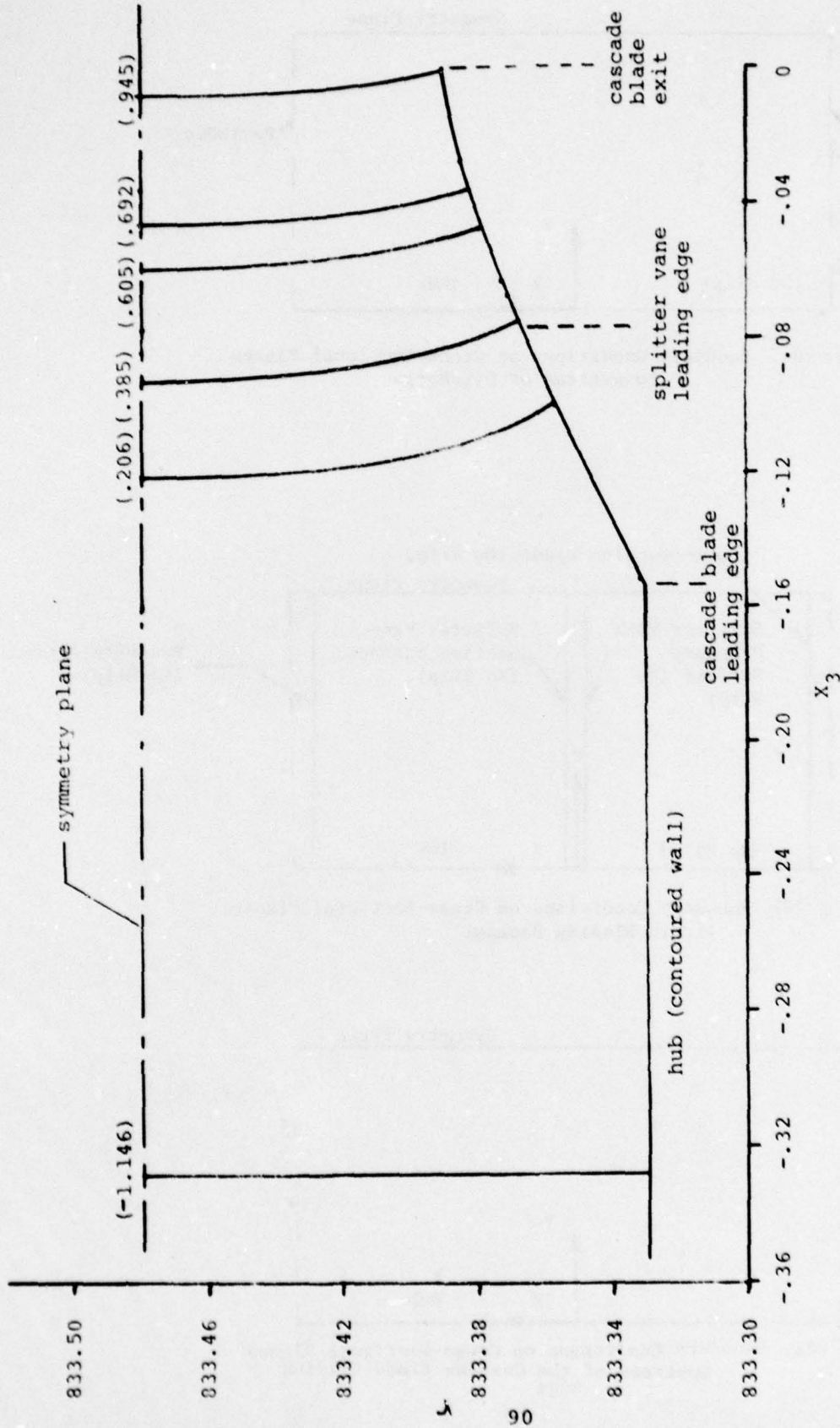
Figure 27. Meridional view of cascade contoured wall and symmetry plane; cross-sectional surfaces for which data reduction and interpretation have taken place are also indicated; numbers in parentheses indicate ratio of axial distance from cascade leading edge to total axial distance of cascade blade; axial distance measured along symmetry plane and denoted by symbol ℓ_r.
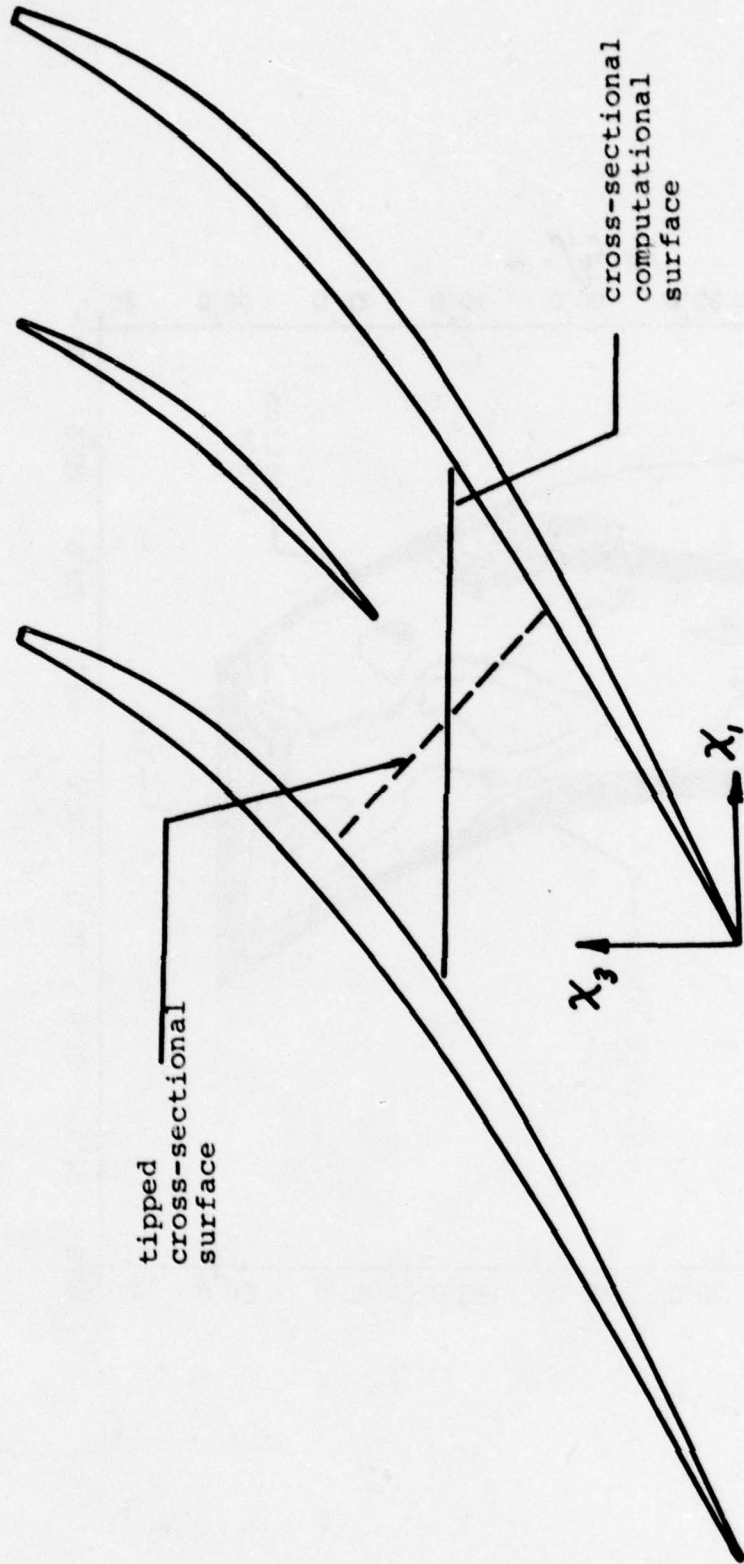
Figure 28. Blade-to-blade view of traces of computational cross-section and tipped cross-section.
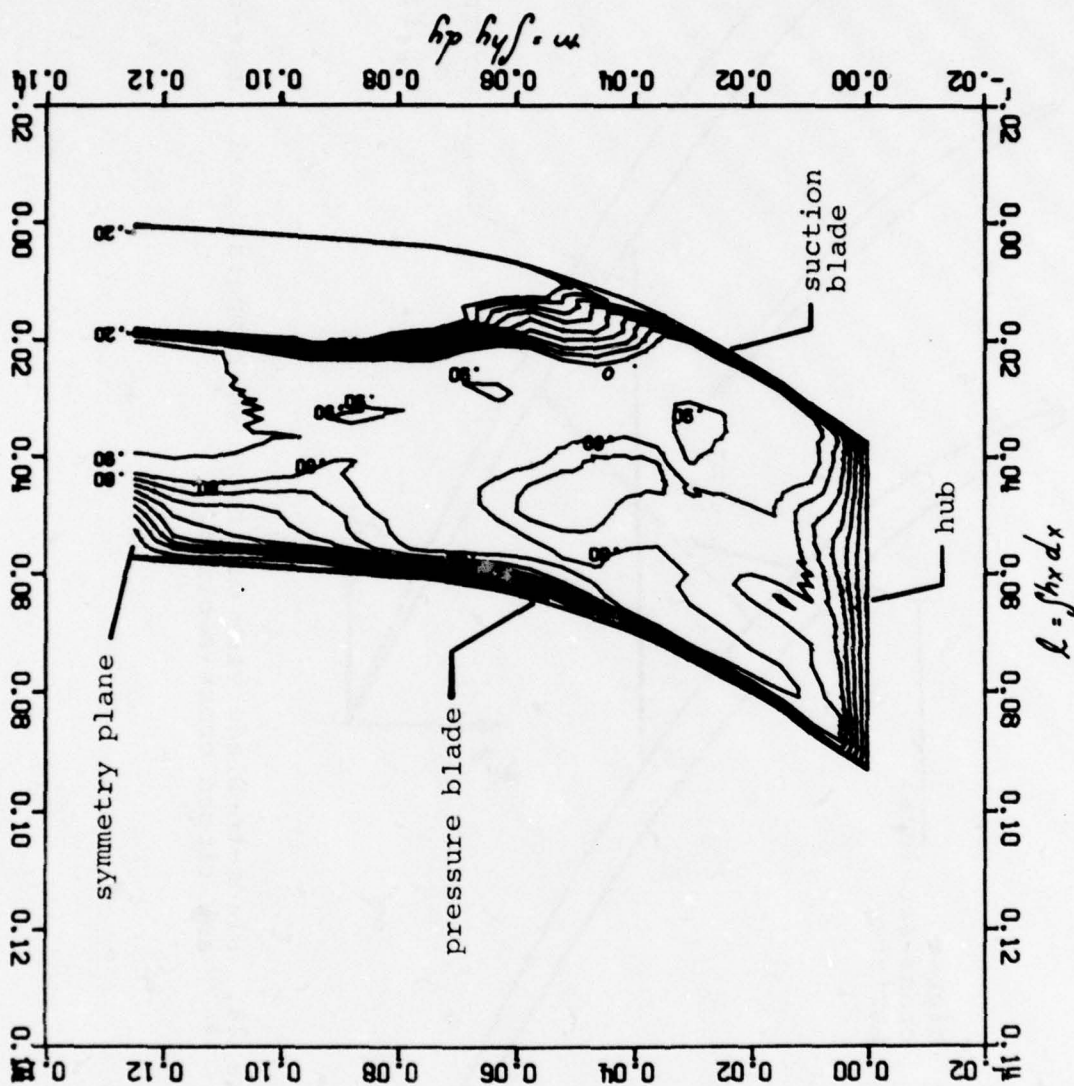
Figure 29. Contour plot of the streamwise velocity component on a cross-sectional surface located at an axial distance ratio ℓ_r of .206.
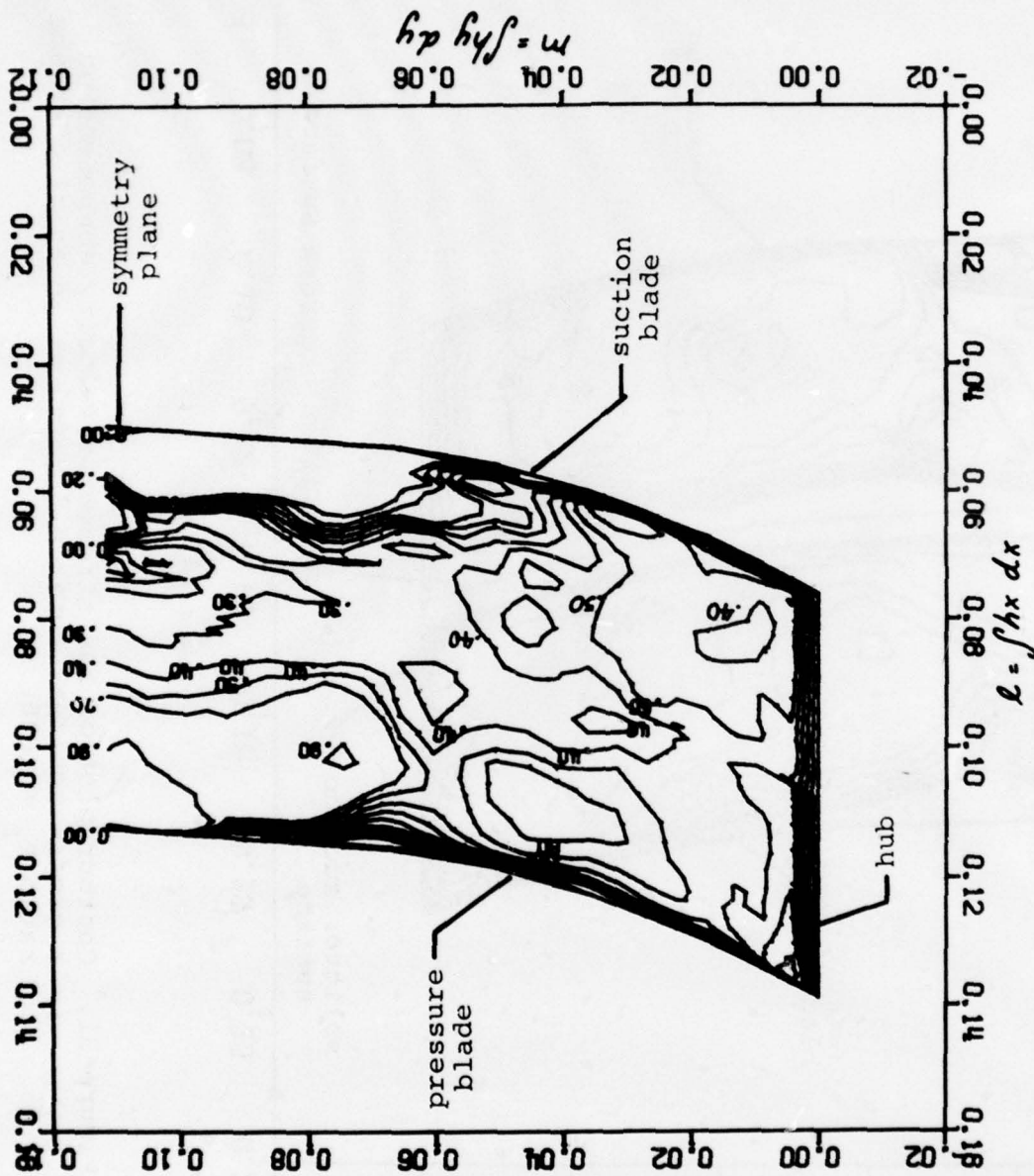
Figure 30. Contour plot of the streamwise velocity component on a cross-sectional surface located at an axial distance ratio $\ell_r = .385$.

93
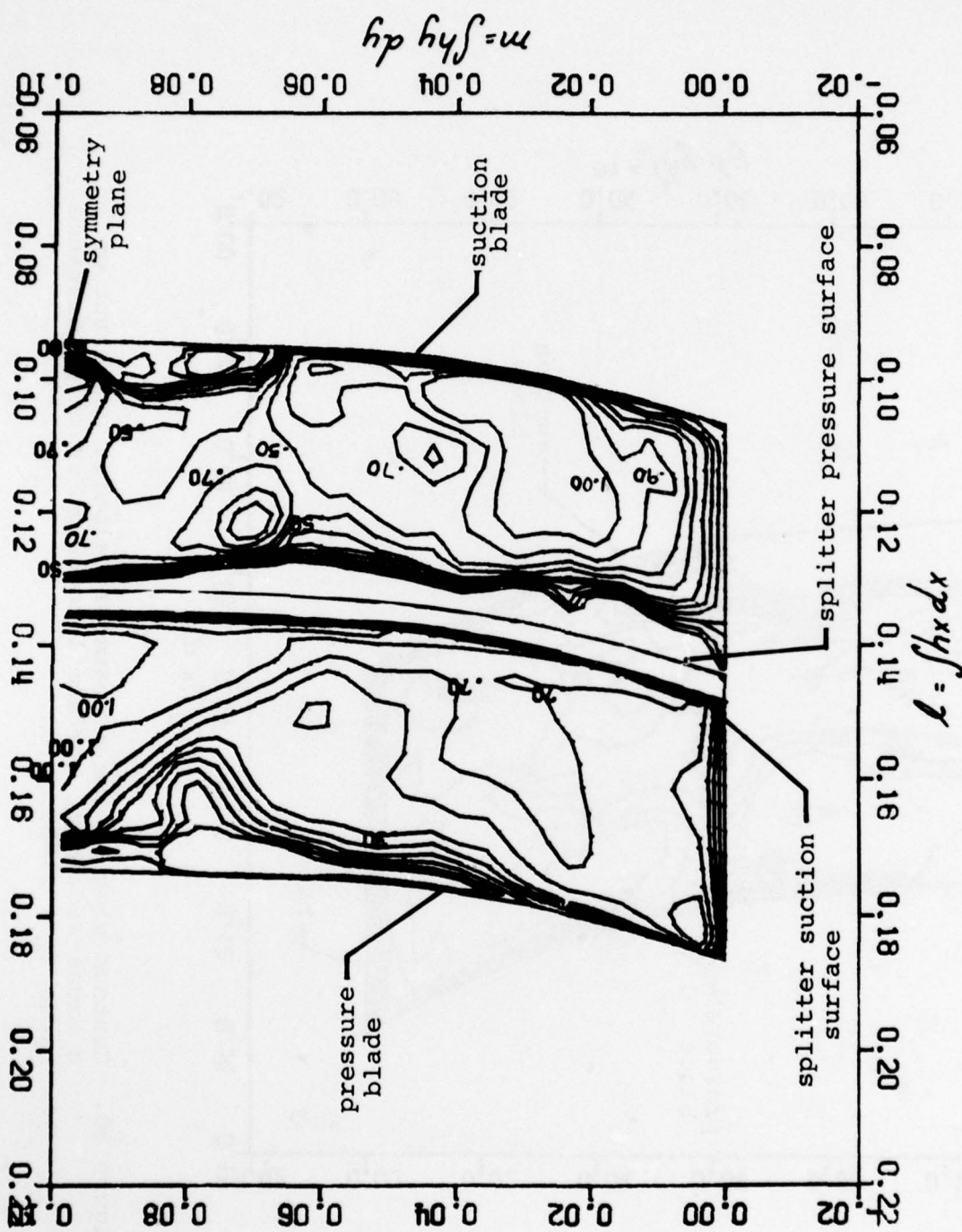
Figure 31. Contour plot of the streamwise velocity component on a cross-sectional surface located at an axial distance ratio $\ell_r = .605$.
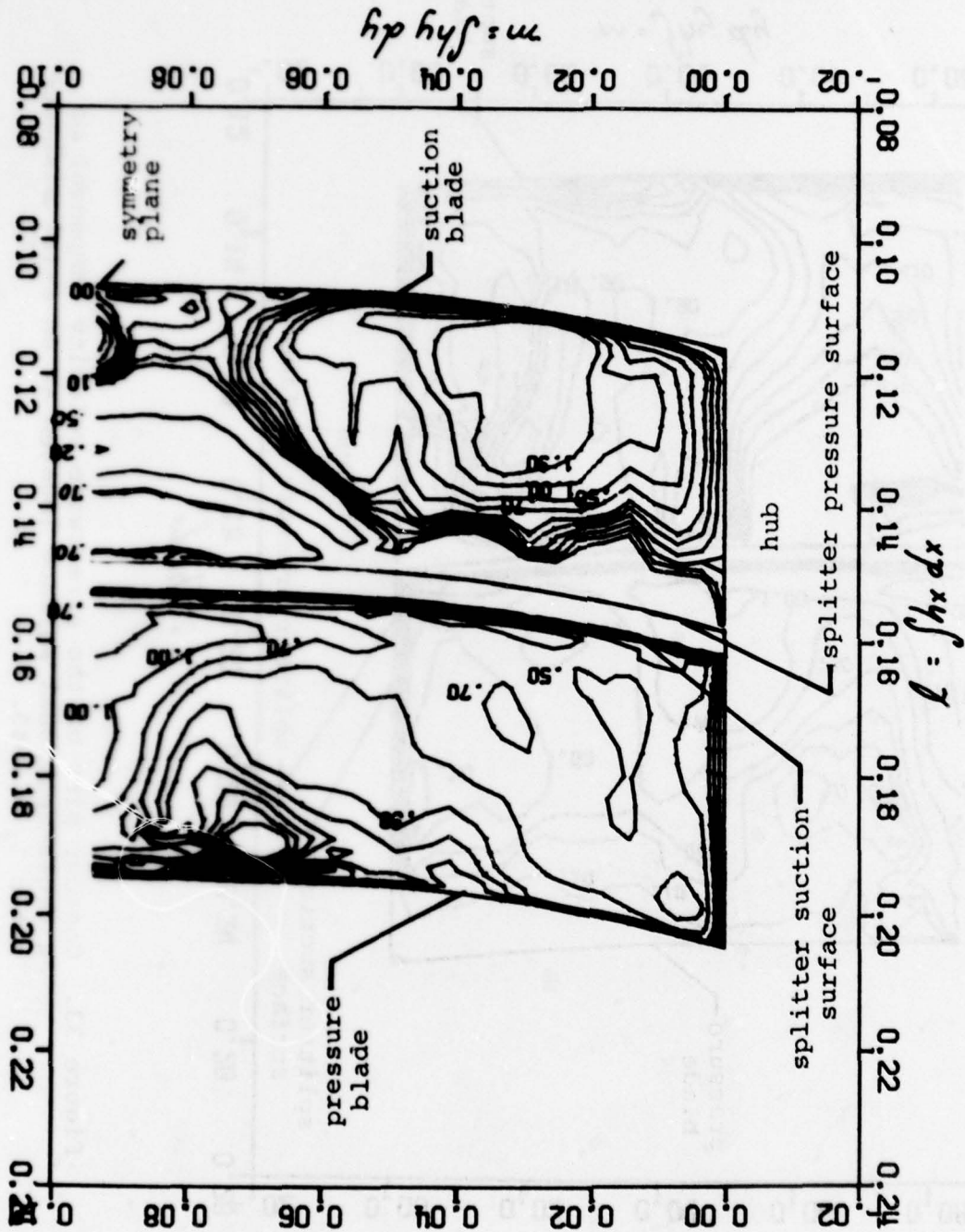
Figure 32. Contour plot of the streamwise velocity component on a cross-sectional surface located at an axial distance ratio $\ell_r = .692$.
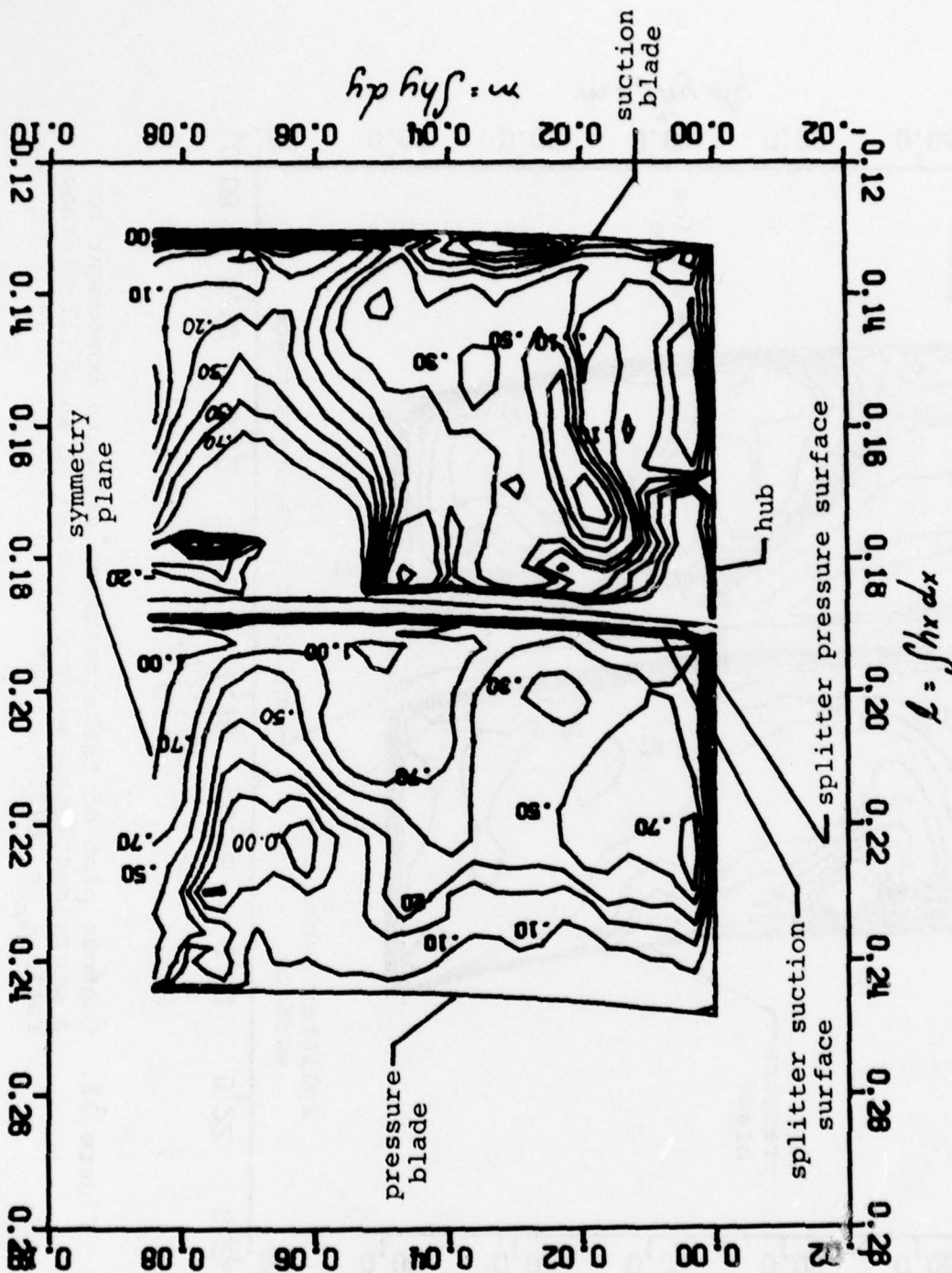
Figure 33. Contour plot of the streamwise velocity component on a cross-sectional surface located at an axial distance ratio $\ell_r = .945$.

96
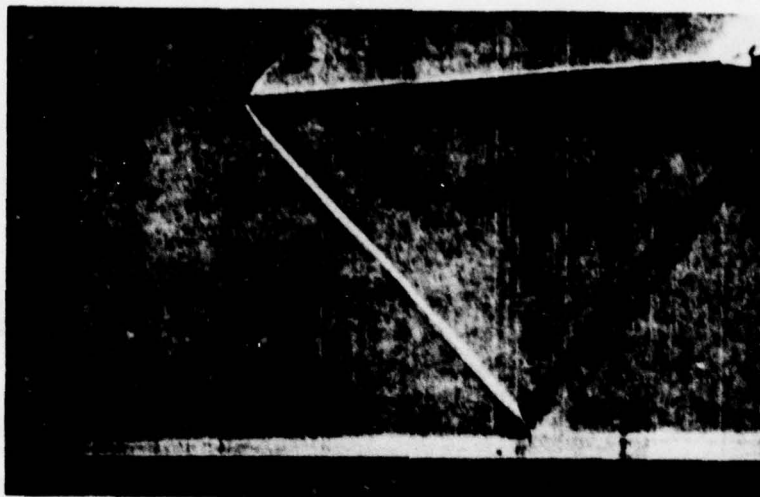
Figure 34.   Shock-wave turbulent boundary layer interaction
             on a flat plate; freestream Mach number is 1.45
             and the wedge angle is 4.5 degrees.
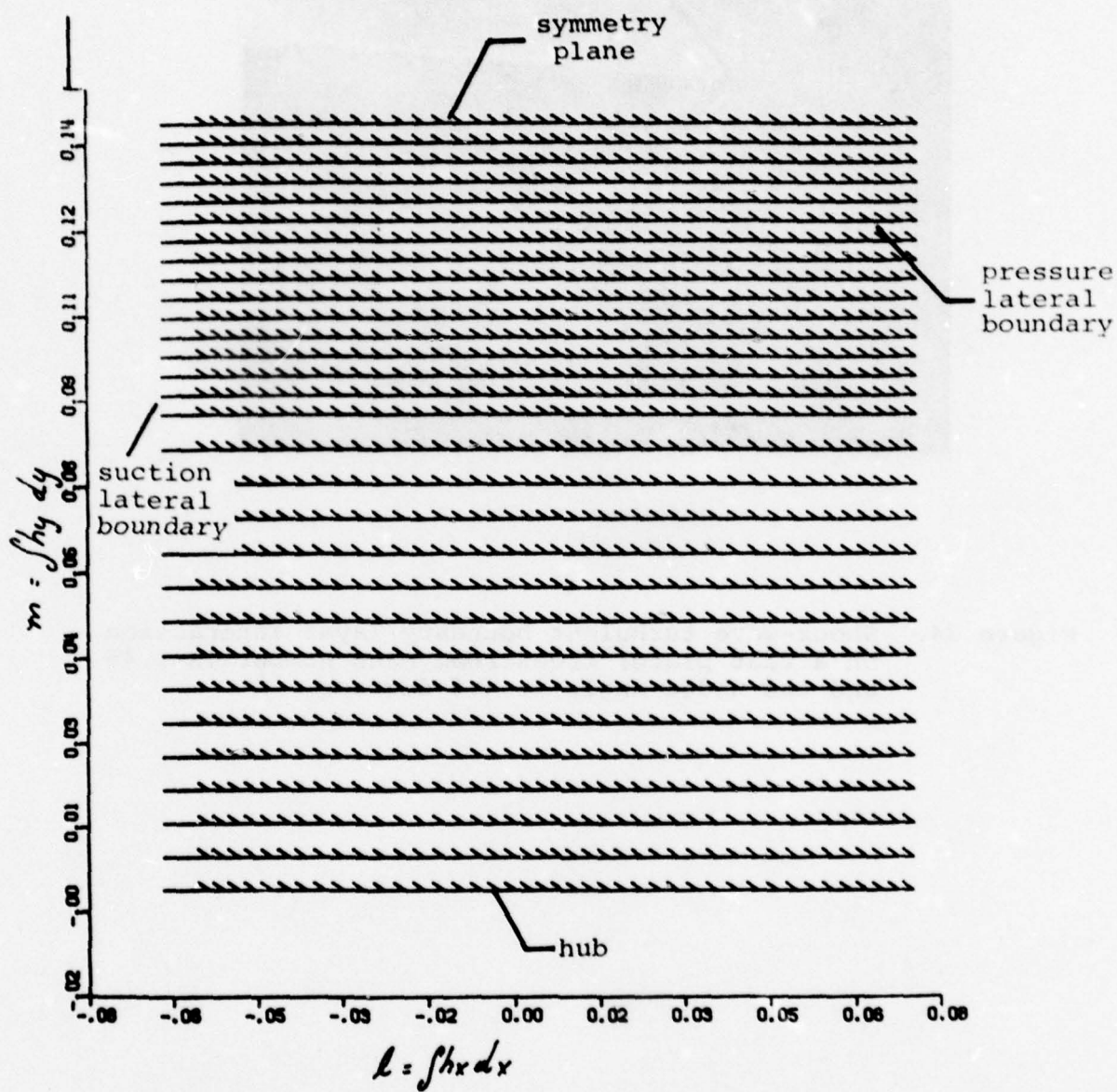
Figure 35. Velocity vector plot of cross-sectional flow field at an axial distance ratio ℓ_r of -1.146.
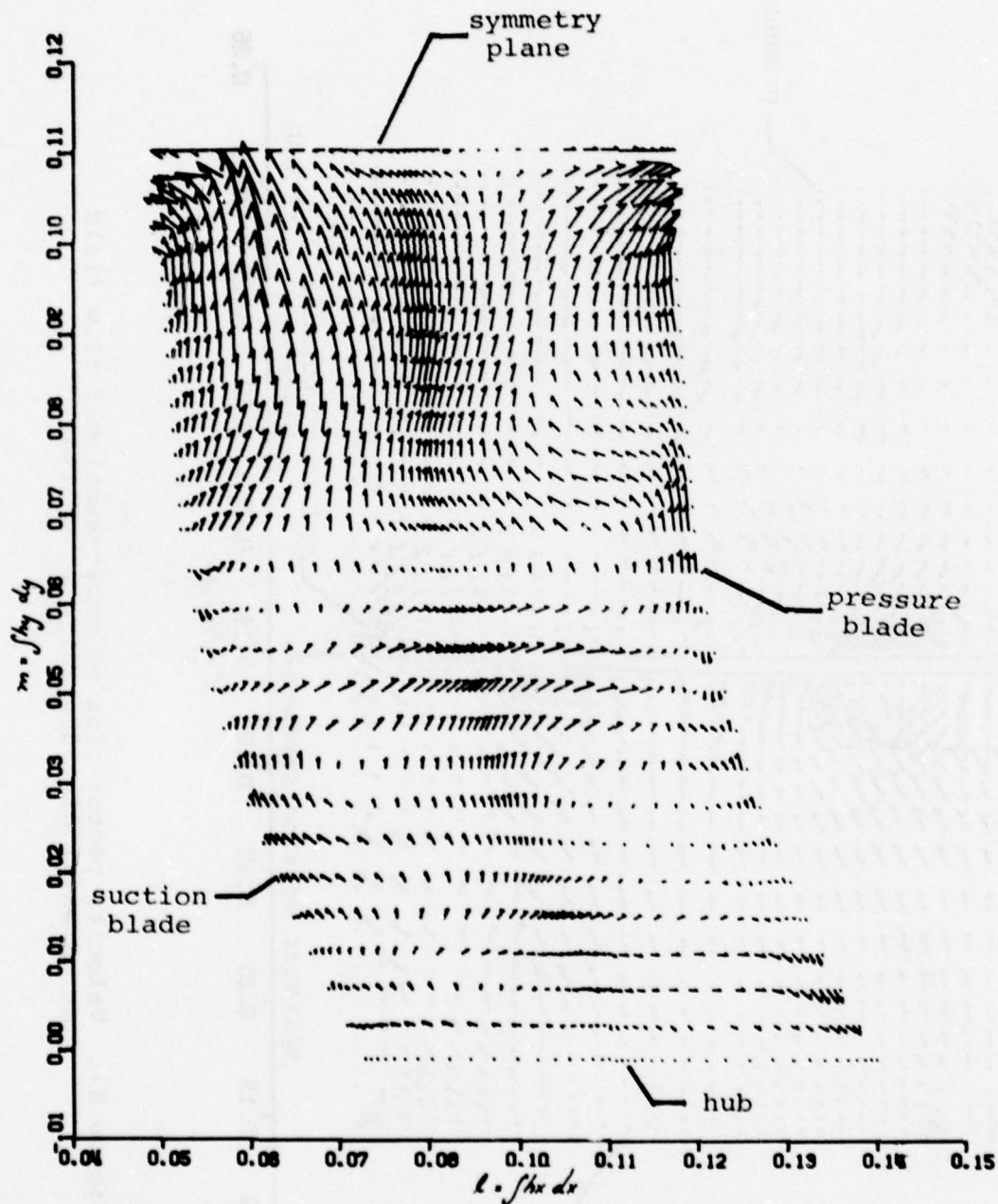
Figure 36. Velocity vector plot of cross-sectional flow field at
            an axial distance ratio ℓ_r of .385.

99
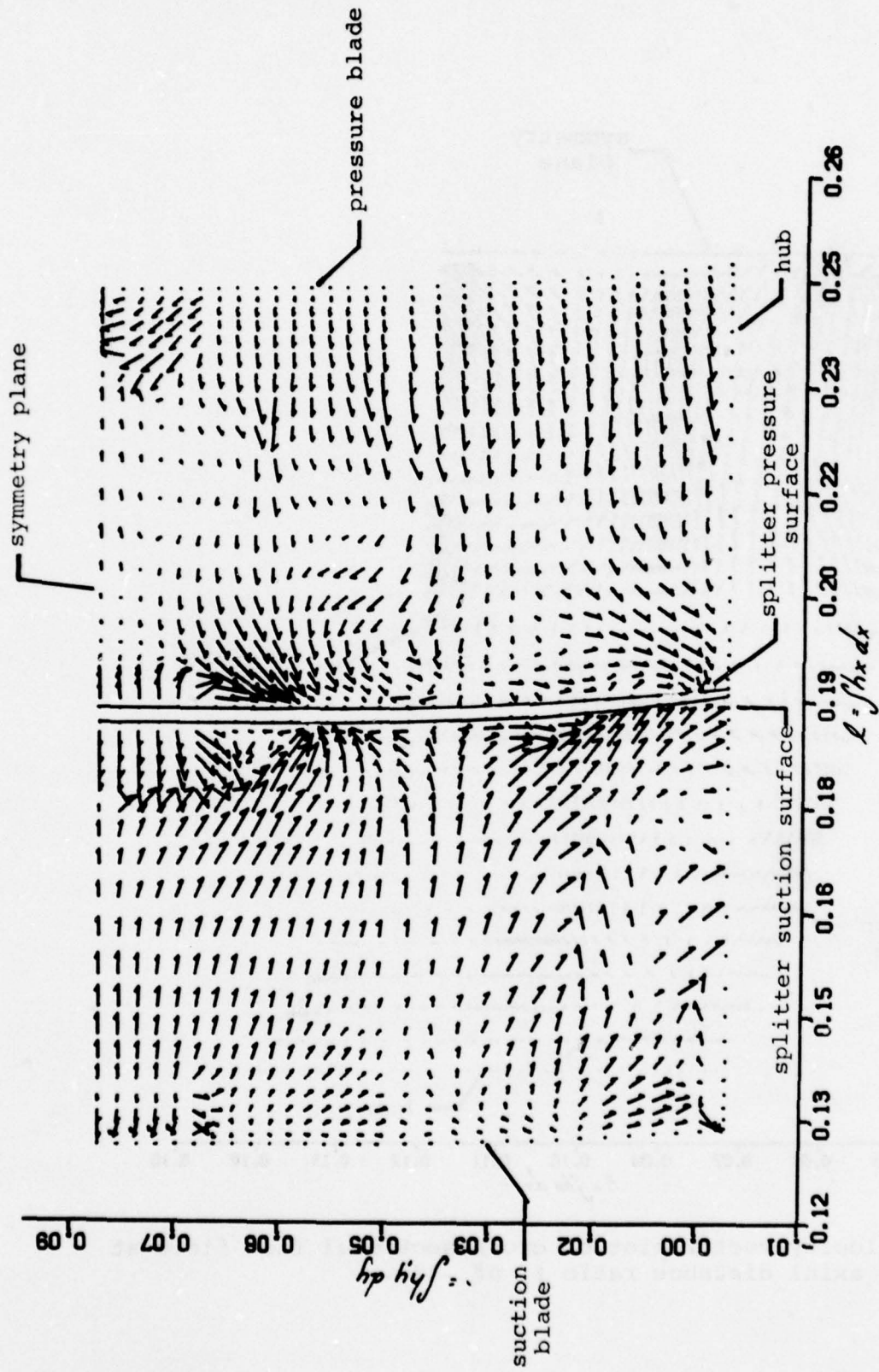
Figure 37. Velocity vector plot of cross-sectional flow field at an axial distance ratio ℓ_r of .945.
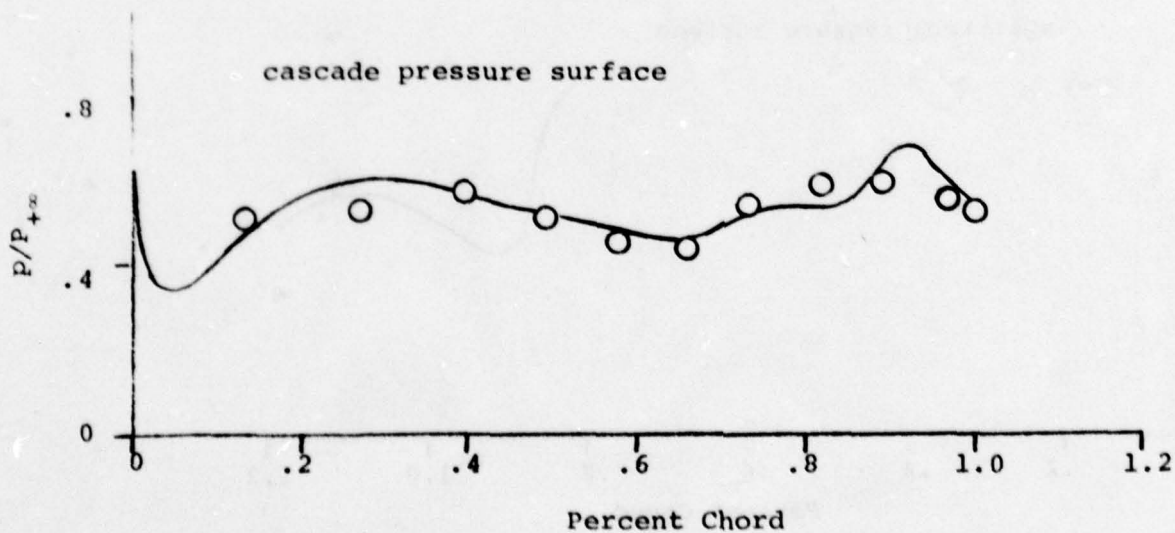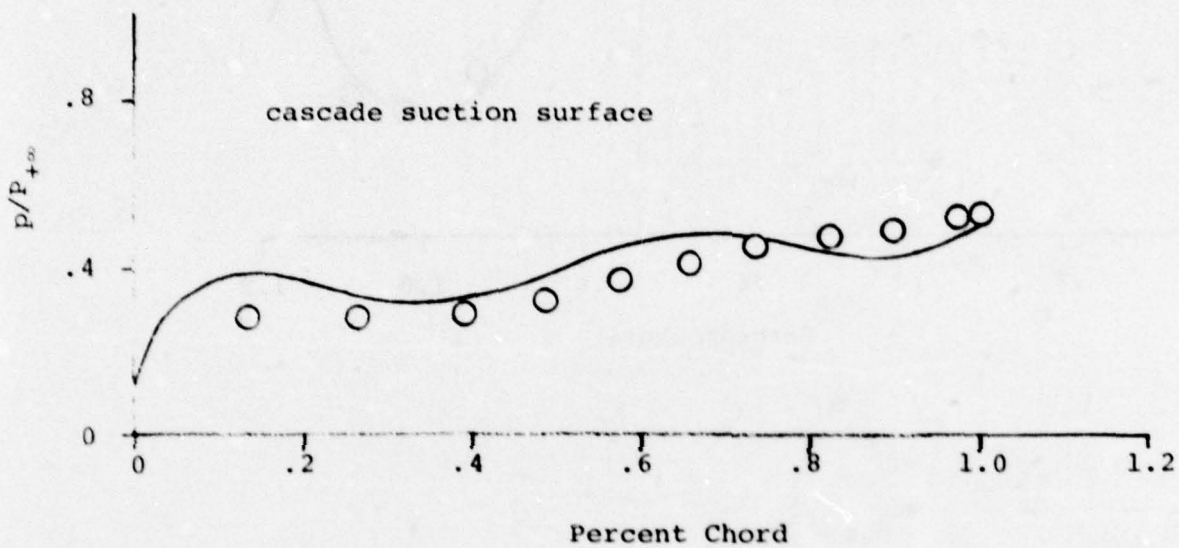
Figure 38. Comparison of numerical and experimental results on cascade main blade; $M_\infty = 1.46$, $Re_\infty = 1.36 \times 10^6$.

101
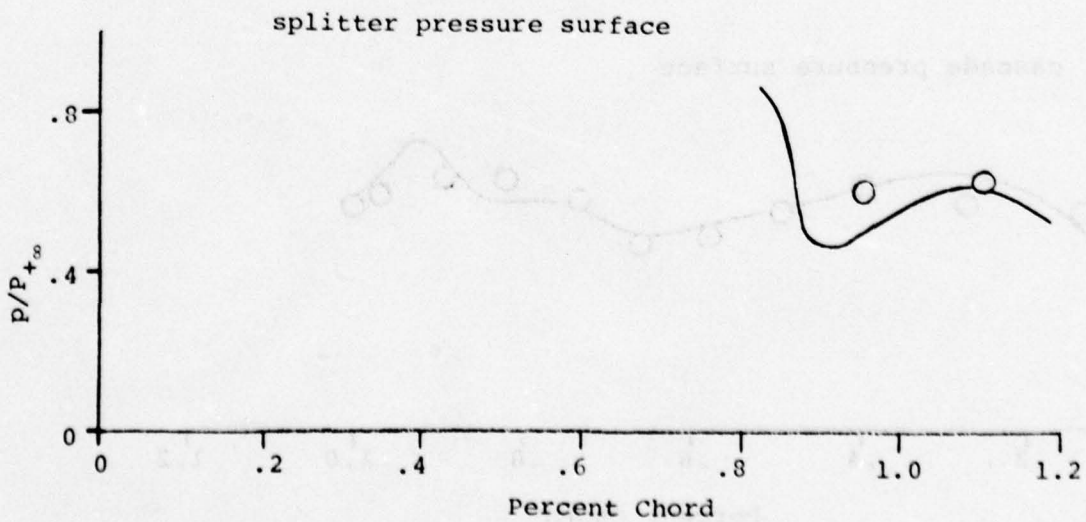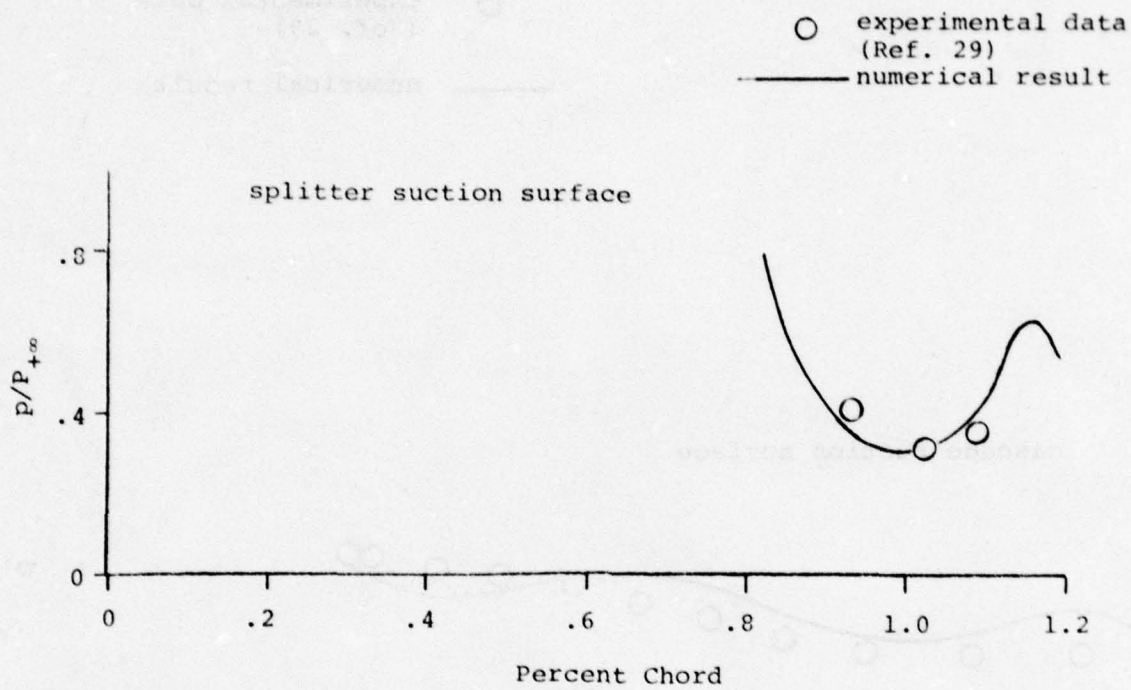
Figure 39. Comparison of numerical and experimental results on cascade splitter vane; $M_\infty = 1.46$, $Re_\infty = 1.36 \times 10^6$

102
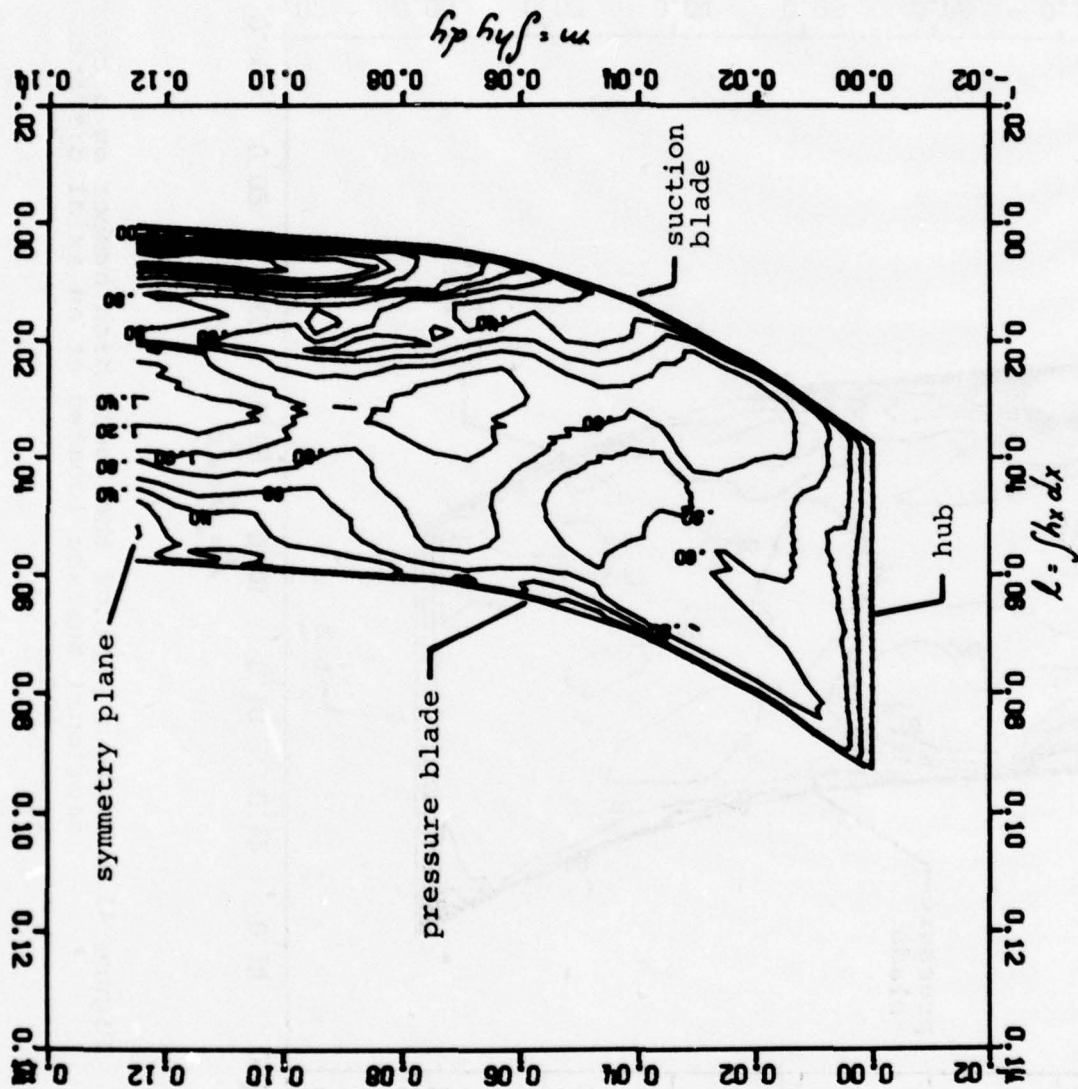
Figure 40. Contour plot of the local Mach number on a cross-sectional surface located at an axial distance ratio $\ell_r = .206$.

103
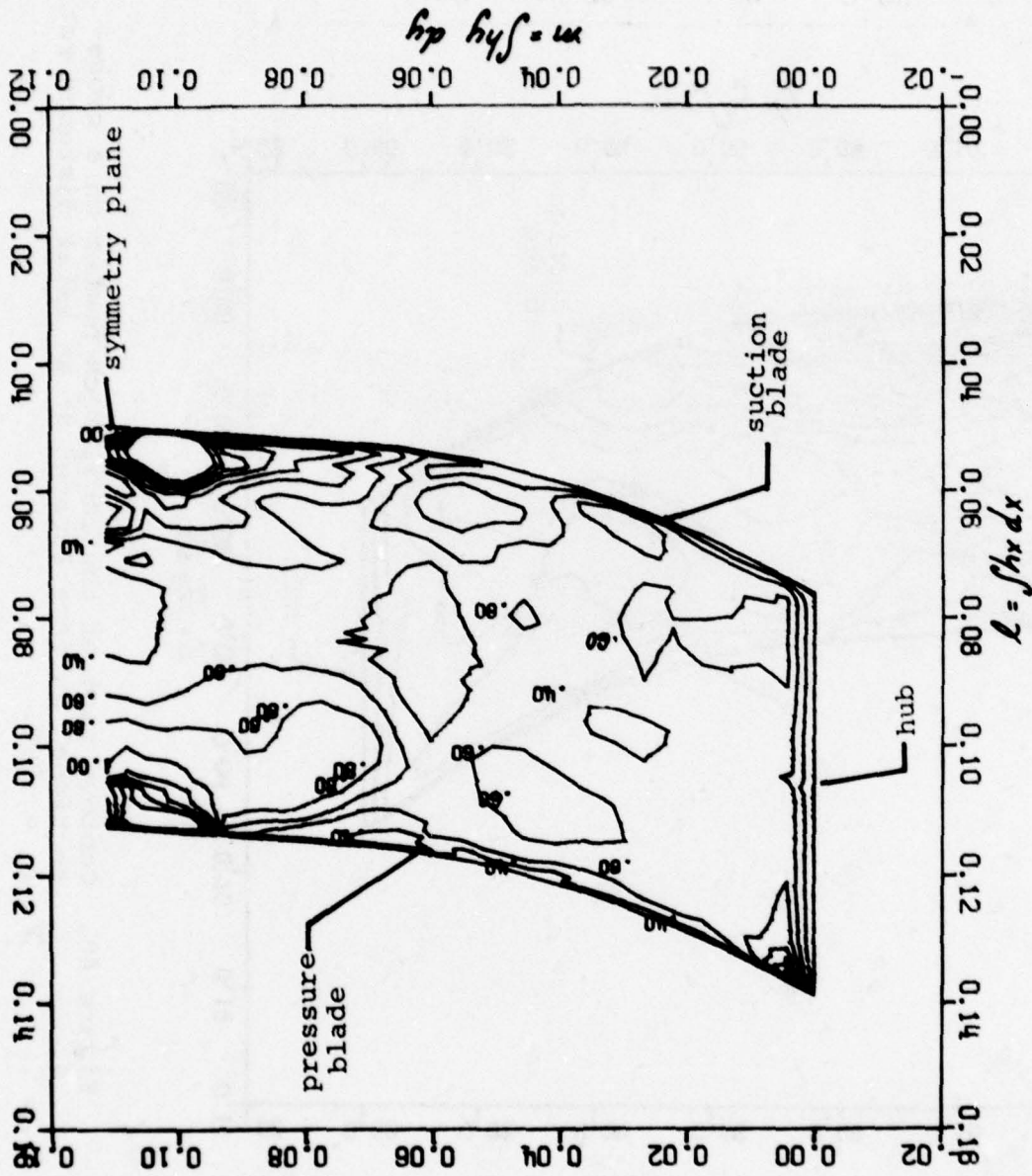
Figure 41. Contour plot of the local Mach number on a cross-sectional surface located at an axial distance ratio $\ell_r = .385$.
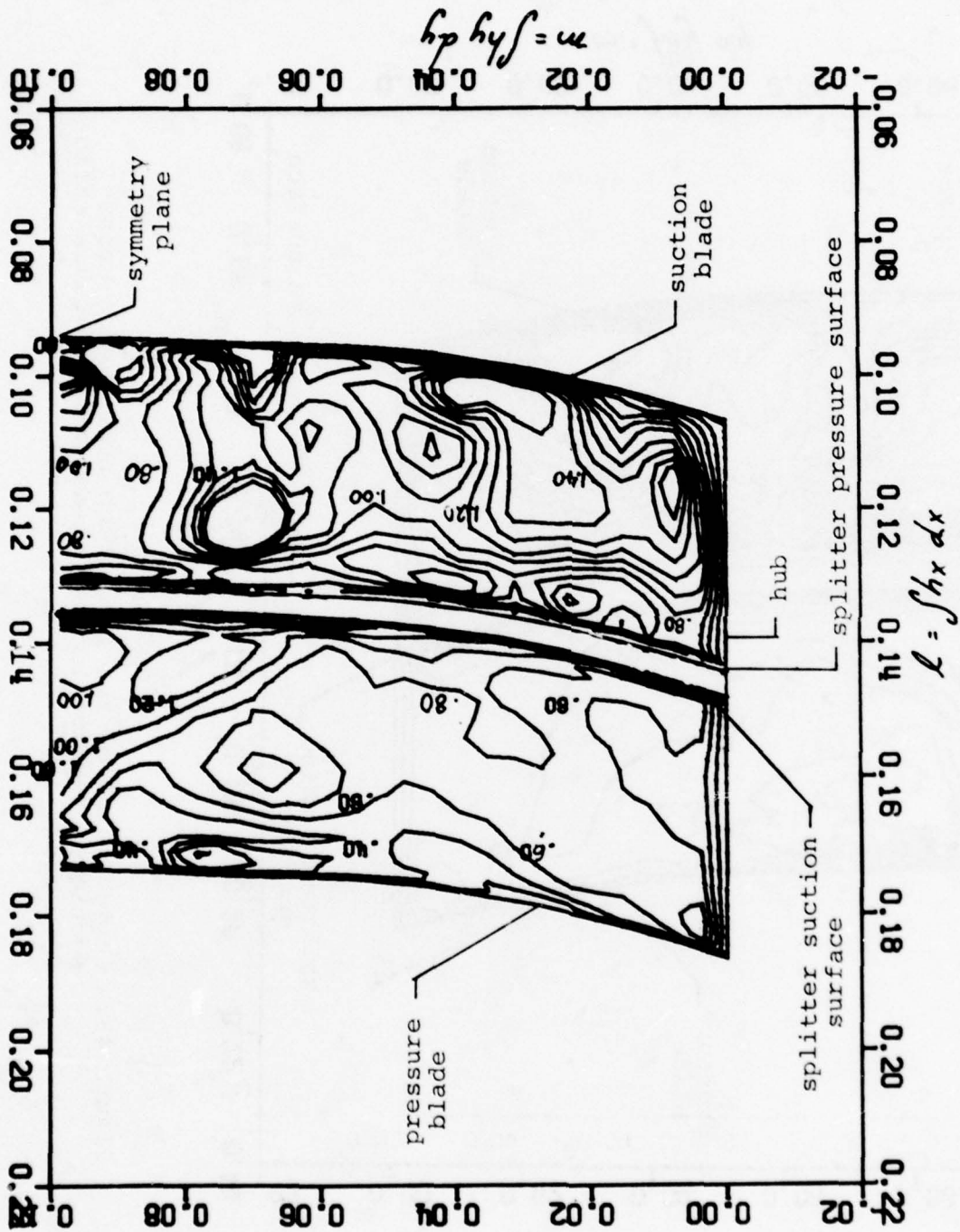
Figure 42. Contour plot of the local Mach number on a cross-sectional surface located at an axial distance ratio $\ell_r = .605$

105
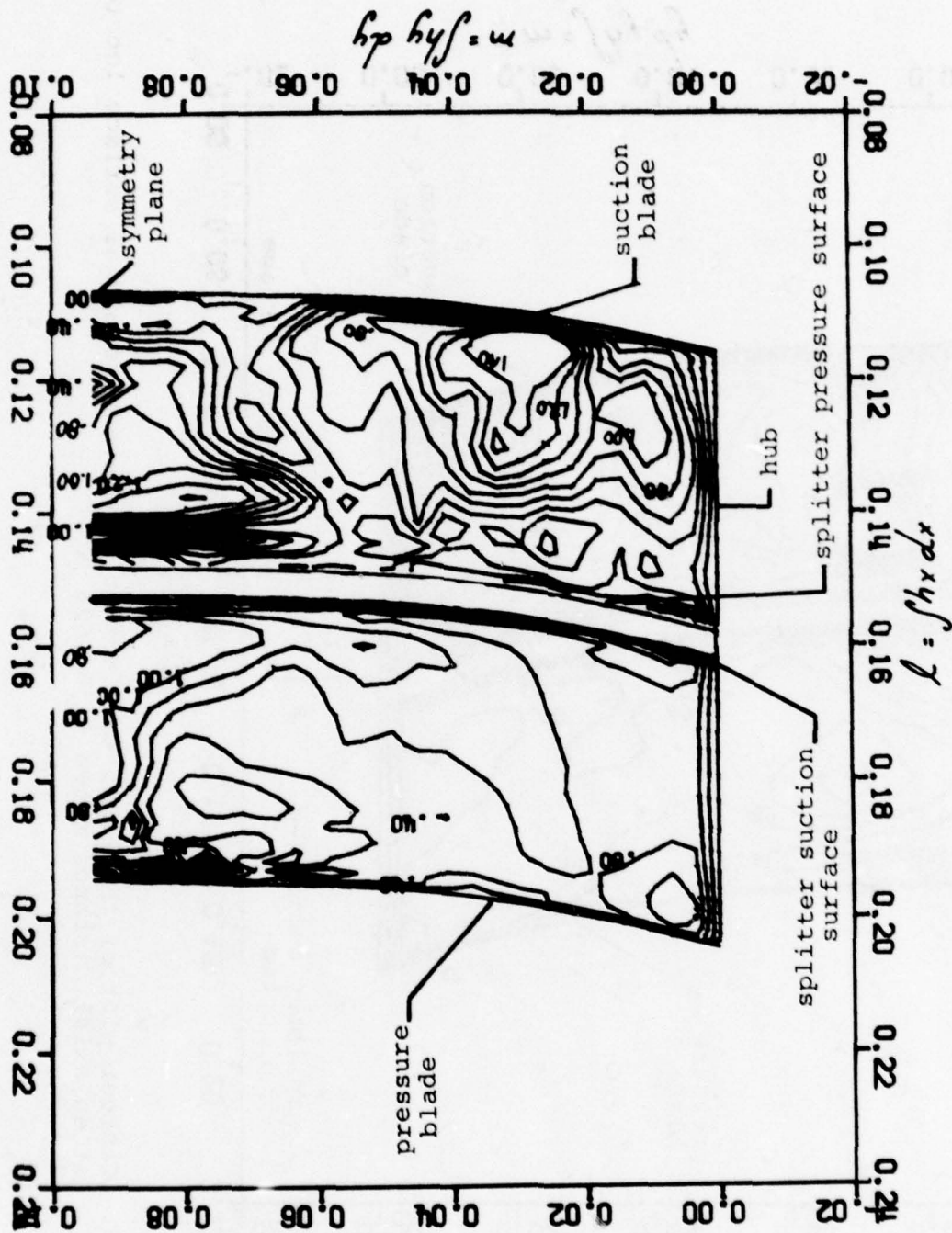
Figure 43. Contour plot of the local Mach number on a cross-sectional surface located at an axial distance ratio $\ell_r = .692$.

106
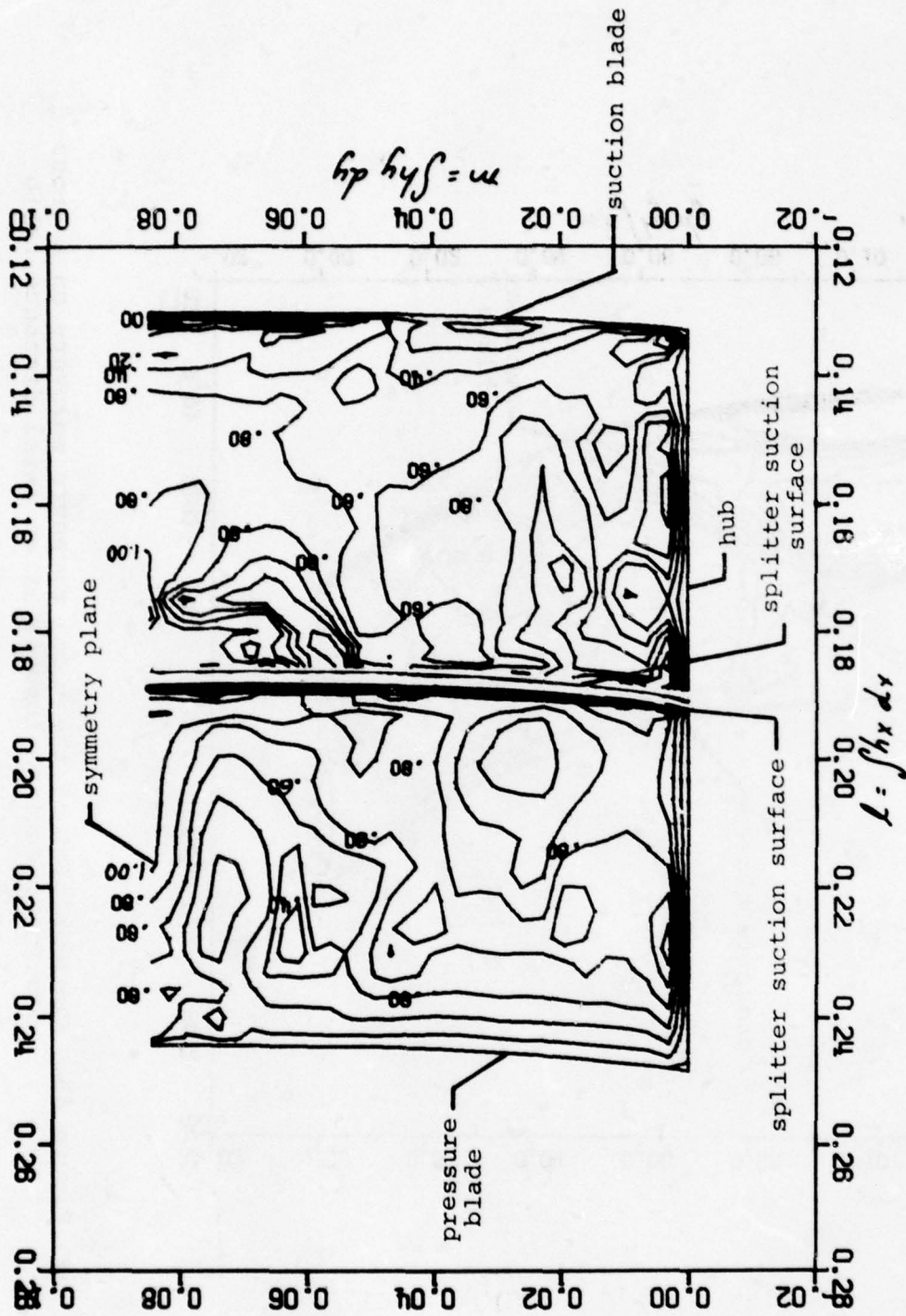
Figure 44. Contour plot of the local Mach number on a cross-
sectional surface located at an axial distance ratio
$\ell_r = .945$.

107
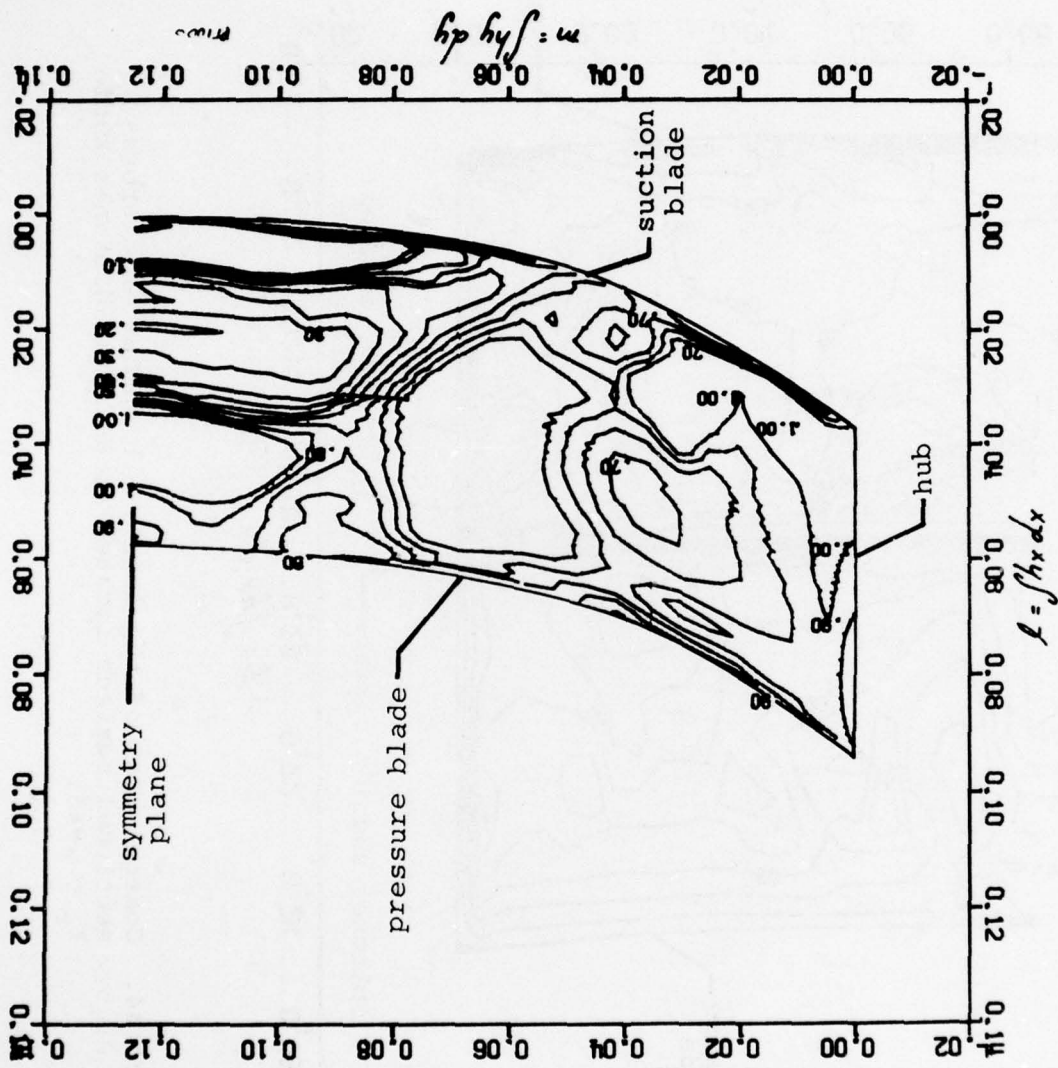
Figure 45. Contour plot of the total pressure recovery on a cross-sectional surface located at an axial distance ratio $\ell_r = .206$

108
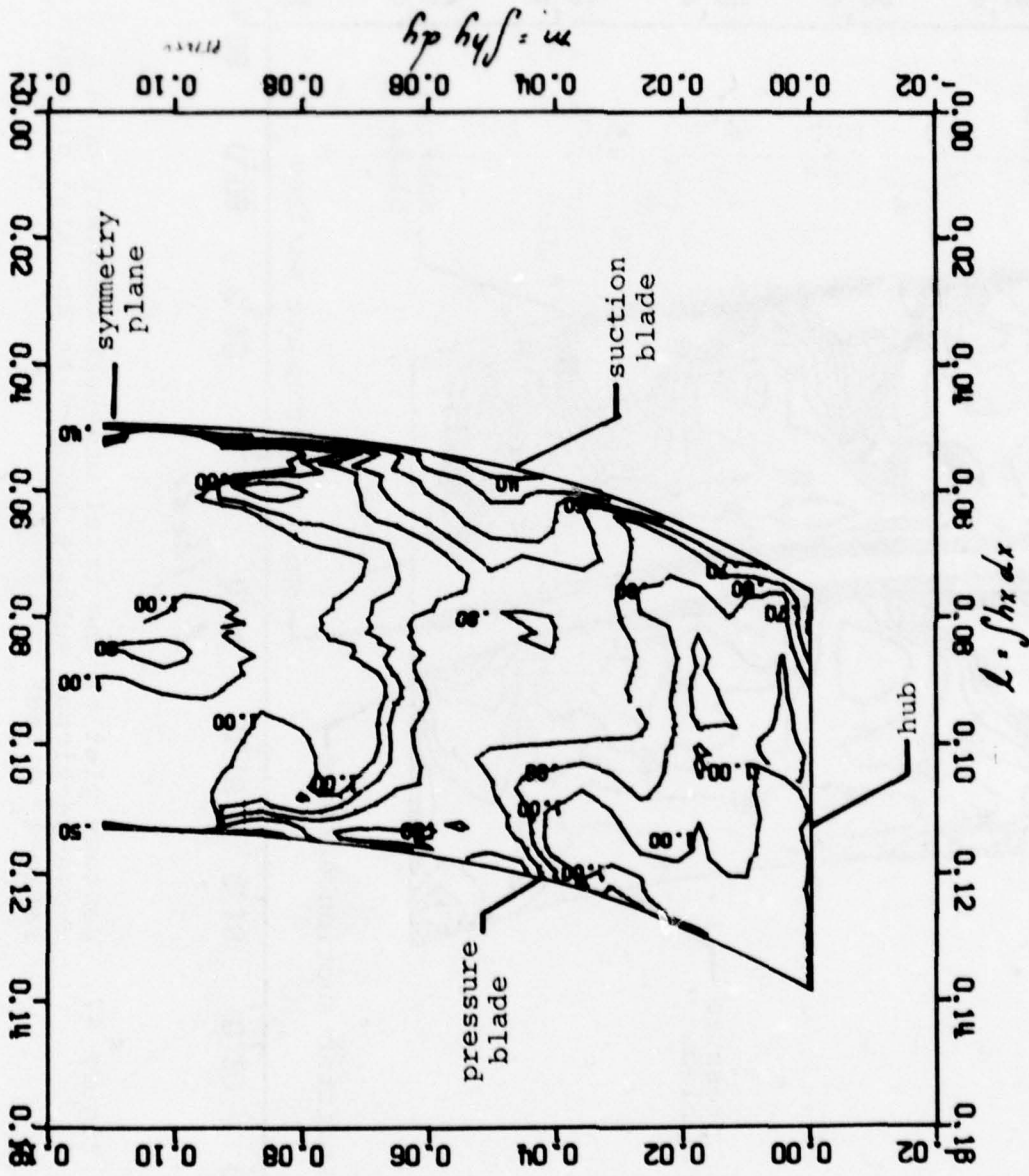
Figure 46. Contour plot of the total pressure recovery on a cross-sectional surface located at an axial distance ratio $\frac{x}{l} = .385$.
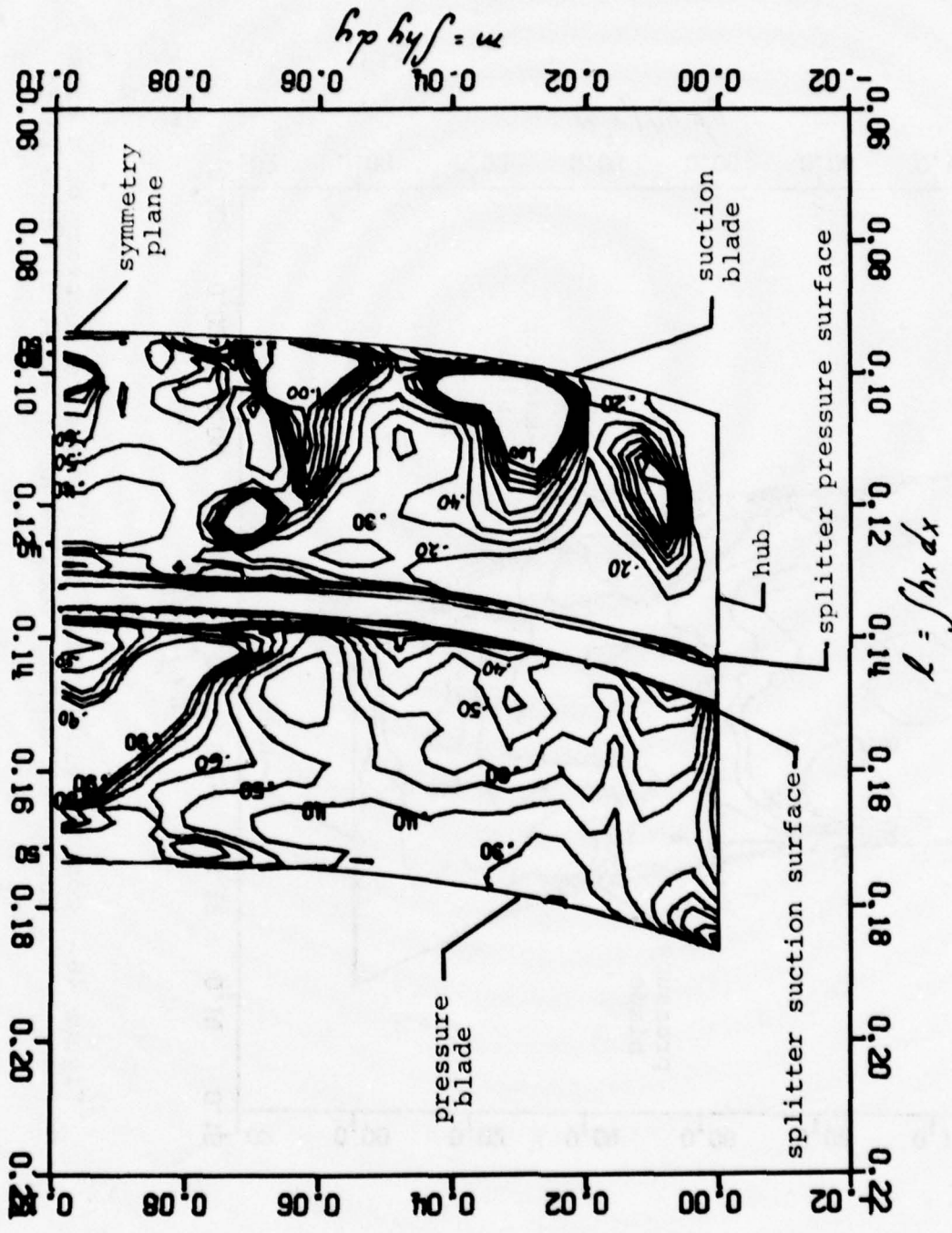
Figure 47. Contour plot of the total pressure recovery on a cross-sectional surface located at an axial distance ratio $\ell_r = .605$

110
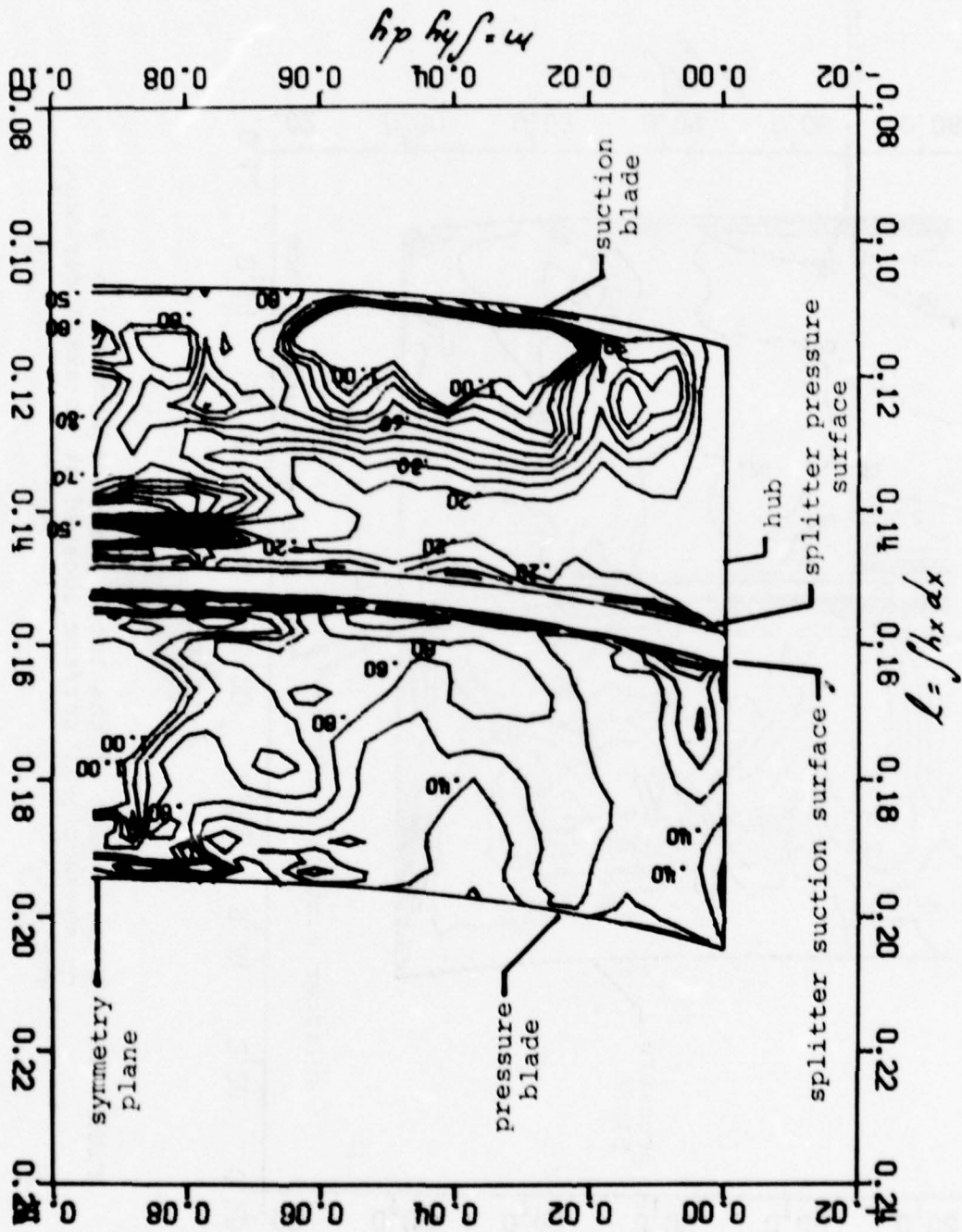
Figure 48. Contour plot of the total pressure recovery on a cross-sectional surface located at an axial distance ratio $\ell_r = .692$.

111
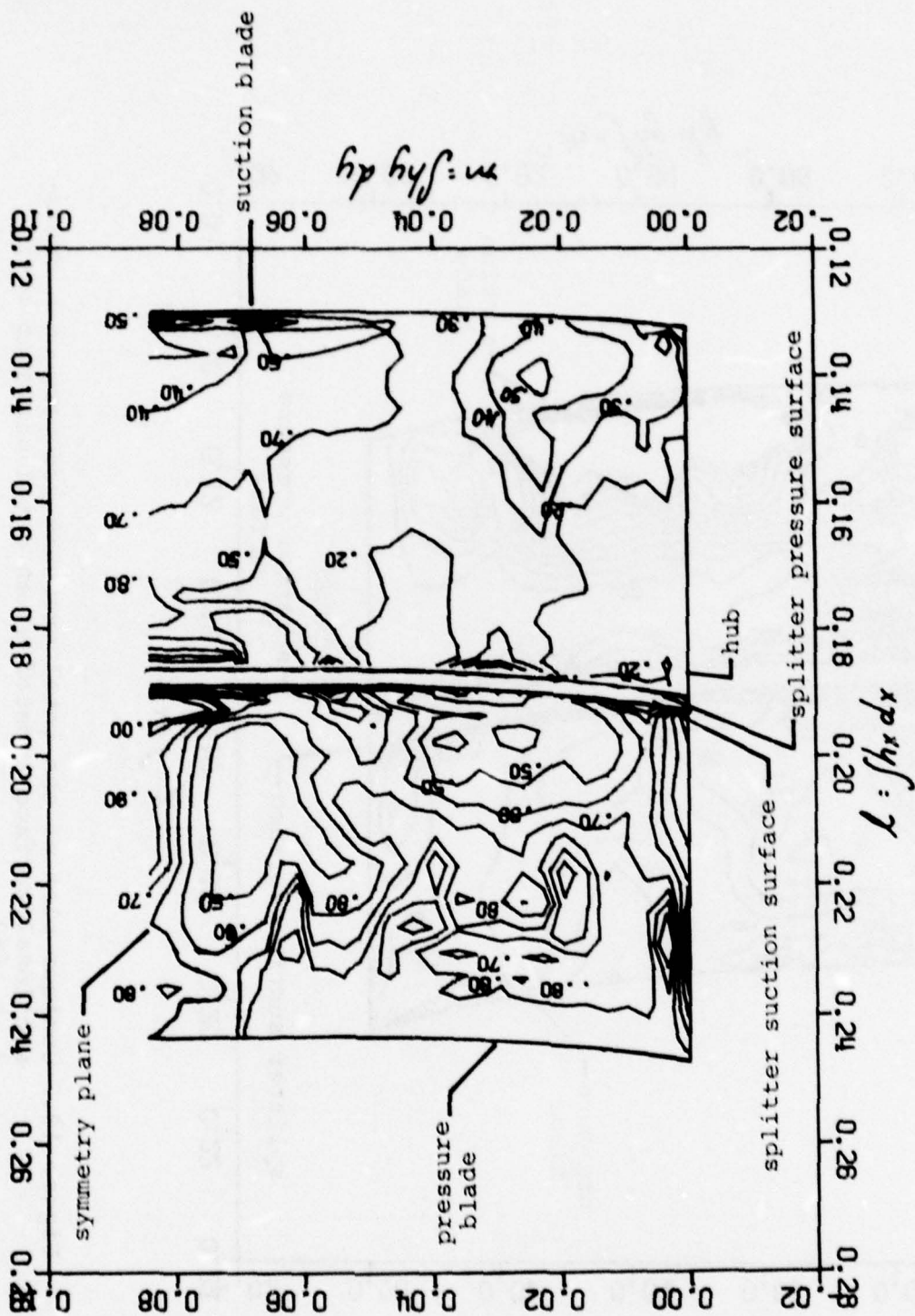
Figure 49. Contour plot of the total pressure recovery on a cross-sectional surface located at an axial distance ratio $\ell_r = .945$.

APPENDIX A

EQUATIONS OF MOTION IN ROTATING ORTHOGONAL CURVILINEAR COORDINATES

Cascade flows are confined to a channel, whose axis follows the channel geometry; hence, the equations of motion are formulated in an orthogonal, curvilinear coordinate system rotating with constant angular velocity ω^*. Let x, y, and z denote the generalized coordinates and let X_1, X_2, and X_3 denote the cartesian coordinates. The continuity, momenta, and specific internal energy equations in rotating, orthogonal, curvilinear coordinates are presented in this Appendix.

Continuity

$$div\left(\rho \underline{u}\right) = 0 \tag{A1}$$

where the divergence of the vector $\rho \underline{u}$ is defined as

$$div\left(\rho \bar{u}\right) = \frac{1}{h_x h_y h_z}\left\{\frac{d}{dx}\left(\rho u h_y h_z\right) + \frac{d}{dy}\left(\rho v h_z h_x\right) + \frac{d}{dz}\left(\rho w h_x h_y\right)\right\} \tag{A2}$$

and the velocity vector $\underline{u}$ is defined as

$$\underline{u} = u\,\underline{i} + v\,\underline{j} + w\,\underline{k} \tag{A3}$$

where: ρ is the density, (u, v, w) are the velocity components in the x, y, and z directions, respectively, ($\underline{i}$, $\underline{j}$, $\underline{k}$) are the unit vectors in the x, y, and z directions, respectively, and h_x, h_y, h_z are the transformation metrics in the x, y, and z directions, respectively.

_____

*For the case of the compressor cascade ω = 0; however, the derivation is applicable to a rotating geometry.

113

x-Momentum

$$\text{div}(\rho u \underline{u}) + \rho u / h_x \left[\frac{u}{h_x} \frac{\partial h_x}{\partial x} + \frac{v}{h_y} \frac{\partial h_x}{\partial y} + \frac{w}{h_z} \frac{\partial h_x}{\partial z} \right] - \frac{\rho}{h_x} \left[\frac{u^2}{h_x} \frac{\partial h_x}{\partial x} + \frac{v^2}{h_y} \frac{\partial h_y}{\partial x} + \frac{w^2}{h_z} \frac{\partial h_z}{\partial x} \right]$$

$$+ 2\rho\omega \left(\frac{w}{h_x} \frac{\partial X_3}{\partial y} - \frac{v}{h_z} \frac{\partial X_3}{\partial z} \right) - \frac{\rho\omega^2}{h_x} \left(\frac{\partial X_1}{\partial x} X_1 + \frac{\partial X_2}{\partial x} X_2 \right) =$$

$$\text{div}(\underline{\sigma}_x) + \frac{\tau_{xy}}{h_x h_y} \frac{\partial h_x}{\partial x} + \frac{\tau_{zx}}{h_x h_z} \frac{\partial h_x}{\partial z} - \frac{\sigma_{yy}}{h_x h_y} \frac{\partial h_y}{\partial x} - \frac{\sigma_{zz}}{h_x h_z} \frac{\partial h_z}{\partial x} \qquad (A4)$$

where the force per unit area in the x-direction is defined as

$$\underline{\sigma}_x = \sigma_{xx} \underline{i} + \tau_{yx} \underline{j} + \tau_{zx} \underline{k}$$

and ($\sigma_{xx}, \tau_{yx}, \tau_{zx}$) are the stress tensor components asso-
ciated with the x-direction. The term div ($\rho u \underline{u}$) is obtained by
replacing the components ($\rho u, \rho v, \rho w$) in Equation (A2) by
($\rho u u, \rho v u, \rho w u$). Similarly the term div($\underline{\sigma}_x$) is obtained from
Equation (A2) by replacing the components ($\rho u, \rho v, \rho w$) by
($\sigma_{xx}, \tau_{yx}, \tau_{zx}$).

y-Momentum

$$\text{div}(\rho v \underline{u}) + \frac{\rho v}{h_y} \left[\frac{u}{h_x} \frac{\partial h_y}{\partial x} + \frac{v}{h_y} \frac{\partial h_y}{\partial y} + \frac{w}{h_z} \frac{\partial h_y}{\partial z} \right] - \frac{\rho}{h_y} \left[\frac{u^2}{h_x} \frac{\partial h_x}{\partial y} + \frac{v^2}{h_y} \frac{\partial h_y}{\partial y} + \frac{w^2}{h_z} \frac{\partial h_z}{\partial y} \right]$$

$$+ 2\omega\rho \left(\frac{u}{h_z} \frac{\partial X_3}{\partial z} - \frac{w}{h_x} \frac{\partial X_3}{\partial x} \right) - \frac{\rho\omega^2}{h_y} \left(\frac{\partial X_1}{\partial y} X_1 + \frac{\partial X_2}{\partial y} X_2 \right) =$$

$$\text{div}(\underline{\sigma}_y) + \frac{\tau_{yz}}{h_y h_z} \frac{\partial h_y}{\partial z} + \frac{\tau_{xx}}{h_x h_y} \frac{\partial h_y}{\partial x} - \frac{\sigma_{zz}}{h_y h_z} \frac{\partial h_z}{\partial y} - \frac{\sigma_{xx}}{h_x h_y} \frac{\partial h_x}{\partial y} \qquad (A5)$$

where the force per unit area in the y-direction is defined as

$$\underline{\sigma}_y = \tau_{xy} \underline{i} + \sigma_{yy} \underline{j} + \tau_{zy} \underline{k}$$

and ($\tau_{xy}, \sigma_{yy}, \tau_{zy}$) are the stress tensor components associated with
the y-direction.

114

z-Momentum

$$\text{div}(\rho W \underline{U}) + \frac{\rho W}{h_z}\left[\frac{U}{h_z}\frac{\partial h_z}{\partial x} + \frac{V}{h_y}\frac{\partial h_z}{\partial y} + \frac{W}{h_z}\frac{\partial h_z}{\partial z}\right] - \frac{\rho}{h_z}\left[\frac{U^2}{h_x}\frac{\partial h_x}{\partial z} + \frac{V^2}{h_y}\frac{\partial h_y}{\partial z} + \frac{W^2}{h_z}\frac{\partial h_z}{\partial z}\right]$$

$$+ 2\rho\omega\left(\frac{V}{h_x}\frac{\partial X_3}{\partial x} - \frac{U}{h_y}\frac{\partial X_3}{\partial y}\right) - \frac{\rho\omega^2}{h_z}\left(\frac{\partial X_1}{\partial z}X_1 + \frac{\partial X_2}{\partial z}X_2\right) =$$

$$\text{div}(\underline{\sigma}_z) + \frac{\tau_{zx}}{h_x h_z}\frac{\partial h_z}{\partial x} + \frac{\tau_{yz}}{h_z h_y}\frac{\partial h_z}{\partial y} - \frac{\sigma_{xx}}{h_x h_z}\frac{\partial h_x}{\partial z} - \frac{\sigma_{yy}}{h_z h_y}\frac{\partial h_y}{\partial z} \qquad (A6)$$

where the force per unit area in the z-direction is defined as

$$\underline{\sigma}_z = \tau_{xz}\,\underline{i} + \tau_{yz}\,\underline{j} + \sigma_{zz}\,\underline{k}$$

and ($\tau_{xz}, \tau_{yz}, \sigma_{zz}$) are the stress components associated with the z-direction.

Internal Energy Equation

$$\text{div}(\rho E \underline{U}) = \sigma_{xx}\left[\frac{1}{h_x}\frac{\partial U}{\partial x} + \frac{V}{h_x h_y}\frac{\partial h_x}{\partial y} + \frac{W}{h_z h_x}\frac{\partial h_x}{\partial z}\right] + \sigma_{yy}\left[\frac{1}{h_y}\frac{\partial V}{\partial y} + \frac{W}{h_y h_z}\frac{\partial h_y}{\partial z} + \frac{U}{h_x h_y}\frac{\partial h_y}{\partial x}\right]$$

$$+ \sigma_{zz}\left[\frac{1}{h_z}\frac{\partial W}{\partial z} + \frac{U}{h_z h_x}\frac{\partial h_z}{\partial x} + \frac{V}{h_y h_z}\frac{\partial h_z}{\partial y}\right] + \tau_{yz}\left[\left(\frac{h_z}{h_y}\right)\frac{\partial}{\partial y}\left(\frac{W}{h_z}\right) + \left(\frac{h_y}{h_z}\right)\frac{\partial}{\partial z}\left(\frac{V}{h_y}\right)\right]$$

$$+ \tau_{zx}\left[\left(\frac{h_x}{h_z}\right)\frac{\partial}{\partial z}\left(\frac{U}{h_x}\right) + \left(\frac{h_z}{h_x}\right)\frac{\partial}{\partial x}\left(\frac{W}{h_z}\right)\right] + \tau_{xy}\left[\left(\frac{h_y}{h_x}\right)\frac{\partial}{\partial x}\left(\frac{V}{h_y}\right) + \left(\frac{h_x}{h_y}\right)\frac{\partial}{\partial y}\left(\frac{U}{h_x}\right)\right] \qquad (A7)$$

The Stokesian stress tensor components for laminar flow in orthogonal, curvilinear coordinates are presented below:

115

Normal Stresses

$$\sigma_{xx} = -p + 2\mu \left(\dot{e}_{xx} - \tfrac{1}{3} \, div(\underline{u}) \right) \tag{A8}$$

$$\sigma_{yy} = -p + 2\mu \left(\dot{e}_{yy} - \tfrac{1}{3} \, div(\underline{u}) \right) \tag{A9}$$

$$\sigma_{zz} = -p + 2\mu \left(\dot{e}_{zz} - \tfrac{1}{3} \, div(\underline{u}) \right) \tag{A10}$$

where μ is the temperature dependent molecular viscosity and the rate of strains $\dot{e}_{xx}$, $\dot{e}_{yy}$, $\dot{e}_{zz}$ are defined as follows:

$$\dot{e}_{xx} = \frac{1}{h_x}\frac{\partial u}{\partial x} + \frac{v}{h_x h_y}\frac{\partial h_x}{\partial y} + \frac{w}{h_z h_x}\frac{\partial h_x}{\partial z} \tag{A11}$$

$$\dot{e}_{yy} = \frac{1}{h_y}\frac{\partial v}{\partial y} + \frac{w}{h_y h_z}\frac{\partial h_y}{\partial z} + \frac{u}{h_x h_y}\frac{\partial h_y}{\partial x} \tag{A12}$$

$$\dot{e}_{zz} = \frac{1}{h_z}\frac{\partial w}{\partial z} + \frac{u}{h_z h_x}\frac{\partial h_z}{\partial x} + \frac{v}{h_y h_z}\frac{\partial h_z}{\partial y} \tag{A13}$$

Shear Stresses

$$\tau_{yz} = \tau_{zy} = \mu \, \dot{e}_{yz} \tag{A14}$$

$$\tau_{zx} = \tau_{xz} = \mu \, \dot{e}_{zx} \tag{A15}$$

$$\tau_{xy} = \tau_{yx} = \mu \, \dot{e}_{xy} \tag{A16}$$

where the rate of strains $\dot{e}_{yz}$, $\dot{e}_{zx}$ and $\dot{e}_{xy}$ are defined as follows:

$$\dot{e}_{yz} = \frac{h_z}{h_y} \frac{d}{dy}\left(\frac{W}{h_z}\right) + \frac{h_y}{h_z} \frac{d}{dz}\left(\frac{V}{h_y}\right)$$

(A17)

$$\dot{e}_{zx} = \frac{h_x}{h_z} \frac{d}{dz}\left(\frac{U}{h_x}\right) + \frac{h_z}{h_x} \frac{d}{dx}\left(\frac{W}{h_z}\right)$$

(A18)

$$\dot{e}_{xy} = \frac{h_y}{h_x} \frac{d}{dx}\left(\frac{V}{h_y}\right) + \frac{h_x}{h_y} \frac{d}{dy}\left(\frac{U}{h_x}\right)$$

(A19)

117

APPENDIX B

DERIVATION OF THE INTEGRAL CONTINUITY EQUATION

In this section the integral continuity equation solved on the (x,y) blade-to-blade surface is derived. This derivation is presented to illustrate the actual elliptic source terms and the parabolic terms of the equations of motion. The equations of motion in rotating, orthogonal, curvilinear, Eulerian coordinates x, y and z are presented in Appendix A.

The steady three-dimensional equations of Appendix A, in Eulerian coordinates x, y, z are transformed to (x,y,t) space according to the following relations :

$$ z = U_z t \quad , \quad \frac{d}{dz} = \frac{1}{U_z} \frac{d}{dt} \quad , \quad W = U_z + w' \tag{B1} $$

where t is a time-like-variable, U_z is the velocity of the blade-to-blade surface, W is the velocity component in the z-direction, and w' is the perturbation velocity in the z-direction. Equations (B1) represent a mathematically convenient transformation and lead to a compact set of integral equations; however, they are somewhat non-physical in that the variable t may no longer be time-like, having the units z/U_z .

The conservation of mass for steady motion relative to the rotating, curvilinear coordinates (x,y,z) is (Appendix A) as follows:

$$ \frac{d}{dz}\left(\rho w h_x h_y \right) + \frac{d}{dx}\left(\rho u h_y h_z \right) + \frac{d}{dy}\left(\rho v h_x h_z \right) = 0 \tag{B2} $$

118

where ρ is the density, u the x-velocity component, v the y-velocity component, and h_x, h_y, h_z are the transformation metrics.

According to Equations (B1) the continuity equation becomes:

$$\frac{d}{dt}(\rho h_x h_y) + \frac{d}{dx}(\rho u h_y h_z) + \frac{d}{dy}(\rho v h_x h_z) = -\frac{1}{U_z}\frac{d}{dt}(\rho w' h_x h_y) \tag{B3}$$

The left-hand side of Equation (B3) closely resembles the continuity equation for unsteady flow in the (x,y) plane. The transformation metrics, h_x, h_y, h_z on the left-hand side account for the fact that the flow is not planar but occurs on a curved surface. The term on the right-hand side of Equation (B3) represents a source term which accounts for the variation of axial velocity w from the constant reference velocity. This term must be considered known in the iteration process and is evaluated from the previous iterate in each successive iteration.

Equation (B3) is formulated in the Eulerian coordinates (x,y,t); however, in the planar calculational process the trace of the boundary of the cascade channel in the cross-sectional surface must distort with time. Hence, we are really interested in the continuity equation in a generalized coordinate system ξ , η , τ , where :

$$t = \tau \tag{B4}$$

$$x = f(\xi, \eta, \tau) \tag{B5}$$

$$y = g(\xi, \eta, \tau) \tag{B6}$$

119

and $f(\xi, \eta, 0) = \xi$, $g(\xi, \eta, 0) = \eta$, where $f_\xi = \left(\frac{\partial f}{\partial \xi}\right)_{\tau=0} = 1$, $g_\eta = \left(\frac{\partial g}{\partial \eta}\right)_{\tau=0} = 1$.

We now differentiate (B4) with respect to t, x, and y, respectively-ly, with the results

$$
\left.
\begin{aligned}
\frac{\partial \tau}{\partial t} &= 1 \\[8pt]
\frac{\partial \tau}{\partial x} &= 0 \\[8pt]
\frac{\partial \tau}{\partial y} &= 0
\end{aligned}
\right\}
\tag{B7}
$$

Performing the same differentiation of Equations (B5) and (B6) yields (after much manipulation)

$$
\left.
\begin{aligned}
\frac{\partial \xi}{\partial \tau} &= \frac{f_\eta g_\tau - g_\eta f_\tau}{[f_\xi g_\eta - g_\xi f_\eta]} \\[8pt]
\frac{\partial \xi}{\partial x} &= \frac{g_\eta}{[f_\xi g_\eta - g_\xi f_\eta]} \\[8pt]
\frac{\partial \xi}{\partial y} &= \frac{-f_\eta}{[f_\xi g_\eta - g_\xi f_\eta]}
\end{aligned}
\right\}
\tag{B8}
$$

$$
\left.
\begin{aligned}
\frac{\partial \eta}{\partial \tau} &= \frac{f_\tau g_\xi - f_\xi g_\tau}{[f_\xi g_\eta - g_\xi f_\eta]} \\[8pt]
\frac{\partial \eta}{\partial x} &= \frac{-g_\xi}{[f_\xi g_\eta - g_\xi f_\eta]} \\[8pt]
\frac{\partial \eta}{\partial y} &= \frac{f_\xi}{[f_\xi g_\eta - g_\xi f_\eta]}
\end{aligned}
\right\}
\tag{B9}
$$

120

Consider the function $G(\xi, \eta, \tau)$ whose derivatives are

$$\frac{\partial G}{\partial t} = G_\xi \frac{\partial \xi}{\partial t} + G_\eta \frac{\partial \eta}{\partial t} + G_\tau \frac{\partial \tau}{\partial t} =$$

$$\frac{G_\xi(f_\eta g_\tau - g_\eta f_\tau) + G_\eta(f_\tau g_\xi - f_\xi g_\tau) + G_\tau(f_\xi g_\eta - g_\xi f_\eta)}{(f_\xi g_\eta - g_\xi f_\eta)} \tag{B11}$$

$$\frac{\partial G}{\partial x} = G_\xi \frac{\partial \xi}{\partial x} + G_\eta \frac{\partial \eta}{\partial x} + G_\tau \frac{\partial \tau}{\partial x} = \frac{G_\xi g_\eta - G_\eta g_\xi}{[f_\xi g_\eta - g_\xi f_\eta]} \tag{B12}$$

$$\frac{\partial G}{\partial y} = G_\xi \frac{\partial \xi}{\partial y} + G_\eta \frac{\partial \eta}{\partial y} + G_\tau \frac{\partial \tau}{\partial y} = \frac{-G_\xi f_\eta + G_\eta f_\xi}{[f_\xi g_\eta - g_\xi f_\eta]} \tag{B13}$$

where use of Equations (B6) - (B9) produced Equations (B11), (B12), and (B13).

Based on Equations (B11), (B12), and (B13), the continuity Equation (B3) transforms to the generalized coordinates (ξ, η, τ) as follows:

$$\frac{\partial}{\partial \tau}(\rho h_x h_y J^{-1}) + \left[(\rho h_y(uh_\tau - S_x h_x)_x) + (\rho h_x(vh_\tau - S_y h_y)_y) \right] J^{-1}$$

$$- \frac{1}{U_\tau}\left[(\rho w' h_y h_x S_x)_x + (\rho w' h_x h_y S_y)_y \right] J^{-1} = -\frac{1}{U_\tau}\frac{\partial}{\partial \tau}(\rho w' h_x h_y J^{-1}) \tag{B14}$$

where $(\ )_x$ and $(\ )_y$ define differentiation with respect to x and y, respectively, and the grid velocity components S_x and S_y are de-

121

fined as

$$S_x = \frac{dx}{dt} = f_\tau$$
$$S_y = \frac{dy}{dt} = g_\tau$$

(B15)

The symbol J represents the Jacobian of the transformation, i.e.,

$$J = \left| \frac{\partial(\xi, \eta, \tau)}{\partial(x, y, t)} \right| = \frac{1}{f_\xi g_\eta - g_\xi f_\eta}$$

(B16)

where:

$$dx\, dy = J^{-1} d\xi\, d\eta$$

(B17)

Multiplying Equation (B14) by the area increment $d\xi\, d\eta$ and integrating yields:

$$\frac{d}{dt} \int_A \rho h_x h_y dA + \int_C \rho(\underline{q} - \underline{q_s}) \cdot \underline{\hat{n}}\, dC - \frac{1}{U_\xi} \int_C \rho w' \underline{q_s} \cdot \underline{\hat{n}}\, dC = -\frac{1}{U_\xi} \frac{d}{dt} \int_A \rho w' h_x h_y dA$$

(B18)

where dA = dx dy, A corresponds to the area in the x,y plane contained within the region bounded by the closed curve C, $\underline{n}$ is the unit normal to the curve C, $\underline{q}$ is the particle velocity vector in the (x,y) plane as defined by Equation (C3), and $\underline{q}_s$ is the coordinate velocity vector in the (x,y) plane as defined by Equation (C4). In the integration process use was made of Equation (B17) to convert integrals in $d\xi\, d\eta$ to integrals in dxdy. Furthermore, Leibniz's rule was used to permute differentiation and integration and Gauss's theorem was used to convert area integrals to line integrals in the (x,y) plane.

122

APPENDIX C

MOMENTUM AND SPECIFIC INTERNAL ENERGY RELATIONS
IN GENERALIZED COORDINATES

In this appendix the momentum and specific internal energy relations are presented in generalized coordinates.

x-direction momentum

$$\frac{d}{dt}\int_A \rho u\, h_x h_y\, dA + \int_C \rho u\, (\underline{q} - \underline{q}_s)\cdot\hat{n}\, dC + \int_A h_x h_y h_z A_x\, dA$$

$$-\frac{1}{U_z}\int_C \rho u w'\, \underline{q}_s\cdot\hat{n}\, dC = -\frac{1}{U_z}\frac{d}{dt}\int_A \rho u w' h_x h_y\, dA + \frac{1}{U_z}\frac{d}{dt}\int_A \tau_{zx} h_x h_y\, dA$$

$$-\frac{1}{U_z}\int_C \tau_{zx}\, \underline{q}_s\cdot\hat{n}\, dC + \int_A h_x h_y \Pi_x\, dA + \int_C \underline{\sigma}_{p_x}\cdot\hat{n}\, dC \qquad (C1)$$

where:

$$A_x = \frac{\rho u}{h_x}\left\{\frac{u}{h_x}\frac{dh_x}{dx} + \frac{v}{h_y}\frac{dh_x}{dy} + \frac{w}{h_z}\frac{dh_x}{dz}\right\} - \frac{\rho}{h_x}\left\{\frac{u^2}{h_x}\frac{dh_x}{dx} + \frac{v^2}{h_y}\frac{dh_y}{dx} + \frac{w^2}{h_z}\frac{dh_z}{dx}\right\}$$

$$+ 2\rho\omega\left(\frac{w}{h_y}\frac{dX_3}{dy} - \frac{v}{h_z}\frac{dX_3}{dz}\right) - \frac{\rho\omega^2}{h_x}\left(\frac{dX_1}{dx}X_1 + \frac{dX_2}{dx}X_2\right) \qquad (C2)$$

$$\underline{q} = u\, h_y h_z\, \underline{i} + v\, h_x h_z\, \underline{j} \qquad (C3)$$

$$\underline{q}_s = S_x h_x h_y\, \underline{i} + S_y h_y h_x\, \underline{j} \qquad (C4)$$

$$\Pi_x = \frac{\tau_{xy}}{h_x h_y}\frac{dh_x}{dy} + \frac{\tau_{zx}}{h_x h_z}\frac{dh_x}{dz} - \frac{\sigma_{yy}}{h_x h_y}\frac{dh_y}{dx} - \frac{\sigma_{zz}}{h_x h_z}\frac{dh_z}{dx} \qquad (C5)$$

123

$$\vec{\sigma}_{Px} = \sigma_{xx} h_y h_z \underline{i} + \tau_{yx} h_x h_z \underline{j} \tag{C6}$$

and A is the area in the (x,y) plane, C a closed curve in the (x,y) plane, $\hat{\underline{n}}$ is a unit normal to the curve C, (σ_{xx}, τ_{yx}, τ_{zx}) are the stress tensor components associated with the x-direction, σ_{yy} is the normal stress in the y-direction, and σ_{zz} is the normal stress in the z-direction.

y-direction momentum

$$\frac{d}{dt}\int_A \rho v \, h_x h_y \, dA + \int_C \rho v \,(\underline{q} - \underline{q}_s) \cdot \underline{\hat{n}} \, dC + \int_A h_x h_y h_z A_y \, dA$$

$$- \frac{1}{U_z}\int_C \rho v w' \underline{q}_s \cdot \hat{n} \, dC = -\frac{1}{U_z}\frac{d}{dt}\int_A \rho v w' h_x h_y \, dA + \frac{1}{U_z}\frac{d}{dt}\int_A h_x h_y \, \tau_{zy} \, dA$$

$$- \frac{1}{U_z}\int_C \tau_{zy} \, \underline{q}_s \cdot \hat{n} \, dC + \int_A h_x h_y h_z \, \pi_y \, dA + \int_C \vec{\sigma}_{Py} \cdot \hat{\underline{n}} \, dC \tag{C7}$$

where:

$$A_y = \frac{\rho w}{h_z}\left\{ \frac{u}{h_z}\frac{dh_y}{dx} + \frac{v}{h_y}\frac{dh_y}{dy} + \frac{w}{h_z}\frac{dh_z}{dz} \right\} - \frac{\rho}{h_z}\left\{ \frac{u^2}{h_x}\frac{dh_x}{dy} + \frac{v^2}{h_y}\frac{dh_y}{dy} + \frac{w}{h_z}\frac{dh_z}{dy} \right\}$$

$$+ 2\rho\omega\left(\frac{u}{h_z}\frac{dX_3}{dz} - \frac{w}{h_x}\frac{dX_3}{dx} \right) - \frac{\rho\omega^2}{h_y}\left(X_1\frac{dX_1}{dy} + X_2\frac{dX_2}{dy} \right) \tag{C8}$$

$$\pi_y = \frac{\tau_{yz}}{h_y h_z}\frac{dh_y}{dz} + \frac{\tau_{xy}}{h_x h_y}\frac{dh_y}{dx} - \frac{\sigma_{zz}}{h_y h_z}\frac{dh_z}{dy} - \frac{\sigma_{xx}}{h_x h_y}\frac{dh_x}{dy} \tag{C9}$$

$$\vec{\sigma}_{Py} = h_y h_z \, \tau_{xy} \, \underline{i} + h_x h_z \, \sigma_{yy} \, \underline{j} \tag{C10}$$

and τ_{yz} is the shear stress component associated with the (y,z) directions.

124

z-direction momentum

$$\frac{d}{dt}\int_A \rho w \, h_x h_y \, dA + \int_C \rho w (\underline{q} - \underline{q}_s) \cdot \hat{\underline{n}} \, dC + \int_A h_x h_y \, h_z \, dA - \frac{1}{U_z}\int \rho w w' \underline{q}_s \cdot \hat{\underline{n}} \, dC$$

$$= -\frac{1}{U_z}\frac{d}{dt}\int_A \rho w w' h_x h_y \, dA + \frac{1}{U_z}\frac{d}{dt}\int_A h_x h_y \, \sigma_{zt} \, dA - \frac{1}{U_z}\int_C \sigma_{zt} \, \underline{q}_s \cdot \hat{\underline{n}} \, dC$$

$$+ \int_A h_x \, h_y \, h_z \, \pi_z \, dA + \int_C \sigma_{P_z} \cdot \hat{\underline{n}} \, dC \qquad \text{(C11)}$$

where:

$$A_z = \frac{\rho w}{h_z}\left\{\frac{u}{h_z}\frac{dh_z}{dx} + \frac{v}{h_y}\frac{dh_z}{dy} + \frac{w}{h_z}\frac{dh_z}{dz}\right\} - \frac{\rho}{h_z}\left\{\frac{u^2}{h_x}\frac{dh_x}{dz} + \frac{v^2}{h_y}\frac{dh_y}{dz} + \frac{w^2}{h_z}\frac{dh_z}{dz}\right\}$$

$$+ 2\rho\omega\left(\frac{v}{h_x}\frac{dX_3}{dx} - \frac{u}{h_y}\frac{dX_3}{dy}\right) - \frac{\rho\omega^2}{h_z}\left(X_1\frac{dX_1}{dz} + X_2\frac{dX_2}{dz}\right) \qquad \text{(C12)}$$

$$\pi_z = \frac{\tau_{xz}}{h_x h_z}\frac{dh_z}{dx} + \frac{\tau_{yz}}{h_z h_y}\frac{dh_z}{dy} - \frac{\sigma_{xx}}{h_z h_x}\frac{dh_x}{dx} - \frac{\sigma_{yy}}{h_z h_y}\frac{dh_y}{dz} \qquad \text{(C13)}$$

$$\sigma_{P_z} = h_y h_z \, \tau_{zx} \, \underline{i} + h_z h_x \, \tau_{yz} \, \underline{j} \qquad \text{(C14)}$$

125

Internal energy equation

$$\frac{d}{dt}\int_A \rho E h_x h_y \, dA + \int_C \rho E(\underline{q} - \underline{q}_s) \cdot \underline{\hat{n}} \, dC - \int_C \rho E W' \underline{q}_s \cdot \underline{\hat{n}} \, dC = -\frac{1}{U_z}\int_A \rho E W' h_x h_y \, dA$$

$$+ \frac{1}{U_z}\left\{ \sigma_{zz} \frac{d}{dt}\int_A W h_x h_y \, dA + \tau_{yz} \frac{d}{dt}\int_A v \, h_x h_y \, dA + \tau_{zx} \frac{d}{dt}\int_A u \, h_x h_y \, dA \right\}$$

$$- \frac{1}{U_z}\left\{ \sigma_{zz}\int_C W \underline{q}_s \cdot \underline{\hat{n}} \, dC + \tau_{yz}\int_C V \underline{q}_s \cdot \underline{\hat{n}} \, dC + \tau_{zx}\int_C U \underline{q}_s \cdot \underline{\hat{n}} \, dC \right\} + \int_A h_x h_y h_z \Pi_E \, dA$$

$$+ \int_A \Pi_{EP} \, dA + \int_C \overline{\sigma}_P \, \underline{\hat{n}} \cdot \underline{q} \, dC + \int_C \tau_P \, \underline{\hat{n}} \cdot \underline{q}_\tau \, dC + \int_C \tau_{Pz} \, \underline{\hat{n}} \cdot \underline{q}_{\tau z} \, dC \quad \text{(C15)}$$

where:

$$\Pi_E = \sigma_{xx}\left[\frac{V}{h_x h_y}\frac{dh_x}{dy} + \frac{W}{h_x h_z}\frac{dh_x}{dz}\right] + \sigma_{yy}\left[\frac{W}{h_y h_z}\frac{dh_y}{dz} + \frac{U}{h_x h_y}\frac{dh_y}{dx}\right] + \sigma_{zz}\left[\frac{U}{h_x h_z}\frac{dh_z}{dx} + \frac{V}{h_y h_z}\frac{dh_z}{dy}\right]$$

$$- \tau_{xy}\left[\frac{V}{h_x h_y}\frac{dh_y}{dx} + \frac{U}{h_x h_y}\frac{dh_x}{dy}\right] - \tau_{zx}\left[\frac{U}{h_z h_x}\frac{dh_x}{dz} + \frac{W}{h_z h_x}\frac{dh_z}{dx}\right] - \tau_{yz}\left[\frac{W}{h_z h_y}\frac{dh_z}{dy} + \frac{V}{h_z h_y}\frac{dh_y}{dz}\right] \quad \text{(C16)}$$

$$\Pi_{EP} = -\left[\sigma_{zz}W + \tau_{yz}V + \tau_{zx}U\right]\frac{d(h_x h_z)}{dz} - \left[\sigma_{xx}U + \tau_{xy}V + \tau_{zx}W\right]\frac{d(h_y h_z)}{dx} - \left[\sigma_{yy}V + \tau_{xy}U + \tau_{zx}W\right]\frac{d(h_x h_z)}{dy} \quad \text{(C17)}$$

$$\overline{\sigma}_P = \begin{pmatrix} \sigma_{xx} & 0 \\ 0 & \sigma_{yy} \end{pmatrix} \quad \text{(C18)}$$

$$\tau_P = \begin{pmatrix} 0 & \tau_{xy} \\ \tau_{xy} & 0 \end{pmatrix} \quad \text{(C19)}$$

$$\tau_{Pz} = \begin{pmatrix} 0 & \tau_{zy} \\ \tau_{zx} & 0 \end{pmatrix} \quad \text{(C20)}$$

$$\underline{q}_\tau = u \, h_x h_z \, \underline{i} + v \, h_y h_z \, \underline{j} \qquad \underline{q}_{\tau z} = w \, h_x h_z \, \underline{i} + w \, h_y h_z \, \underline{j} \quad \text{(C21)}$$

REFERENCES

1. Hearsey, R.M., "Computer Program for Single-Stage Axial Compressor Test Data Analysis," ARL-73-0177, Vol. 1, December 1973.

2. Wennerstrom, A.J., "On the Treatment of Body Forces in the Radial Equilibrium Equation of Turbomachinery," ARL75-0052, April 1974.

3. Katsanis, T. and McNalley, W.D., "Revised Fortran Program for Calculating Velocities and Streamlines on the Hub-Shroud Mid-Channel Stream Surface of an Axial, Radial, or Mixed Flow Turbomachine or Annular Duct, II Programmers Manual, NASA TN D-8431, July 1977.

4. Dodge, P.R., "Transonic Two-Dimensional Flow Analysis of Compressor Cascade with Splitter Vanes," AFAPL-TR-75-110, December 1975.

5. Private communication.

6. Pulliam, T.H. and Steger, J.L., "On Implicit Finite Difference Simulations of Three-Dimensional Flow," AIAA 16th Aerospace Sciences Meeting, Huntsville, Alabama, Jan. 16-18, 1978, AIAA Paper No. 78-10.

7. King, L.S., Walitt, L. and Enos, J.A., "An Investigation of Computational Time Reduction Methods for Solving the Navier-Stokes Equations," NASA TM X-73,102, October 1975.

8. Walitt, L., Harp, J.L. and Liu, C.Y., "Numerical Calculation of the Internal Flow Field in a Centrifugal Compressor Impeller," NASA CR-134984, December 1975.

9. Walitt, L. and Rutz, R., "Feasibility Extension Study of a Computer Program for the Numerical Calculation of the Internal Flow Field in a Centrifugal Compressor Impeller," Progress Rept. #11 on Contract NAS3-20032, August 1977.

10. Baldwin, B.S., and Rose, W.C., "Calculation of Shock-Separated Turbulent Boundary Layers," Proceedings NASA Conference on Aerodynamic Analyses Requiring Advanced Computers, Langley, Virginia, March 1975.

11. Deiwert, G.S., "Computation of Separated Transonic Turbulent Flows," Private Communication. See also Deiwert, G.S., McDevitt, J.B., and Levy, L.L. Jr., "Simulation of Turbulent Transonic Separated Flow," Proceedings NASA Conference on Aerodynamic Analyses Requiring Advanced Computers, Langley, Va. March 1975

12. Baldwin, B.S., and MacCormack, R.W., "Numerical Solution of the Interaction of a Strong Shock Wave with a Hypersonic Turbulent Boundary Layer," AIAA Paper 74-558, AIAA 7th Fluid and Plasma Dynamics Conference, June 1974.

13. Cebeci, T., "Calculation of Compressible Turbulent Boundary Layers with Heat and Mass Transfer," *AIAA Journal*, Vol. 9, No. 6, p. 1091, 1971.

14. Cebeci, T., Smith, A.M.O. and Mosinskis, G., "Calculations of Compressible Adiabatic Turbulent Boundary Layers," *AIAA Journal*, Vol. 8, No. 11, p. 1974, 1970.

15. Kolmogorov, A.N., "Equations of Turbulent Motion of an Incompressible Liquid," *Izv. Akad. Nauk SSR Seria fizichiska* VI, No. 1-2, p. 56, 1942.

16. Saffman, P.G., "A Model for Inhomogeneous Turbulent Flow," Proc. Roy. Soc., A317, p. 417, 1970.

17. Chou, P.Y., "On the Velocity Correlations and the Solution of the Equations of Turbulent Fluctuation," *Q. Appl. Math.*, Vol. 3, p. 38, 1945.

18. Hawlow, F.H. and Nakayama, P.I., "Transport of Turbulence Energy Decay Rate," Los Alamos Sci. Lab., University of California, Rep. LA-3854, 1968.

19. Jones, W.P. and Lauder, B.E., "The Prediction of Laminarisation with 2-Equation Model of Turbulence," *Int. J. Heat Mass Transfer*, Vol. 15, p. 301, 1972.

20. Ng, K.H. and Spalding, D.B., "Some Applications of a Model of Turbulence to Boundary Layers near Walls," *Phys. of Fluids*, Vol. 15, 1972.

21. Wilcox, D.C., "Calculation of Turbulent Boundary-Layer Shock-Wave Interaction," *AIAA Journal* Vol. II, No. 11, p. 1592, 1973.

22. Prandtl, L., "Bericht uber Untersuchungen zur ausgebildeten Turbulenz," *ZAMM*, Vol. 5, p. 135, 1925.

23. Van Driest, E.R., "On Turbulent Flow Near a Wall," *J. Aerospace Sci.*, Vol. 23, No. 11, p. 1007, 1956.

24. Shang, J.S. and Hankey, W.L., Jr., "Numerical Solution of the Navier-Stokes Equations for Supersonic Turbulent Flow over a Compression Corner," AIAA Paper 75-4, 1975.

25. Granville, P.S., "The Calculation of the Viscous Drag of Bodies of Revolution," Rep. 849, David Taylor Basin, 1953.

26. Michel, R., "Etude de la Transition sur les Profiles d'aile, Establissement d'un Critere de Determination due Point de Transition et Calcul de la Trainee de Profile Incompressible," O.N.E.R.A. Report 1/1578A, July 1951.

27. Lauder, B.E. and Spalding, D.B., "Mathematical Models of Turbulence," Academic Press, p. 82, 1972.

28. Ibid, p. 144.

29. Holtman, R.L., McClure, R.B., and Sinnett, G.T., "Test of a Supersonic Compressor Cascade with Splitter Vanes," Aerospace Research Laboratories Report ARL 73-0142, pp. 257-265, December 1973.

30. Vavra, M.H., Aero-Thermodynamics and Flow in Turbomachines, pp. 499-508, Wiley, 1960.

31. Liepmann, H.W. and A. Roshko, "Elements of Gas Dynamics," 1st Edition, p. 126, Wiley, N.Y., 1957.

32. Liepmann, H.W. and A. Roshko, Elements of Gas Dynamics, 1st Edition, p. 346, Wiley, N.Y., 1957.

33. MacCormack, R.W. and Paullay, A.J., "Computational Efficiency Achieved by Time Splitting of Finite Difference Operations," AIAA Paper No. 72-154, 1972.

34. Mach, K.D., "An Alternating-Direction-Implicit Solution of Subsonic Cascade Flow," AFAPL-TR-75-80, March 1976.